Studies for current and future high intensity experiments at the CERN P42 and K12 beam lines

Gian Luigi D'Alessandro

Department of Physics

Royal Holloway, University of London

A thesis submitted to the University of London for the degree of Doctor of Philosophy

15th December 2021

Declaration

I confirm that the work presented in this thesis is my own. Where information has been derived from other sources, I confirm that this has been indicated in the document.

Signed:

Date: 15/12/2021

I dedicate this thesis to my family and my girlfriend.

Abstract

Fixed target experiments in particle physics provide the possibility of reaching a large number of particle collisions, allowing precise measurements of physics observables. CERN hosts a variety of fixed target experiments that aim at high-precision measurements, few of them located in the so-called North Area. These experiments make use of the 400 GeV/c proton beam extracted from the SPS that is led to collide on a target head to produce diverse particle species. Among these experiments there is NA62 that aims at measuring ultra rare decays (mainly $K^+ \to \pi^+ \nu \bar{\nu}$) to a high precision (10% for $K^+ \to \pi^+ \nu \bar{\nu}$) in order to challenge the Standard Model and conduct searches for new particles. In the case of NA62, the primary protons coming from the SPS are transported via a series of transfer lines to the P42 beam line, which guides the beam to the T10 beryllium target that generates a secondary beam. A 75 GeV/c positive particle component of the beam is selected by the K12 beam line; it contains about 6% of positive kaons that are afterwards transported to the NA62 experiment. Such a high precision experiment requires detailed Monte Carlo simulation models for understanding the beam and characterisation of the background. These models have been created and are studied within this thesis. The software tools used for the development are BDSIM, FLUKA and MADX. It is shown in particular that the beam in K12 can be simulated to a very high detail in BDSIM and FLUKA reaching an overall agreement with data within 1%. The BDSIM model is used to study background for muons generated along the beam line, showing satisfactory agreement with data for a large part of the spectrum. Finally, the FLUKA model is used to show that the background produced by particle interactions with the residual gas present in the vacuum tank is negligible. Besides NA62, more high-intensity experiments are currently being considered to take place in the P42 and K12 beam lines in future.

These are KLEVER, NA62-HIGH-INTENSITY, NA62-BEAM-DUMP and SHADOWS. The nature of these experiments is quite diverse and they all cover different physics topics, including Standard Model investigation and dark matter searches. Feasibility and characterisation studies for the beam lines of these experiments are carried out and presented in this thesis. In particular, it's shown in this thesis how the KLEVER beam line can be optimised regarding the radiation levels, calculated in FLUKA, outside the experimental hall. Studies on the P42 beam line in MADX and AppLE.py show that the current intensity for K12 can be increased using a target bypass technique useful for KLEVER and NA62-HIGH-INTENSITY. Finally, an NA62-BEAM-DUMP model is created in BDSIM and benchmarked to data for muon background characterisation. The same model is used for studies on the background reduction for SHADOWS that show first proof of feasibility of the experiment with the existing beam line design.

Acknowledgements

My PhD work has been developed as a collaboration between Royal Holloway and CERN. I was given the opportunity to work in these two fantastic environments where I met great people that helped me to develop this thesis. First of all I have to thank my supervisor, Stephen Gibson that gave me the chance to undertake my PhD and thoroughly supported me in this experience. He has always been very kind and gave me plenty of good ideas and inspiration for the development of the thesis work. My research would have been impossible without the aid and support of my CERN supervisor, Alexander Gerbershagen. He has always been there for me and has always combined a great leadership with a gentle behaviour. I could learn a lot from him both on human and scientific aspects, I really enjoyed working side by side with him at CERN. I wish to thank Stewart Boogert for his great help during my stay at Royal Holloway, his software and coding knowledge really impressed me, I am glad that I could learn a lot from him. My sincere thanks go to my CERN group leader, Markus Brugger, he welcomed me in the group making me feel part of the CERN community and he gave me important feedback for most of the work developed in this thesis. Johannes Bernhard gave me invaluable help with all my studies, he guided me and introduced me the most important physics concepts treated in this thesis, he is a brilliant physicist without whom I could not have reached the current work status. Many of the ideas presented in this thesis have come from Lau Gatignon. Lau is one of the main scientists working for the North Area at CERN and he represented for me a living bible during the period at CERN, there was not a single time where I did not get an answer from a technical or physics related question, his support was truly fundamental for the development of my work. I wish to acknowledge Laurie Nevay for all his support with BDSIM, it is impossible to express in words how much Laurie knows

Contents

List of Figures

17

List of Tables

Chapter 1

Introduction

High-energy physics is the branch of physics that studies the smallest components of matter. The developments of this branch led to the discoveries of elementary particles that are understood to be the building blocks of the universe. These particles are described in the so called Standard Model (SM) that calculates and predicts most of their properties. The European Organization for Nuclear Research (CERN) has played a main role in this field and here were discovered several particles and properties of the SM. CERN hosts the Large Hadron Collider (LHC) that is currently the biggest accelerator on Earth and has a vibrant and wide research spectrum.

This thesis was fully developed at CERN within the EA-LE section (Experimental Areas and Liason with Experiments) that collaborates with Royal Holloway, University of London and the John Adams Institute. The work laid out here is experimental and mainly focused on simulation models production, their analysis and comparison to data.

The EA-LE section is in charge of several CERN experimental areas and facilities to which it also provides technical support. It is in particular responsible for the design, maintenance and operation of the secondary beams (beams that are downstream of the primary targets), as well as of irradiation or test facilities in the CERN accelerator complex. Among the experiments located in the experimental areas there is the NA62 experiment [1] that is an experiment focused on rare kaon decays. The physics of kaons is particularly interesting for searches within the SM and beyond. One of the milestones reached in kaon physics is the proof of CP violation in 1964.

NA62 is located in one of the experimental areas at CERN (North Area) on the K12 beam line managed by EA-LE and it is currently one of the highest-intensity kaon beams in the world. The goal of the experiment is to do testing of the Standard Model via measurements of the rare kaon decay $K^+ \to \pi^+ \nu \nu$. The experiment managed to measure for the first time in 2018 this very rare decay that has a theoretical branching ratio of 1.7×10^{-10} [2].

Several upgrades of the NA62 experiment are being considered within the Physics Beyond Colliders study (PBC) [3]. The PBC program aims at investigating the most important open questions in particle physics, exploiting the full infrastructure of CERN through projects that are complementary to high-energy colliders. A study group was founded within the PBC, the Conventional Beams Working Group (CBWG), in order to study potential new experiments at the CERN experimental areas. This study group is in part dedicated to studies on the future of the K12 beam line, where NA62 is currently located. These studies are diverse and include experiments in search for dark matter, such as NA62 Beam Dump (NA62-BD) and Search for Hidden And Dark Objects With the SPS (SHADOWS), studies on neutral kaons like KLEVER [4] and a possible adaptation of NA62 and its beam line to allow it to run at substantially higher intensities (called NA62-High-Intensity, NA62-HI, or NA62×4) [5].

The simulations developed in this thesis aim to study the various kind of backgrounds that are expected on the K12 beam line for: NA62, NA62-BD, SHADOWS, KLEVER and NA62-HI. The feasibility of some of the new experiments within PBC will also be investigated. The work includes the quantification of radiation outside the experimental hall and shielding requirements. These studies are carried out keeping an active interface with the relevant experimental groups.

An overview of the relevant particle physics is discussed in the next chapter with a focus on kaon physics. In Chapter 3 an overview of the applicable accelerator physics concepts is given. In Chapter 4 the various experiments that are studied for this thesis are described in detail. Chapter 5 gives an overview of the simulation tools used for the various applications. Chapter 6 is dedicated to studies for collimators in experimental areas that

are useful also for secondary beams. In Chapters 7 and 8 the technical work done for the experiments and the simulations is explained in detail. Finally, Chapter 9 gives an outlook and summarises all the results of the thesis.

Chapter 2

Particle and Kaon Physics

This chapter introduces some general concepts of particle physics and focuses on the physics of kaons. At the end of the chapter there is a short overview of the topic of dark matter, which is a relevant subject for a part of the studies presented in this thesis.

2.1 Standard Model Overview

The Standard Model (SM) of particle physics is a theory that describes the known elementary particles and their interactions. The SM is a quantum field theory (QFT) that combines quantum physics with relativity. All the particles in the SM are considered as excited quantum states which are characterised by their quantum numbers. Every particle interacts via up to three main forces: electromagnetic, weak and strong interaction. The Higgs mechanism, that explains the origin of elementary particle's mass via spontaneous symmetry breaking, is also described in the SM [6]. Particles of the Standard Model are divided into two main classes according to their spin (intrinsic angular momentum): bosons (with integer spin) and fermions (with half-integer spin). Fermions obey the Pauli Exclusion Principle that states that two identical fermions in the same system cannot occupy the same quantum state. There are currently twelve known fermions (six quarks and six leptons) and thirteen bosons (γ, two W-bosons, Z, eight gluons and the Higgs) in the SM, a schematic of these particles is shown in Figure 2.1. The Dirac equation shows that a charged massive fermion has an antiparticle of the same mass and spin, but opposite charge, and opposite magnetic moment relative to the direction of the spin. Leptons and quarks have spin $\frac{1}{2}$, in units of $\hbar$ (that is the Planck constant divided by 2π). Charged leptons can interact only through the electromagnetic and the weak interactions. Various
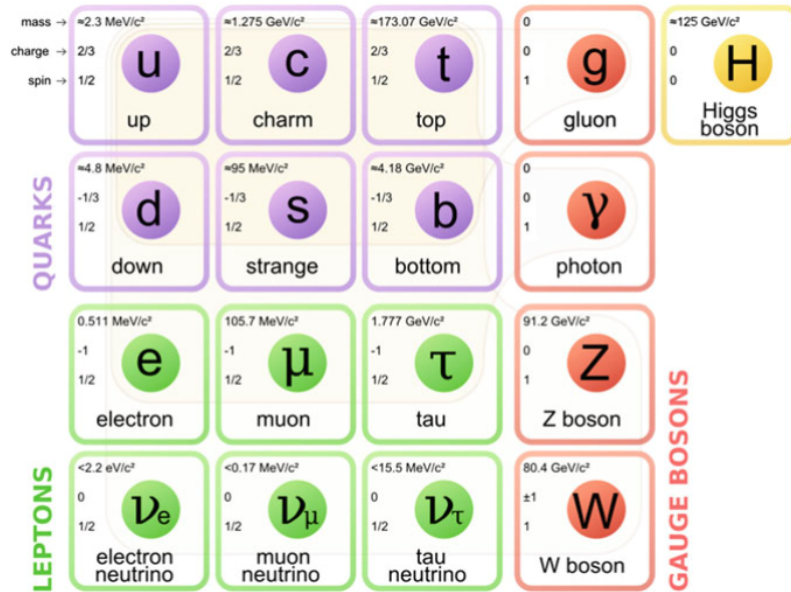
Figure 2.1: Currently known SM particles. The fermions are listed on the first three columns, with the bosons on the right [7].

experiments in the field of particle physics led to the conclusion that a charged lepton of certain type or flavour (e,μ,τ) can change via an interaction only to another of the same type and a lepton and an anti-lepton of the same type can only be created or destroyed together [7]. This effect is known as lepton number conservation. Quarks interact through the electromagnetic, weak and also through the strong interaction. Quarks have a colour charge in the strong interaction that can be seen as the analogue of the electric charge for electromagnetism. The number of different types (flavours) of quark are not separately conserved, indeed flavour changes are possible through the weak interaction. The most elementary bound systems of quarks are baryons which are composed of three quarks (or anti-quarks) and mesons which are composed of a quark and an anti-quark. The protons and neutrons are baryons.

Bosons are the mediators of the forces described by the SM. The electromagnetic interaction is mediated via the photon, the weak interaction is mediated via the W and the Z bosons and the strong interaction is mediated via the gluons. SM interactions are usually described via the Standard Model Lagrangian that has internal symmetry $SU(3) \times SU(2) \times U(1)$. The processes in the SM are usually represented via Feynman diagrams that help in their visualisation and are very useful tools in the calculation of measurable quantities such as cross-sections, which quantify the probability of interaction, and decay rates, which quantify the probability of decay. See an example of a Feynman dia-

gram in Figure 2.2 [8].
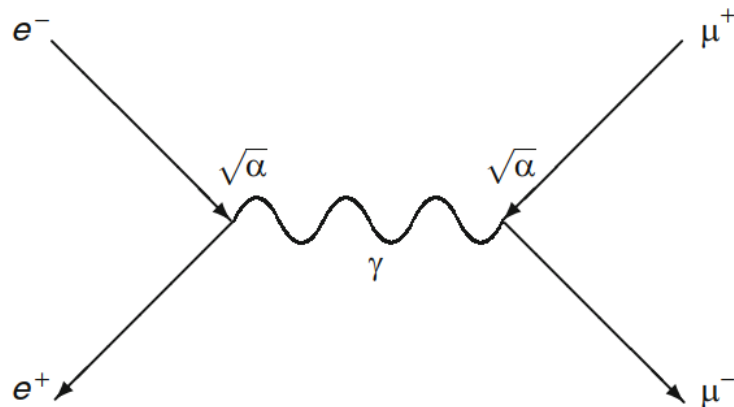
Figure 2.2: Annihilation process of an electron and its antiparticle, the positron, into a gamma that generates two muons [8].

The predictions of the SM have been largely verified in experiments worldwide, nevertheless this model in not complete. For example, it does not include the gravitational force and has 19 free parameters that cannot be predicted theoretically. It does not explain baryon asymmetry nor does it account for the accelerating expansion of the Universe, an effect that could be described with the introduction of dark energy. The model does not contain dark matter particles that satisfy the required properties deduced from observational cosmology. Finally it does not incorporate neutrino oscillations and their non-zero masses.

2.2 Physics Symmetries

In this section some relevant quantum operators are introduced. These operators will help to describe the quantum states of kaons (discussed in more detail later in this chapter). Conservation laws in a quantum process regulate the possibility of a state transforming into another state (collision or decay); these are expressed in terms of the quantum numbers of those states. State transformations can be represented via the application of a quantum operator, Q, that leads from an initial state $|i\rangle$ to a final state $|f\rangle$, $|f\rangle = Q|i\rangle$. In this section three operators are discussed: P, C and T. The parity operation P when applied to a certain state, inverts the three spatial coordinates. A state has a well-defined parity

only if it has a defined eigenvalue under the application of the operator P. This means:

$$P|\psi\rangle = p|\psi\rangle, \quad \text{with} \quad p = \pm 1 \tag{2.1}$$

The state of vacuum falls into this category and its parity is set positive by definition. The eigenvalue p of P is called intrinsic parity (or parity), which can be either positive ($p = 1$) or negative ($p = -1$). The parity of the proton is assumed positive by convention and the parities of the other fermions are given relative to this. The charge conjugation operator (C) acting on one particle state changes this particle into its antiparticle, leaving the other properties unchanged. This means that the sign of all the additive quantum numbers such as electric charge, baryon number and lepton flavour are changed under a C transformation [9]. The time reversal operator, T, inverts the time leaving the spatial coordinates unchanged. Studies of symmetries and experimental results show that all phenomena in quantum field theory are invariant under CPT transformation [10].

2.3 Weak Interaction and CKM matrix

In the present section the CKM matrix is introduced, which is an important component for this thesis and is highly relevant for kaon decays.

In 1963 Cabibbo introduced a mathematical formalism to explain the transformation between strong states and weak states [11]. The two bases (for each representation) are connected by a unitary transformation (matrix) introduced by Cabibbo that for the (d, s) doublet can be represented as:

$$\begin{pmatrix} d' \\ s' \end{pmatrix} = \begin{pmatrix} V_{ud} & V_{us} \\ V_{cd} & V_{cs} \end{pmatrix} \begin{pmatrix} d \\ s \end{pmatrix} \tag{2.2}$$

The generalisation to three quark families was done by M. Kobayashi and K. Maskawa in 1973 [12].

$$\begin{pmatrix} d' \\ s' \\ b' \end{pmatrix} = \begin{pmatrix} V_{ud} & V_{us} & V_{ub} \\ V_{cd} & V_{cs} & V_{cb} \\ V_{td} & V_{ts} & V_{tb} \end{pmatrix} \begin{pmatrix} d \\ s \\ b \end{pmatrix} \tag{2.3}$$

For these reasons, this matrix is nowadays called the Cabibbo–Kobayashi–Maskawa (CKM) matrix and the unitarity condition means that has to satisfy:

$$V_{\mathrm{ckm}}V_{\mathrm{ckm}}^{\dagger} = 1 \tag{2.4}$$

The CKM matrix determines the probability of transition from a quark state i into another state j. These transitions are proportional to the matrix elements $|V_{ij}|^2$. This matrix is a complex unitary matrix, and has therefore nine real degrees of freedom. It is possible to show that these nine parameters are interdependent and can be reduced to four: three angles and one phase. These angles can be named θ_{12}, θ_{23} and θ_{13} representing the rotations in the flavour space, and the phase δ. Using this formalism the CKM matrix can be rewritten as:

$$V_{\mathrm{ckm}} = \begin{pmatrix} c_{12}c_{13} & s_{12}c_{13} & s_{13}e^{-i\delta} \\ -s_{12}c_{23} - c_{12}s_{23}s_{13}e^{i\delta} & c_{12}c_{23} - s_{12}s_{23}s_{13}e^{i\delta} & s_{23}c_{13} \\ s_{12}s_{23} - c_{12}c_{23}s_{13}e^{i\delta} & -c_{12}s_{23} - s_{12}c_{23}s_{13}e^{i\delta} & c_{23}c_{13} \end{pmatrix} \tag{2.5}$$

Where $c_{ij} = \cos\theta_{ij}$ and $s_{ij} = \sin\theta_{ij}$. This parametrisation is usually called "standard parametrisation". Its coefficients have been experimentally measured to be: $\theta_{12} = (13.02 \pm 0.04)°$, $\theta_{23} = (2.36 \pm 0.08)°$, $\theta_{13} = (0.20 \pm 0.02)°$ and $\delta = (69 \pm 5)°$ [13]. All the rotation angles are comparably small, hence, the CKM matrix is approximately diagonal. Assuming that θ_{23} and θ_{13} are equal to zero, the largest angle, θ_{12}, is responsible for the flavour mixing. If $\sin(\theta_{12})$ is fixed to be equal to a parameter λ the CKM matrix can be rewritten as:

$$|V_{\mathrm{ckm}}| \approx \begin{pmatrix} 1 - \frac{\lambda^2}{2} & \lambda & \lambda^3 \\ -\lambda & 1 - \frac{\lambda^2}{2} & \lambda^2 \\ \lambda^3 & \lambda^2 & 1 \end{pmatrix} \tag{2.6}$$

This is known as the Wolfenstein parametrisation. In the SM, the CKM matrix is unitary by construction. If a fourth generation (another quark type) was discovered, the CKM matrix would not need to be unitary within the three generations. This means that testing the CKM matrix for unitarity assuming three generations is a way to indirectly look for physics beyond the Standard Model. In practice, what is done by the experiments is to measure all the CKM elements separately (independently) to check if unitarity holds. The

current best measured values are [13]:

$$
\begin{pmatrix} V_{ud} & V_{us} & V_{ub} \\ V_{cd} & V_{cs} & V_{cb} \\ V_{td} & V_{ts} & V_{tb} \end{pmatrix} = \begin{pmatrix} 0.97 \pm 0.0001 & 0.22 \pm 0.001 & 0.039 \pm 0.0004 \\ 0.23 \pm 0.01 & 1.02 \pm 0.04 & 0.0041 \pm 0.001 \\ 0.0084 \pm 0.0006 & 0.039 \pm 0.002 & 0.88 \pm 0.07 \end{pmatrix} \quad (2.7)
$$

These values can be determined in different ways, for example by measuring the semi-leptonic decay rates of hadrons (such as kaons) of different flavours such as: beauty, charm and strangeness. A convenient and commonly used representation of the CKM elements is attained via the so-called unitarity triangle. Unitarity implies that the rows of the CKM matrix are orthonormal, as well as the columns. That can be expressed as: $\sum_i V_{ij} V_{ik}^* = \delta_{jk}$ for any i and k [6]. The constraints given by the unitarity conditions can be represented as a closed triangle in the complex plane, as shown in Figure 2.3: The
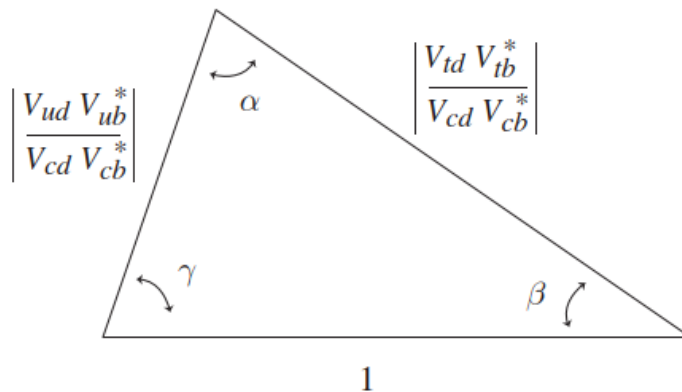
Figure 2.3: Representation of the CKM-matrix unitarity via a triangle. One side of the triangle is normalised to unity and the others are related to the CKM matrix elements V_{ij}. The angles of the triangle are independent and can be a sensitive probe to CP violation processes [6].

lengths of the sides of the unitarity triangle are indicators of flavor mixing and the angles of the triangle are sensitive to CP violation.

2.4 Kaons

This section introduces the particles named kaons. Historically, these particles were essential in establishing the foundations of the Standard Model of particle physics. This section begins with the description of the discovery of those particles moving on to what are their main properties and their importance for the SM.

2.4.1 Kaons Discovery

In order to better understand the evolution of kaon physics the first observation of kaons is introduced here. Cosmic rays that collide with the terrestrial atmosphere produce showers of secondary particles. Leprince-Ringuet and L'Heritier, using a cloud chamber, measured new components in the showers of cosmic rays in 1943 [14]. These new components (particles) had a "strange" behaviour. They were produced in pairs and by "fast" strong interactions, proven by the large cross section of the process, but they decayed with lifetimes typical of weak interactions. For this reason they were called "strange particles". The physical interpretation of these particles was given independently by Nishijima [15] and by Gell-Mann [16]. They introduced a new quantum number S, the "strangeness", which is an additive quantum number. Figure 2.4 shows a kaon decay observed in a cloud chamber. S is conserved in strong and electromagnetic interactions while it is not in weak
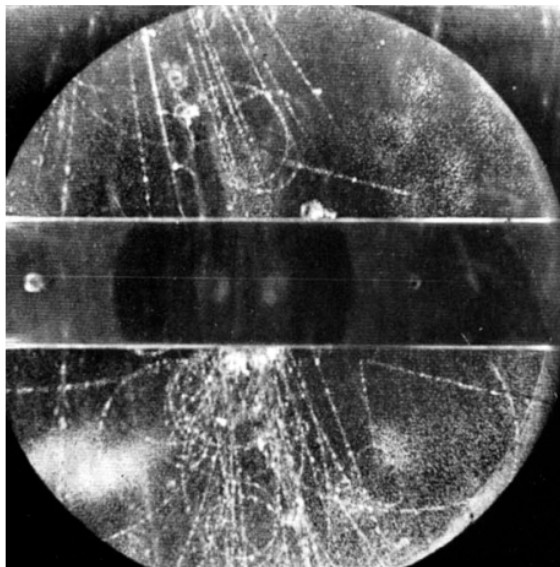
Figure 2.4: Kaon decay in a cloud chamber [17].

ones. The production via strong interactions starting from an initial state with $S = 0$ it is allowed only if two particles with opposite S are generated (in this case the two K^0s). Due to conservation of energy, kaons can decay only to lighter non-strange states, hence, they are not allowed to decay strongly. It was later discovered that there are four kaons, two neutrals, described in next section, and two charged. The two charged K mesons are the K^+ and its antiparticle, the K^-.

2.4.2 Kaon States

The $K^0 = d\overline{s}$ and $\overline{K^0} = \overline{d}s$ are generated in pairs via the strong interaction and are the antiparticle of one other. These have respectively strangeness $S = 1$ and $S = -1$. The fact that they are antiparticles means: $CP|K^0\rangle = \overline{K^0}$ and $CP|\overline{K^0}\rangle = K^0$. The K^0 and $\overline{K^0}$ can exchange into each other via virtual common decay modes: $K^0 \to 2\pi \to \overline{K^0}$ and $K^0 \to 3\pi \to \overline{K^0}$. These Ks are not CP eigenstates but can be CP eigenstates if represented in the following basis:

$$|K_1\rangle = \frac{1}{\sqrt{2}}(|K^0\rangle + |\overline{K^0}\rangle), \qquad CP = +1 \tag{2.8}$$

$$|K_2\rangle = \frac{1}{\sqrt{2}}(|K^0\rangle - |\overline{K^0}\rangle), \qquad CP = -1 \tag{2.9}$$

In order to characterise the eigenstates of these kaons, the 2π and 3π neutral systems can be considered. The CP eigenvalue of a neutral 2π system is positive. Actually it can be shown that:

$$CP(\pi^0\pi^0) = [CP(\pi^0)]^2 = (-1)^2 = +1$$
$$CP(\pi^+\pi^-) = C(\pi^+\pi^-)P(\pi^+\pi^-) = (-1)^l(-1)^l = +1$$

Where l is the angular momentum of the state. As a consequence, if CP is conserved, only the K_1, with the eigenvalue $CP = +1$, can decay into 2π. For the 3π systems the following relation is valid:

$$CP(\pi^0\pi^0\pi^0) = [CP(\pi^0)]^3 = (-1)^3 = -1 \tag{2.10}$$

The state $\pi^-\pi^+\pi^0$ is a bit more complicated but after some calculations it can be proved that [9]:

$$CP(\pi^+\pi^-\pi^0) = -1 \tag{2.11}$$

These calculations show that if CP is conserved, only the CP state with eigenvalue $CP = -1$, that is K_2, can decay into $3\,\pi$. This means that if CP is conserved the allowed decays are:

$$K_1 \to 2\pi, \quad K_2 \to 3\pi. \tag{2.12}$$

If CP was conserved, K_1 and K_2 would be states with definite mass and lifetime. It will be shown in the next sections that CP is lightly violated, and that the states that have definite mass and lifetime are the so-called "Kaon short" (K_S) and "Kaon long"(K_L) respectively. It is experimentally shown that the lifetime of the (Kaon short) state decaying into 2π, is approximately 580 times shorter than the lifetime of the (Kaon long) state decaying into 3π [9].

2.4.3 Kaon Oscillation

In 1955 Gell-Mann and Pais [18] speculated that oscillations of strangeness should happen for a pure K^0 beam. This means that starting with a K^0 beam, it should be possible to observe a $\overline{K^0}$ component in the beam after a certain time τ. In order to prove this
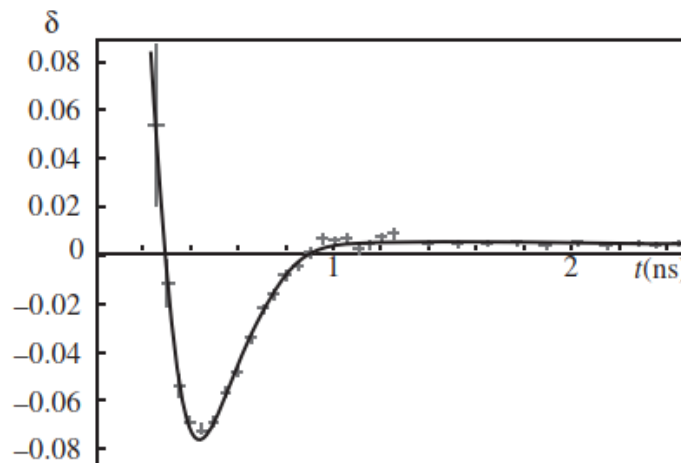
Figure 2.5: Probability function δ of oscillation in a kaon neutral system. This probability is quantified via the charge asymmetry, namely the difference between the numbers of observed K^0 semi-leptonic decays and the number of $\overline{K}^0$ semi-leptonic decays [9].

assumption measurements for a beam of K^0s had to be executed. In particular, to select definite strangeness states, semi-leptonic decays have to be selected. In these processes the difference between the strangeness of the kaons in the final and initial states is equal to the difference of electric charge and are easy to observe since the decays have a large branching ratio. Therefore, experimentally, the oscillation of kaons is measured via the charge asymmetry, that is the difference between the numbers of observed $K^0 \to \pi^- l^+ \nu_l$ and $\overline{K^0} \to \pi^+ l^- \overline{\nu_l}$ events. The difference between the probability of having a K^0 and a

$\overline{K^0}$ can be calculated as a function called δ. This measurement was carried out at the CERN PS accelerator [19]. The calculated δ function and the relative data can be seen in Figure 2.5. It was therefore proven that there is an oscillation within the beam as predicted by theory. It can also be noticed that the function does not converge to 0 as it should do if K^0s were CP eigenstates.

2.4.4 Kaon Regeneration

A final confirmation of the phenomenom of oscillation was given by the Pais-Piccioni experiment [20]. This experiment used a beam of π^- colliding on target to generate neutral kaons K^0. The K^0 state is represented as a superposition of K_1 and K_2. The K_1 component decays mainly into 2π and does so at short distances, the K_2 survives for longer times and does not decay into 2π, provided CP is conserved. The 2π decays are observed immediately after the target (the short-lived component disappears), leaving a beam of pure long-lived kaons with half the initial intensity. If a second target is inserted, the surviving neutral K mesons interact with the nuclei in this target by strong interactions. If this beam interacts with the target material, then the K^0 and its antiparticle $\overline{K^0}$ interact differently with the nuclei. The K^0 undergoes quasi-elastic scattering with nucleons, whereas its antiparticle can create hyperons. Given the different interactions of the two components, K^0 and $\overline{K^0}$, the coherence between the particle states vanishes. The emerging beam then contains different linear superpositions of the K^0 and $\overline{K^0}$. This kind of state (superposition) is a mixture of K_1 and K_2. This proves that the K_1 component is "regenerated" by a neutral kaon beam passing through matter. This process, called "regeneration", was observed for the first time at Lawrence Berkeley National Laboratory [20].

2.4.5 CP Violation in Kaon Systems

In 1964 James Cronin, Val Fitch [21] and coworkers while working at the Brookhaven National Laboratory proved that CP-symmetry could be broken. This discovery proved that weak interactions violate the charge-conjugation symmetry C that links a particle to its antiparticle and the parity P, but also their combination CP. The approach of the experiment was to create a beam of K_1 and K_2 decaying over a length of approximately 17 meters. For the properties discussed before: one of these components it is long lived (K_2), while the other is the short lived (K_1). Short lived kaons decay quickly into two pions while the long lived ones into three. Given these conditions at the end of the beam

line, one would expect to see only decays from the K_2 and therefore to detect three pions decays only. The experiment found out that this is not always true, and proved that the K_2 particle decays into two pions (45 events detected out of the total 22700) as well, violating the particle-antiparticle symmetry. This kind of CP violation was linked to the fact that neutral kaons can oscillate into their antiparticles and vice-versa, but this transformation does not occur with exactly the same probability in both directions, this is called indirect CP violation. Summarising, the experiment shows that the two CP eigenstates K_1 and K_2 are not the states with definite mass and lifetime. The latter can be written as:

$$|K_S\rangle = \frac{1}{\sqrt{1 + |\epsilon|^2}}(|K_1\rangle + \epsilon|K_2\rangle) \tag{2.13}$$

$$|K_L\rangle = \frac{1}{\sqrt{1 + |\epsilon|^2}}(\epsilon|K_1\rangle + |K_2\rangle) \tag{2.14}$$

The ϵ parameter measures the small impurity of the imprecise CP conservation. The Fitch and Cronin experiment was sensitive to the absolute value of this complex parameter. Other searches on CP violation were conducted without any success before the 1990s, when the NA31 experiment at CERN suggested a first evidence for CP violation in the decay process of the neutral kaons (direct CP violation) confirmed afterwards by the NA48 experiment [22] and KTeV at Fermilab [23]. CP violation is considered one of the milestones of particle physics and represented at the time of its discovery a revolution for the field. Nowadays the research program on kaons is still active and continues with a main focus on rare kaon decays.

2.4.6 Rare Kaon Decays

Kaons have a relatively long lifetime because they decay only weakly. For this reason, studies of their decays provide a useful probe of the weak interaction behaviour under the three fundamental symmetry operators C, P, and T. One of the decay channels currently studied is the $K \to \pi\nu\overline{\nu}$. The decay rate of this process caused by $s \to d\nu\overline{\nu}$ quark flavor-changing neutral currents (FCNC) can be calculated within the Standard Model to a high precision. For this reason, this channel is also referred to as "golden". It is reminded here that flavour changing neutral currents are processes in which there is not charge exchange but a flavour state change. In the Standard Model FCNC decays are forbidden at the tree level because of the unitarity of the quark-mixing matrix. These processes can anyway

happen via loop diagrams involving virtual quarks and intermediate bosons. Figure 2.6 shows the so called penguin and box loop diagrams that describe these processes within the SM. In the SM, the decays $K \to \pi\nu\bar{\nu}$ are "clean" processes that can be calculated to a high precision. For the probability of the decay $K^+ \to \pi^+\nu\bar{\nu}$, the uncertainties in the
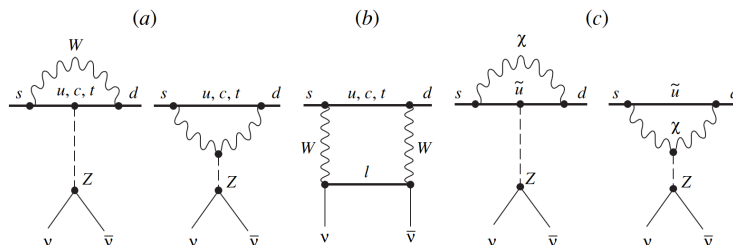
Figure 2.6: One-loop diagrams of leading order contributions for the $K \to \pi\nu\nu$ decay in the SM [24].

theoretical calculations do not exceed 5 to 7%. For the decay $K_L \to \pi^0\nu\bar{\nu}$ the uncertainties are not above 2%.

From the previous arguments it is deduced that decays like $K \to \pi\nu\bar{\nu}$ are strongly suppressed and are therefore characterised by very small expected branching ratios (below 10^{-10}). Such an effect offers interesting prospects for seeking new effects beyond the Standard Model. The $Zd\bar{s}$ vertices in the diagrams in Figure 2.6 are determined by the short-distance region around $r \sim 1/M_Z$. Therefore, the decays $K \to \pi\nu\bar{\nu}$ are sensitive probes to the contribution of new heavy objects, which also happen at short distances. It can be concluded that a comparison of experimental results with theoretical estimates within the Standard Model would make it possible to search for direct manifestations of new physics in these rare kaon decays [25].

2.5 Dark Matter

The term dark matter is used to describe a form of matter that has not yet been fully understood and that cannot be observed since it does not seem to interact electromagnetically. In 1933, Fritz Zwicky who studied galaxy clusters, confirmed previous observations of an apparent missing portion of the mass of these clusters, called by Zwicky, "dunkle Materie" ("dark matter") [26]. Because dark matter has not yet been observed directly, if it exists, it must rarely interact with ordinary matter, except through gravity. Most of the hypothesised dark matter is not composed by baryons and it may be composed of some

undiscovered elementary particles [27]. The primary candidate for dark matter is some new kind of elementary particle that has not yet been discovered, such as WIMPs [28], heavy neutral leptons (HNL) [13] and dark photons [29]. In the rest of the section these dark matter candidates are described since they are relevant for some of the studies within PBC.

2.5.1 Dark Photon

The dark photon is a hypothetical spin-1 boson and could be the carrier particle of a new force. It would have properties similar to the photon and would also be described by an abelian U(1) symmetry, but the strength of this force (ϵ') would be very weak, making it very difficult to be observed. The discovery of the dark photon could explain the anomalous magnetic dipole moment of electromagnetism, where experiments show, that the expected value for electrons, muons and tau lepton is about 0.1% off the value calculated. This difference could be explained if a mixing between the photon and the dark photon is assumed. Besides the effect on electromagnetism via mixing and possible interactions with dark matter particles, a dark photon (if massive) can also play the role of a dark matter candidate itself [29]. Figure shows 2.7 the regions covered by various experiments for dark photon searches as a function of mass and coupling strength ϵ'.
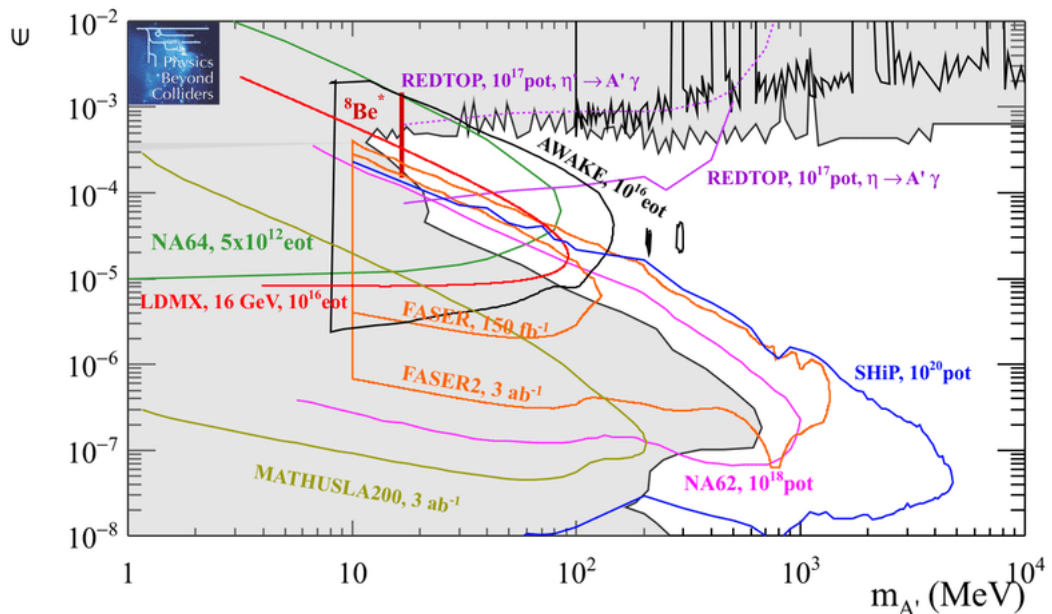
Figure 2.7: Regions explored by various experiments for dark photon mass in function of the coupling strength ϵ' [30].

2.5.2 Heavy Neutral Leptons

Other candidates for dark matter are sterile neutrinos (falling in the more general field of heavy neutral leptons, HNLs). The Standard Model includes three types of neutrinos that have left-handed chirality (meaning that the directions of spin and motion are opposite). Sterile neutrinos on the other hand are hypothetical particles with right-handed chirality, which means that the weak interaction would not affect them, so they only interact gravitationally. Some particle physics theories support the existence of right-handed neutrinos; this is given by the fact that all the other known fermions have both left and right chirality. These could explain the small neutrino masses given by the neutrino oscillation effect. It is currently theorised that a mixing of standard and sterile neutrinos could lead to a decay of a sterile neutrino into a standard neutrino and a photon or into three standard neutrinos [31]. So far scientists are trying to estimate the range in which these processes occur and currently these HNLs could have masses from below 1 eV up to 10^{15} GeV, which of course is not a very restrictive range. This is still a vast field to investigate and the effort to search for HNLs has increased steadily in recent years [?].

2.5.3 WIMPs

The Weakly Interacting Massive Particles (WIMPs) are presented here; they are classic candidates to explain dark matter. They are hypothetical particles, that would be subject to a yet unknown fundamental force (or gravity) with a strength that is even lower than the weak interaction. This definition leaves a vast series of possibilities to what these particles' properties could be, how they behave and how many different types could exist. Because of that, when looking for a WIMP it is necessary to search at all scales of mass, which cannot be done with only one experiment. Several experiments over last 50 years have tried to look for WIMPs without success. These experiments looked at decay products of these WIMPs, coming from far away from earth like the Fermi-LAT [32] and VERITAS [33]; or at interactions of WIMP with big surface detectors, like CRESST [34], SNOLAB [35] and many others. From the recent results it would appear that the mass of a WIMP, in case it existed should be quite high, meaning at least above 10 GeV and more likely even up to several TeV [36].

Accelerator Physics

The development of particle physics is strongly linked to that of accelerator facilities, that made possible the discovery of most of the elementary particles known nowadays. Accelerator technologies are currently so complex that a new branch of physics is dedicated to them, namely accelerator physics. In this chapter the concepts of accelerator physics relevant for the thesis work are covered. Most of these concepts are linked to optics and beam line elements that are used in beam lines in general and in secondary beam lines, specifically.

3.1 Target and Secondary Beams

A primary beam (protons in the case of the CERN SPS) that interacts with a target produces a secondary beam (see more about secondary beam lines at CERN in Chapter 4). The properties of the target material are important for the production rate and composition of the secondary particles. Every target in the secondary beam lines can serve several beam lines (between one and three in the North Area). Inside each beam line, the beam composition can be additionally modified via a number of methods, e.g. by placing a secondary target downstream of which a lower-momentum tertiary beam is defined.

3.1.1 Target Properties

The 400 GeV/c high-intensity primary proton beam from the SPS is extracted at an intensity on the primary targets between several 10^{12} and 1.5×10^{13} ppp (protons per pulse). When this beam interacts with a target, the rate and composition of the secondary beam depends on the length and material of it, as well as on the momentum and production

39

angle (angle between the primary and secondary beam axis) of the secondary beam. The choice of the target material and length depends mainly on the nuclear interaction length λ_I, the radiation length X_0 and its thermal properties. The nuclear interaction length quantifies the length scale over which the primary particles interact with the nuclei of the material. It also describes the re-absorption through secondary interactions of the secondary hadrons produced. The fraction of non-interacting particles (primary or secondary) decreases exponentially with the parameter λ_I. The number of secondary hadrons produced dN_h per length dL is parameterised approximately by Equation 3.1:

$$\frac{dN_h}{dL} = \frac{L}{\lambda_I} e^{\frac{-L}{\lambda_I}} \tag{3.1}$$

If x is defined as $x = L/\lambda_I \approx L/Xo$ (true in the case of beryllium), where L is the length of the target, the target efficiency ϵ_T can be written as $\epsilon_T(L) = xe^{-x}$ for hadrons and approximately as $x^2 e^{-x}$ for electrons or positrons. The target efficiency for hadrons is therefore maximum when $\frac{\partial \epsilon_T}{\partial x} = 0$, or $(x-1)e^{-x} = 0$, hence $x=1$. It can be observed from this equation that the maximum target efficiency for a beryllium target is $e^{-1} \approx 0.37$ that corresponds to approximately 40 cm of length. This is indeed the length chosen for the T10 target in the NA62 experiment, see Figure 3.1.
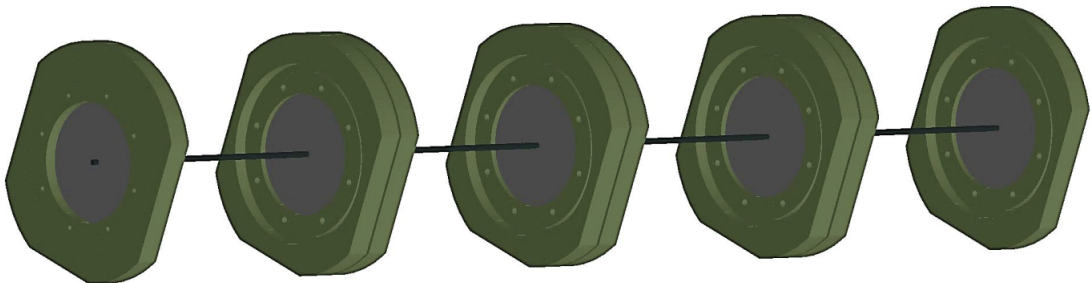
Figure 3.1: T10 target of the NA62 experiment in the North Area. It is composed of four Beryllium rods for a total length of apporximately 40 cm.

3.1.2 Particle Production

Among the particles produced only those sufficiently stable can be transported along beam lines, namely (anti-)protons, charged pions and kaons, electrons and positrons, muons and the neutral particles K_L, K_S, Λ, neutrons and photons. Muons are mainly produced by decays of pions and kaons, therefore downstream of the target. The production rates as

a function of momentum (for momenta above 60 GeV/c) and production angle have been measured by the NA20 collaboration. Those data have also been parametrised in a useful formula, called "Atherton parametrisation" [37], see Equations 3.2 and 3.3.

$$For \quad K^{\pm}, \pi^{\pm}, \bar{p}: \qquad \frac{d^2N}{dpd\Omega} = A\left(\frac{B}{p_0}e^{\frac{Bp}{p_0}}\right)\left(\frac{Cp^2}{\pi}e^{-C(p\theta)^2}\right) \qquad (3.2)$$

$$For \quad p: \qquad \frac{d^2N}{dpd\Omega} = A\left(\frac{B+1}{p_0}\left(\frac{p}{p_0}\right)^B\right)\left(\frac{Cp^2}{\pi}e^{-C(p\theta)^2}\right) \qquad (3.3)$$

In these equations, p, p_0 and θ are the secondary momentum, the primary beam momentum and the incidence angle of the primary beam respectively. The parameters A, B and C vary for different particles and can be found in Table 3.1. This formula is precise to

Particle Type	A	B	C
π^+	0.80	11.5	5
π^-	0.16	8.5	5
K^+	1.2	9.5	3
K^-	0.10	13.0	3.5
$\bar{p}$	0.06	16.0	3.0
p	0.80	-0.6	3.5

Table 3.1: A,B and C parameters for different particles in the Atherton formula.

a few percent for North Area energies, except if used in the very low momenta regions (below 60 GeV/c). In the region below 60 GeV/c the so called Malensek parametrisation is used instead [38]. The flux for various particles can be plotted at different momenta as shown in Figure 3.2. For electrons the parameterisation follows a complex pattern since
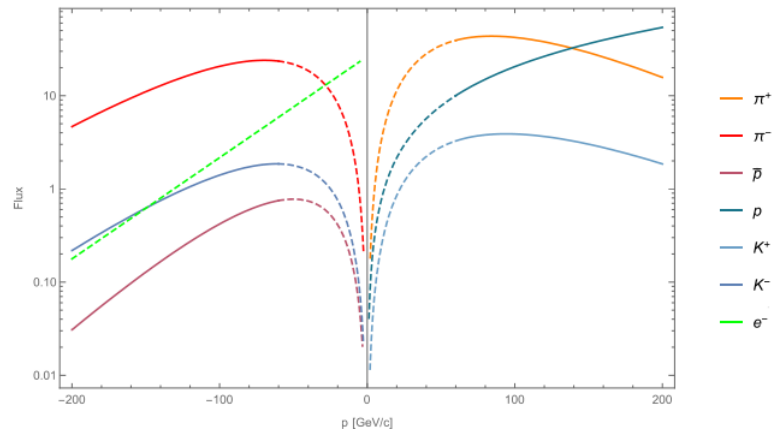
Figure 3.2: Flux calculated for various particles using the Atherton formula at 0 mrad production angle. The flux plots on the negative axis are for the antiparticles. The primary incident beam is a 400 GeV/c proton beam.

they are produced by different processes (mainly π^0 decays) and afterwards multiply in electromagnetic showers. A fit of simulations and data from the H3 beam line (a CERN secondary beam line) show that the production rate of electrons can be expressed via Equation 3.4.

$$\frac{d^2N}{dpd\Omega} = A\left(\frac{B}{p_0}e^{-\frac{Bp}{p_0}}\right)\left(\frac{Cp_0^2}{\pi}e^{-C(p\theta)^2}\right) \tag{3.4}$$

With $A = 0.0023$, $B = 10.0$ and $C = 9.0$ [39].

3.2 Magnets

The motion of particles within magnets (as in general for electromagnetic fields) is described by the Lorentz force $\boldsymbol{F_L}$ given by the relation:

$$\boldsymbol{F_L} = q(\boldsymbol{E} + \boldsymbol{v} \times \boldsymbol{B}) \tag{3.5}$$

Where $\boldsymbol{E}$ is the electric field, $\boldsymbol{v}$ the velocity of the particle and $\boldsymbol{B}$ is the magnetic field. For high-energy particles, the absolute value of the velocity, v, is close to the speed of light and for this reason the contribution to the force of the second term $(\boldsymbol{v} \times \boldsymbol{B})$ is the dominating one. This is why magnetic fields are used in accelerators, rather than electric fields. There are different types of magnets, categorised by the number of poles: dipoles, quadrupoles, sextupoles, and so on [40]. Not all these magnets are used in secondary beam lines, with dipoles (also called bending magnets) and quadrupoles being the most common ones. In this section only non-permanent magnets will be discussed, these are magnetised with the use of coils wrapped around their yokes.

The concepts presented here can be extended to superconducting magnets; these are not commonly used as secondary beam line elements and hence will not be covered in detail in this chapter.

3.3 Multipole Magnets

In accelerator physics a three-dimensional field is usually described with the xy components in the transverse plane relative to the beam and the z component in the longitudinal one, this convention is used in this thesis as well. A magnetic field $\boldsymbol{B} = (B_x, B_y, B_z)$ with constant B_z and described in a xy complex plane via Equation 3.6 satisfies Maxwell's
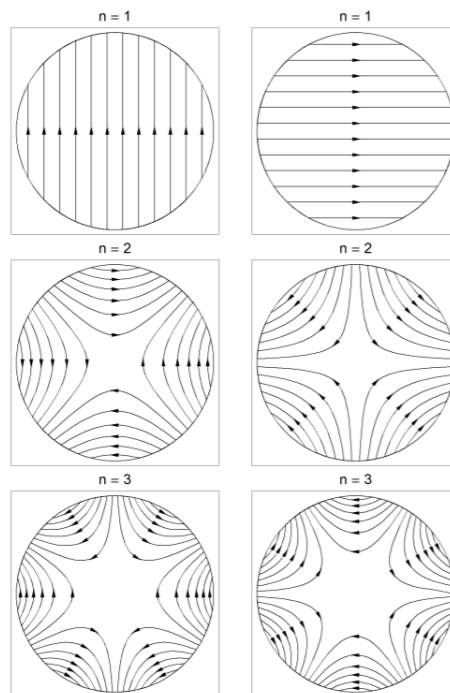
Figure 3.3: Magnetic fields in the transverse plane for multipole magnets [40].

equations.

$$B_x + iB_y = \sum_{n=1}^{\infty} C_n(x + iy)^{n-1} \tag{3.6}$$

Fields of this form are known as multipole fields [40], see Figure 3.3. These fields can be defined as normal or skew according to their orientation. In Figure 3.3 the elements on the left are defined as normal and the ones on the right as skew. The index n (an integer) indicates the order of the multipole where n = 1 is a dipole, n = 2 is a quadrupole, n = 3 is a sextupole, and so forth. The coefficients C_n are complex coefficients that depend on the magnetic field. It can be seen from these expressions that a normal dipole has a uniform vertical field, a normal quadrupole has a vertical field for y = 0, that grows linearly in x, and that a normal sextupole has for y=0 a vertical field that grows with the square of x.

3.3.1 Dipole Magnets

Dipole magnets are used to bend particles in a beam line. Dipoles usually contain two coils (can be one or more) wrapped around their yokes that generate a field which moves from the north to the south pole creating a region with a homogeneous field. See in Figure 3.4 the most common type of bending magnets in secondary beams, called H-shape and C-shape.
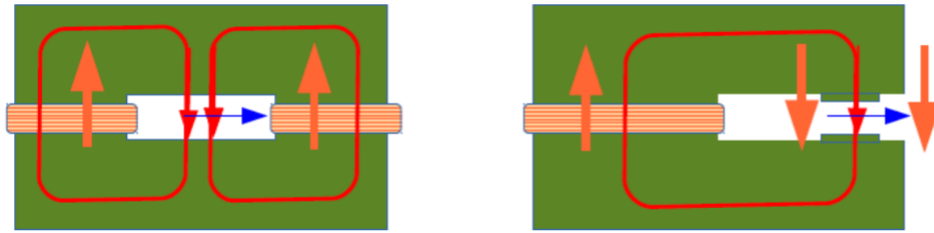
Figure 3.4: Schematic view of a H-shaped magnet (on the left) and a C-shaped magnet (on the right). The direction of the magnetic field lines is schematically shown in red and the deflection in blue (for a negatively charged moving perpendicularly and into the plane of the page). The orange arrows indicate the relative orientation of the return fields [39].

Using the Lorentz force it can be shown that a charged particle entering such a region with a velocity non-parallel to the field (in which case the force would be 0) would be bent along a curve. This bending effect is expressed by the magnetic rigidity, $B\rho$ [41]:

$$B\rho = \frac{p}{q} \tag{3.7}$$

where p is the particle momentum, q the particle charge, ρ the curvature radius and B is the field in the magnet (assuming that this is homogeneous and constant along the magnet length). This is an important equation in accelerator physics and can be used in accelerators to calculate the magnetic field needed in the dipoles to steer a desired beam energy. This equation can also be reformulated to show that the angle at which a bending magnet would bend is:

$$\theta \text{ [mrad]} = 0.29979 \frac{BL \text{ [Tm]}}{p \text{ [GeV/c]}} \tag{3.8}$$

Where L is the length of the magnet.

Some smaller bending magnets are also referred to as corrector or trimmer magnets, which have relatively low bending strength compared to the bending magnets and help to steer or correct the beam trajectory if needed.

3.3.2 Quadrupole Magnets

Propagating particles, like light, when travelling freely, tend to spread out (see the definition of emittance later in this chapter). For this purpose there is the need to use a focusing device within a beam line. In accelerators quadrupoles are used for this purpose [42]. A beam entering a quadrupolar magnetic field with a velocity non parallel to the field would

be focused in one direction (x, for example) but defocused in the other perpendicular direction. Quadrupoles which focus in one plane are combined with ones which focus in the other, such that the net effect is focusing in both planes. The combination of these focusing and defocusing quadrupoles in a beam line is called a focusing-defocusing (FODO) cell. The strength of a quadrupole is usually quantified via the focusing coefficient k [42]:

$$k \; [\text{m}^{-2}] = 0.29979 \frac{g \; [\text{T/m}]}{p \; [\text{GeV/c}]} \qquad (3.9)$$

Where g is the field gradient of the quadrupole that is defined as the ratio between the field at pole edge divided by the pole edge distance from the center of the quadrupole.

3.3.3 Sextupole Magnets

As mentioned in the beginning of this section, in a beam line mostly bending and quadrupole magnets are used and this is the case of secondary beam lines as well. For some complex systems there might be a problem with chromatic aberrations, this means that particles with slightly different energies are differently focused by the quadrupoles, slightly distorting the beam. In light optics such aberrations can be partially corrected by the use of glasses with different refractive indices. In particle optics sextupoles are used for this purpose. Aberration effects are generated in accelerators by the quadrupole field contribution at higher orders and can be cancelled out by the corresponding terms of sextupolar fields [43]. In other words, it can be shown that by placing a sextupole in a point at which the particles have a non null dispersion the field strength of the magnet can be set so that all particles with energy offsets are focused to the same point.

3.4 Collimators

A collimator is an element made of heavy materials with a high stopping power that defines the acceptance of the beam. Collimators can have adjustable apertures in either one or two planes, respectively, or a fixed aperture. The (typically major) part of the beam passes within the aperture limits of the collimator while the particles beyond its acceptance interact in the material and get absorbed, scattered or undergo inelastic interactions. In CERN's experimental areas beam lines lengths of these elements range between 5-10 λ_I, where λ_I is the nuclear interaction length of the material. Therefore, when the beam passes through the material the flux will be reduced by a factor proportional to $e^{-\lambda_I}$ [44].

More details on collimators are given in Chapter 6 with a special overview of collimators for secondary beams.

3.4.1 Sweeping magnets

Beam lines contain also magnets that are used to "clean" the beam from a certain component that is undesired. This is the case for a beam that interacting with some material generates showers of particles that propagate forward together with the beam generating potential background for the experiment [45]. This process is relevant for example for high
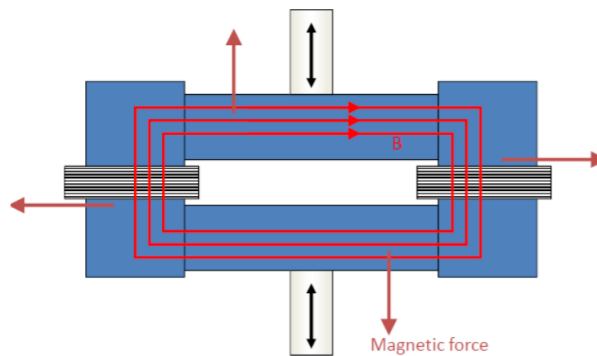
Figure 3.5: Schematic illustration of a muon sweeper. It can be seen in the center the field-free region and the magnetic lines in the yoke.

energy muons that once created tend to not interact with matter (since they have a low interaction cross section) and propagate undisturbed for long distances possibly generating background in the experiment detector.

Sweeping magnets (also called scraper magnets) are toroidal magnets or magnetised blocks that let the core of the beam propagate through a field-free region, removing via the field in the yoke the undesired part (e.g. muons) [46]. See an example of such a magnet in Figure 3.5. This figure shows a muon sweeper that lets the beam pass through the field-free region in the center of the magnet and deviates out the muons interacting with the magnetic field of the yoke (the scattering of the particles in the material contributes to this process as well). A similar system is used in the NA62 experiment [1], where a series of three sweeping magnets is used to reduce the muon halo generated along the beam line.

3.5 Beam Monitors and Detectors

Magnets and collimators are the beam line elements used to modify the beam parameters, but are not the only elements used. Other instruments are usually placed along a beam line

to measure the beam properties (intensity, beam-size, divergence, particle type and so on) in a certain location; these are the beam monitors (detectors). The intensity can be measured with scintillators [47] or ionisation chambers [39], that count the number of particles crossing the active material. For the beam size and divergence measurements, gaseous detectors are commonly in use, like Multi Wire Proportional Chambers, MWPC [48]. The particle identification is usually achieved using Cherenkov detectors, like the CEDAR counters [49], or via the time of flight reconstruction technique. The CEDAR counters are described in the next subsection since play an important role for the NA62 experiment.

3.5.0.1 CEDAR

CEDAR counters are CErenkov Differential counters with Achromatic Ring focus. They are called differential because of the use of optical focusing and/or geometrical masking to select particles having velocities in a specified region. These counters are available in some of the CERN secondary beam lines to perform particle identification for individual particle types.
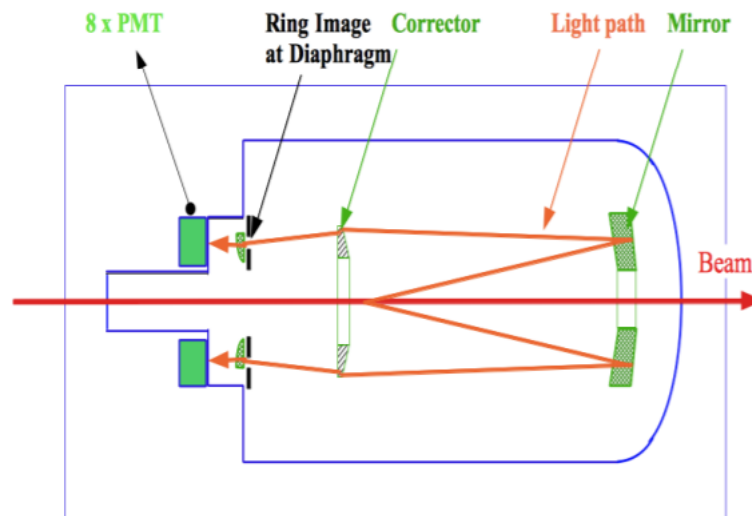
Figure 3.6: CEDAR detector schematic [50]. It can be seen that the light generated by the passing beam is reflected on the internal mirrors and redirected on the light detectors (PMTs in this case).

CEDARs are basically tanks filled with gas (e.g. nitrogen or hydrogen) that works as an active material and contain a system of mirrors and lenses to reflect and focus the light generated in the gas. These detectors make use of the Cerenkov effect, an effect that takes place when a particle moves at higher speed than light in a certain material

generating a cone of light. The Cerenkov equation states that this light is produced at an angle:

$$cos(\theta_c) = \frac{1}{n\beta} \tag{3.10}$$

where n is the refractive index of the material and $\beta = v/c$. The light produced in the CEDAR is reflected by the mirror at the downstream side of the detector and focused in order to give a ring image that is different in radius and can be distinguished for different particles masses (see Figure 3.6). It can be shown that two particles with two different masses m_1 and m_2 lead to a difference in the ring radii:

$$\Delta R = \frac{f}{\theta_c} \frac{m_2^2 - m_1^2}{2p^2} \tag{3.11}$$

f is the focal length of the system and p is the momentum of the particle [49].

3.6 Hamiltonian Approach and Transfer Maps

The present section describes the motion of particles along an ensemble of magnets. The most convenient coordinate system to describe particle motion in a lattice is the Frenet-Serret system [51] [52] that follows the particle along the reference path. This means that it is a curvilinear coordinate system. Figure 3.7 shows a vector $\mathbf{t}$ tangent to the curve, a vector $\mathbf{n}$ normal to the curve, and a vector $\mathbf{b}$ to complete the basis. The constant of curvature k defines the radius of the arc, while the initial condition n_0 defines the angle of the plane containing the arc. Numerically, particle dynamics can be described by integrating the equations of motion for a particle in a field, using an integration algorithm. This type of integrator solves the dynamic for initial coordinate values and can track the particle propagating through a magnet. This requires knowledge of the magnetic field along the trajectory of the particle. However, the obtained result would not give any indication of how changes in the initial values will affect the final values, this means that the integrator must be run separately for each set of initial values that may be of interest. If some studies require tracking many particles and iterate many times this approach can be quite time consuming. The solution to this problem in accelerator physics is to construct a so called "transfer map", which expresses in functional form the dependence of the final values of the dynamical variables in terms of the initial values. A transfer map can be constructed using a mode decomposition of the magnetic field and integrating this
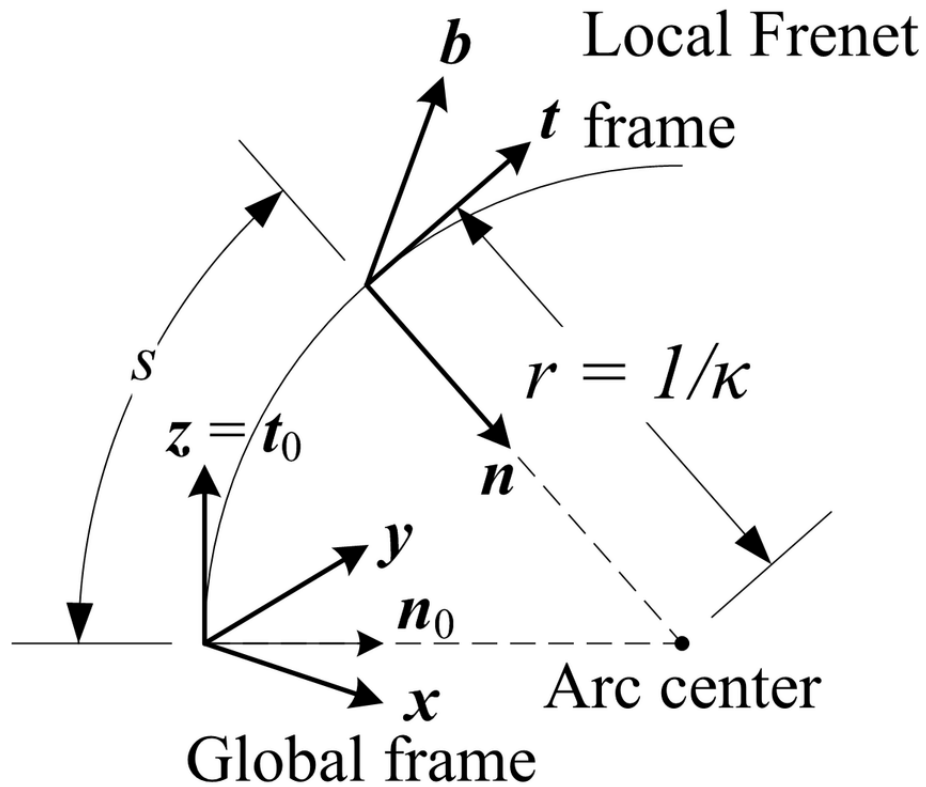
Figure 3.7: Frenet-Serret coordinate system [53].

as it would be done for the numerical integration. The result of the integration is a set of power series, one for each dynamical variable. Once the transfer map has been obtained (by a single integration through the cell), tracking particles simply involves evaluating the power series for the given initial values of the dynamical variables [54]. These variables are usually expressed using the Hamiltonian formalism shown in the next section.

3.6.1 Accelerator Hamiltonian

The Hamiltonian formalism is the most commonly used one in accelerator physics. In this formalism the dynamical variables used for the description of a particle propagating into an electromagnetic field can be chosen to be: x and y, the coordinates in a plane transverse to the reference trajectory; p_x and p_y are the normalised momenta given by:

$$p_x = \frac{\gamma m \dot{x} + q A_x}{p_0}, \tag{3.12}$$

$$p_y = \frac{\gamma m \dot{y} + q A_y}{p_0}, \tag{3.13}$$

where γ is the relativistic factor for the particle, m and q are the mass and charge of the particle, A_x and A_y are the transverse components of the electromagnetic vector potential, and p_0 is the fixed reference momentum. A dot indicates the derivative with respect to time. The longitudinal coordinate z of a particle is defined by:

$$z = \frac{s}{\beta_0} - ct \qquad (3.14)$$

where β_0 is the relativistic β for a particle with the reference momentum, and t is the time at which the particle arrives at a point s along the reference trajectory. The energy deviation δ, is defined by:

$$\delta = \frac{E}{p_0 c} - \frac{1}{\beta_0} \qquad (3.15)$$

where E is the energy of the particle. With these variables, the Hamiltonian describing the dynamics of a charged particle is:

$$H = \frac{\delta}{\beta_0} - \sqrt{\left(\delta + \frac{1}{\beta_0}\right)^2 - \left(p_x - \frac{qA_x}{p_0}\right)^2 - \left(p_y - \frac{A_y}{p_0}\right)^2 - \frac{1}{\beta_0^2 \gamma_0^2}} - \frac{qA_z}{p_0} \qquad (3.16)$$

where the zero index refers to the variables corresponding to the reference particle with the usual meanings. It is also important to note that the independent variable here is path length s, not time, which are the Frenet-Serret coordinates. This Hamiltonian can be solved calculating the usual Hamiltonian coordinates:

$$\frac{dp_i}{dt} = \frac{\partial H}{\partial q_i}, \qquad (3.17)$$

$$\frac{dq_i}{dt} = -\frac{\partial H}{\partial p_i}. \qquad (3.18)$$

The Hamiltonian defined before cannot anyway be solved analytically because of the presence of the square root. For this reason the expression is approximated by a Taylor series taking into account only terms at the second order; this approximation is usually called paraxial and is valid only for particles that are at small angles and near the reference path [54].

3.6.2 Linear Transfer Maps

If the equations of motion are linear, transfer maps can be written as matrices. In this formalism a particle with initial coordinates $\boldsymbol{x_1}$ propagating in a series of n elements

represented by maps (matrices) M_i transforms to a final state with coordinate $\boldsymbol{x_2}$ via:

$$\boldsymbol{x_2}(\boldsymbol{s}) = M_n(s)...M_2(s)M_1(s)\boldsymbol{x_1}(\boldsymbol{s}) \tag{3.19}$$

It can be shown as an example, the calculation of the transfer map for few elements: drift, bend and quadrupole. For a drift there are not electric or magnetic fields therefore potentials can be set to 0. After expanding to second order Equation 3.16 and dropping terms of third and higher orders the Hamiltonian for a drift becomes:

$$H_{drift} = \frac{p_x^2}{2} + \frac{p_y^2}{2} + \frac{\delta^2}{2\beta_0^2\gamma_0^2} \tag{3.20}$$

Using the Hamilton Equations 3.17 and 3.18 these relations can be put in matrix form.

$$R_{drift} = \begin{pmatrix} 1 & L & 0 & 0 & 0 & 0 \\ 0 & 1 & 0 & 0 & 0 & 0 \\ 0 & 0 & 1 & L & 0 & 0 \\ 0 & 0 & 0 & 1 & 0 & 0 \\ 0 & 0 & 0 & 0 & 1 & \frac{L}{\beta_0^2\gamma_0^2} \\ 0 & 0 & 0 & 0 & 0 & 1 \end{pmatrix} \tag{3.21}$$

where L is the length of the drift. Given the 6-vector $\boldsymbol{x}$, $\boldsymbol{x} = (x, p_x, y, p_y, z, \delta)$ the coordinates of this particle would transform as $\boldsymbol{x_1}(\boldsymbol{s}) = R_{drift}\boldsymbol{x_2}(\boldsymbol{s})$.

For bending magnets the second order Hamiltonian takes the form:

$$H_{bend} = \frac{p_x^2}{2} + \frac{p_y^2}{2} + (k_0 - h)x + \frac{1}{2}hk_0x^2 - \frac{h}{\beta_0}x\delta + \frac{\delta^2}{2\beta_0^2\gamma_0^2} \tag{3.22}$$

Where $k_0 = \frac{q}{p_0} B_0$ is the normalised dipole field strength. Following the same approach used for the drift can be shown that the transfer matrix of a dipole is:

$$
R_{bend} = \begin{pmatrix}
\cos(\omega l) & \frac{\sin(\omega l)}{\omega} & 0 & 0 & 0 & \frac{1-\cos(\omega L)}{\omega\beta_0} \\
-\omega\sin(\omega l) & \cos(\omega l) & 0 & 0 & 0 & \frac{sin(\omega L)}{\beta_0} \\
0 & 0 & 1 & L & 0 & 0 \\
0 & 0 & 0 & 1 & 0 & 0 \\
-\frac{sin(\omega L)}{\beta_0} & -\frac{1-cos(\omega L)}{\omega\beta_0} & 0 & 0 & 1 & \frac{L}{\beta_0^2\gamma_0^2} - \frac{\omega L - sin(\omega L)}{\omega\beta_0^2} \\
0 & 0 & 0 & 0 & 0 & 1
\end{pmatrix}
\tag{3.23}
$$

This matrix is calculated in the assumption that the reference trajectory is matched to the dipole strength, $\omega = \frac{1}{r} = k_0$.

For quadrupoles the Hamiltonian takes the form of:

$$
H_{quad} = \frac{p_x^2}{2} + \frac{p_y^2}{2} + \frac{\delta^2}{2\beta_0^2\gamma_0^2} + \frac{k_1}{2}(x^2 - y^2)
\tag{3.24}
$$

Once again using Equations 3.17 and 3.18 it can be shown that the corresponding transfer matrix is [41]:

$$
R_{quad} = \begin{pmatrix}
\cos(\omega l) & \frac{\sin(\omega l)}{\omega} & 0 & 0 & 0 & 0 \\
-\omega\sin(\omega l) & \cos(\omega l) & 0 & 0 & 0 & 0 \\
0 & 0 & \cosh(\omega l) & \frac{\sinh(\omega l)}{\omega} & 0 & 0 \\
0 & 0 & 0 & \omega\sinh(\omega l) & \cosh(\omega l) & 0 \\
0 & 0 & 0 & 0 & 1 & \frac{L}{\beta_0^2\gamma_0^2} \\
0 & 0 & 0 & 0 & 0 & 1
\end{pmatrix}
\tag{3.25}
$$

3.6.3 Transverse Motion in a Lattice

From the Hamiltonian shown above can be proven that the motion of a particle in the transverse plane can be described by the so-called Hill's equations [55]:

$$
u''(s) + K(s)u(s) = 0
\tag{3.26}
$$

Where k is a function of s and u indicates both the x and the y coordinate. The principal solutions of these equations are in the form of:

$$u(s) = \sqrt{\epsilon}\sqrt{\beta(s)}\cos(\phi(s) + \phi_0) \tag{3.27}$$

where β is referred to as the beta function, and is a position-dependent amplitude, and ϵ is a constant of motion, $\phi(s)$ is the phase advance that depends also on the focusing strenght and ϕ_0 is an integration constant depending on initial conditions.

3.6.4 Twiss parametrization

The solutions exposed above are usually parametrised using the so called Twiss parameters. The Twiss parameters use the fact that the beam is an ellipse in phase-space (the
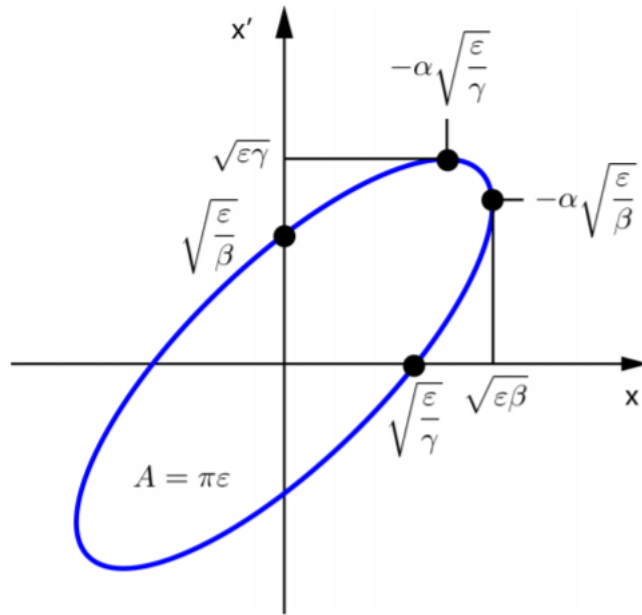
Figure 3.8: Twiss Parameters of a beam in x and x' (phase-space).

area of which is the emittance [56]) and therefore the quantity ϵ can be expressed (in one direction, e.g. x) as:

$$\epsilon_x = \gamma_x x^2 + 2\alpha_x x x' + \beta x'^2 \tag{3.28}$$

with $x' = dx/ds$, and:

$$\gamma_x = \frac{1 + \alpha_x^2}{\beta_x} \tag{3.29}$$

This leads to the formula:

$$\int xx' = \pi \epsilon_x \tag{3.30}$$

With ϵ_x being the beam emittance. For a Gaussian with zero dispersion the beam-size is defined as $\sigma_x = \sqrt{\epsilon_x \beta_x}$. In accelerator physics ϵ is referred to as the emittance and obeys Liouville's theorem, which states that particle density in phase space is conserved along all trajectories. This is true only if there is no time dependence on the Hamiltonian, i.e. when the beam energy is constant. This is for example not the case for accelerated beams and beams that interact with collimators. For accelerated beams the normalised emittance ($\epsilon_n = \beta \gamma \epsilon$) is a conserved quantity instead. The twiss parameters are particularly useful for machines and transfer lines where ideally the emittance is conserved. In secondary and tertiary beam lines, this is normally not the case, as collimation is necessary to define the central momentum and the width of the momentum band transported. Therefore, the optics design is usually based on the transfer matrix approach.

Chapter 4

CERN Secondary Beam Lines and North Area Experiments

This chapter introduces the general structure of the CERN accelerator complex with a focus on secondary beam lines and their experiments. Among these, the experiments served by the K12 beam line that represent, all together with its possible future upgrades, the core of this thesis. The discussion mainly focuses on the structure of the detector and the physics goals of these experiments, whilst the beam lines structure and simulations will be discussed in more detail in the following chapters.

4.1   CERN Accelerator Complex

The Large Hadron Collider (LHC) is the biggest accelerator in the world reaching a center of mass collision energy of 13 TeV. The complex of the LHC crosses the border between Switzerland and France. It is mostly operated as a proton-proton (p-p) collider but can also be operated as an ion-ion collider. For p-p collisions, the first accelerator in the chain is Linac 4 that accelerates protons to an energy of 160 MeV (see Figure 4.1). The beam is then injected into the Proton Synchrotron Booster, which accelerates the protons to 2 GeV/c, followed by the Proton Synchrotron (PS) which brings the beam to 24 GeV/c. Protons are then sent to the Super Proton Synchrotron (SPS) where they are accelerated to up to 400 GeV/c. In the final step, protons are transferred to the LHC where they reach their maximum energy of up to 6.5 TeV. These protons are finally divided in two counter-rotating beams that are afterwards led to collision at the four detectors: ALICE, ATLAS, CMS and LHCb. The total energy at the collision point is equal to 13 TeV [58].
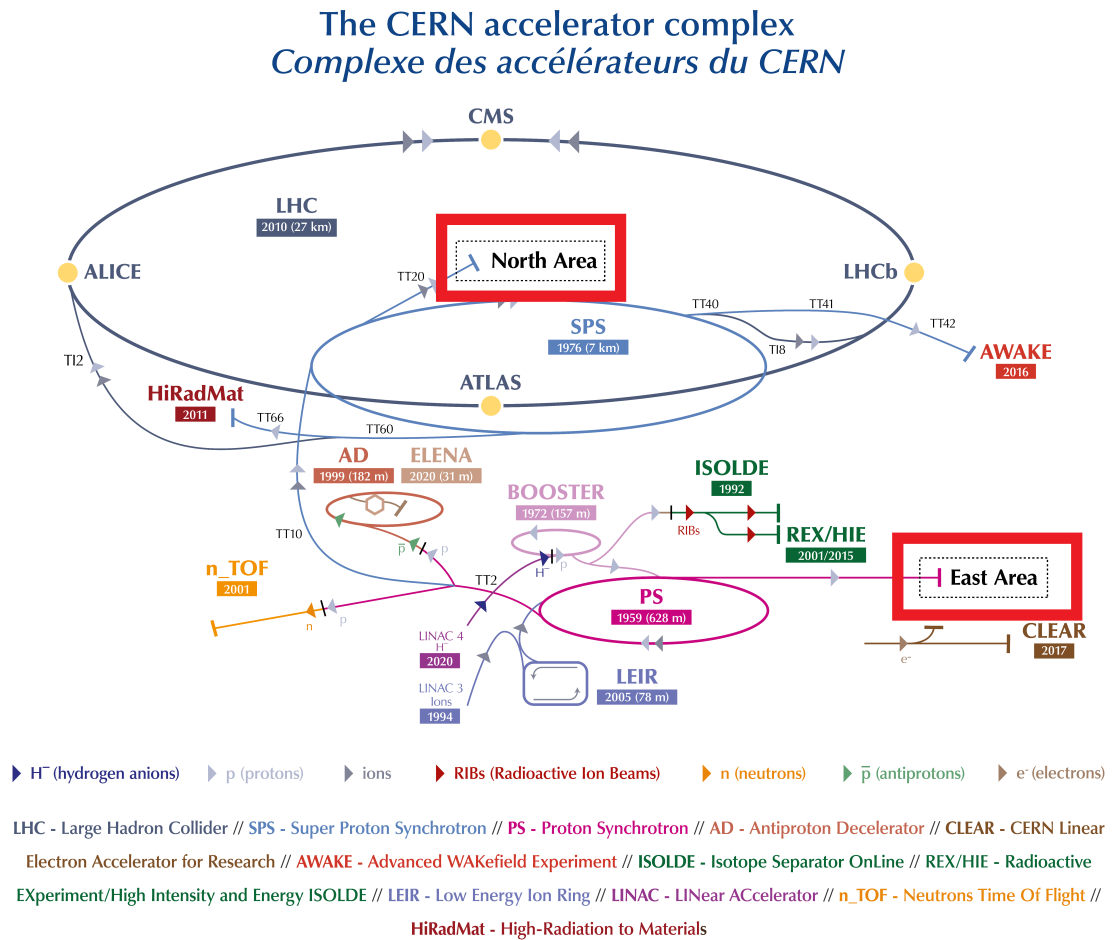
Figure 4.1: CERN accelerator complex layout. The North and East Areas are highlighted in red [57].

The PS and the SPS play an important role in the accelerator chain for the LHC but are also important for other activities. For example these two accelerators slowly-extract particles at low energies (compared to the LHC) that feed the so-called "secondary beam lines". Most of these beam lines are located into two areas at CERN, the North Area (beam extracted from the SPS) and the East Area (beam extracted from the PS) and are used as facilities for test beam as well as to host a series of fixed target experiments [39].

4.2 CERN Secondary Beam Lines

The CERN secondary beam lines in the North and the East Areas are designed to deliver beams of secondary and tertiary particles as well as attenuated primary protons and ions (the primary protons are extracted from the PS and SPS at 24 GeV/c and 400 GeV/c

respectively). The East Area beam lines are located next to each other and shielded with concrete and iron blocks as can be seen in Figure 4.2. The SPS North Area experiments are housed in different experimental halls, two on the surface, EHN1 and EHN2, as well as an underground cavern, ECN3. The beam lines in these areas deliver secondary and tertiary beams of hadrons, electrons and muons in the energy range $< 360\,\mathrm{GeV/c}$, typically at a maximum flux of 10^7–10^8 particles/spill (for secondary and tertiary beams). Primary
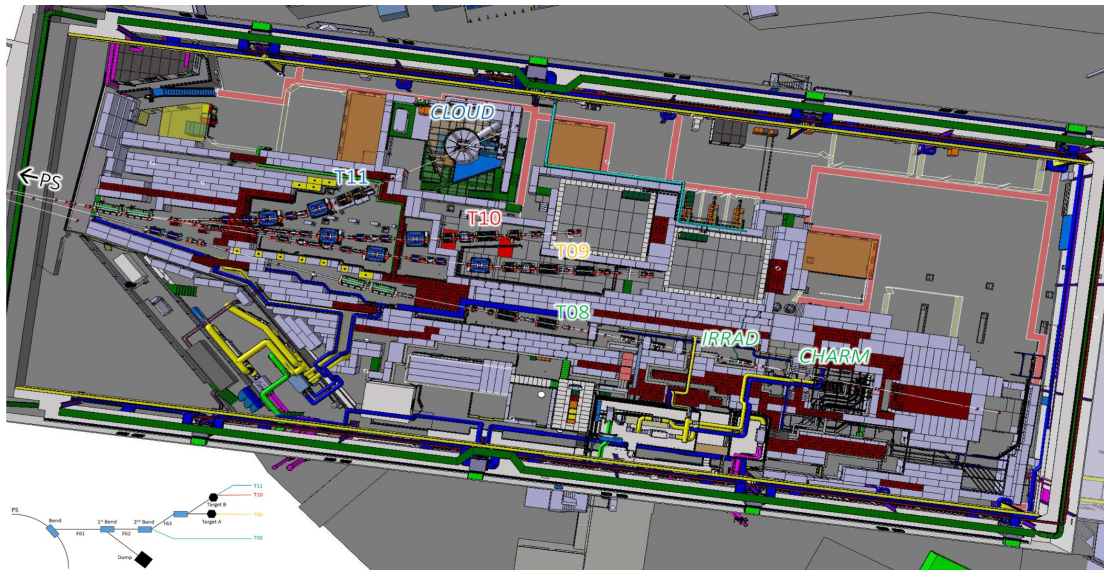
Figure 4.2: CERN East Area top view in CAD. The main beam lines (T8, T9, T10 and T11) and the relative experiments are highlighted [59].

beams are attenuated to similar intensities in the surface halls as well. The East Area delivers beams of mixed/pure hadrons, electrons and muons in the momentum range $< 15\,\mathrm{GeV/c}$ at a maximum flux of few $\times 10^6$ particles/spill.

4.2.1 Fixed Target Experiments at Secondary Beam Lines

In fixed-target experiments (FT), primary particles collide with a stationary target, producing secondary particles that can be studied for several purposes. Fixed-target experiments are easier to install and operate compared to experiments at big colliders; they allow a better beam particle type and momentum selection and have higher event rate. The disadvantage of FT experiments is in the collision energy that is much lower than the one that can be reached at colliders. The energy, s, in the center of mass at a fixed target experiment scales with the beam energy $s \approx \sqrt{m_p E}$, where m_p is the mass of the colliding

particle and E its energy; lower than $s \approx 2E$ achievable in colliders. CERN hosts a series of fixed-target experiments in the East Area and the North Area, e.g. NA62, NA61 [60], COMPASS [61], CLOUD [62] and NA64 [63]. The physics studied in these experiments is mainly focused on precision studies and ranges from kaon physics with NA62, atmospheric physics with CLOUD to the investigation of hadronic interactions and sub-atomic structure with NA61 and COMPASS.

4.3 Kaon Experiments at the North Area

The North Area (see Figure 4.3) has been hosting several fixed target experiments in more than 40 years of operation. The kaon program started in 1989 with the NA31 experiment that gave the first hint of direct CP violation afterwards confirmed by its successor, the NA48 experiment and kTeV at Fermilab. More details on NA48 and CP violation can be found in Chapter 2. After the operation of NA48 [22] a new kaon experiment followed it, NA62, that started physics data taking in 2015. As it is shown in detail in the next section, the main goal of NA62 is to measure rare charged kaon decays. Currently several projects are being considered for the future of NA62. The different proposed experiments are introduced in more detail in this chapter and studied in depth in the framework of this thesis.

4.4 The NA62 Experiment

NA62 studies the very rare decay channel $K^+ \to \pi^+ \nu \overline{\nu}$. The main goal of the experiment is to investigate this decay to extract the CKM parameter $|V_{td}|$ to a 10% precision level (See Chapter 2 for an overview of the CKM matrix properties). This is achieved via the measurement of the π^+ that comes from the K^+ decay with no other particles detected (since neutrinos are not visible in the detector). This measurement is performed with a series of detectors as shown in the next section. The experiment is schematically depicted in Figure 4.4. It has a total length of approximately 270 m and inherited some of the detector components from NA48. NA62 receives particles originally extracted from the SPS. The proton beam coming from the SPS is transported to a primary target (T10) via the P42 beam line. Protons colliding with this target create secondary particles that are selected (positively charged particles at 75 GeV/c momentum) in the K12 beam line. The K12 beam line elements are only briefly introduced here and are described in greater

Figure 4.3: Satellite view of the North Area at CERN. Beam lines and experimental halls are highlighted in the figure [64].
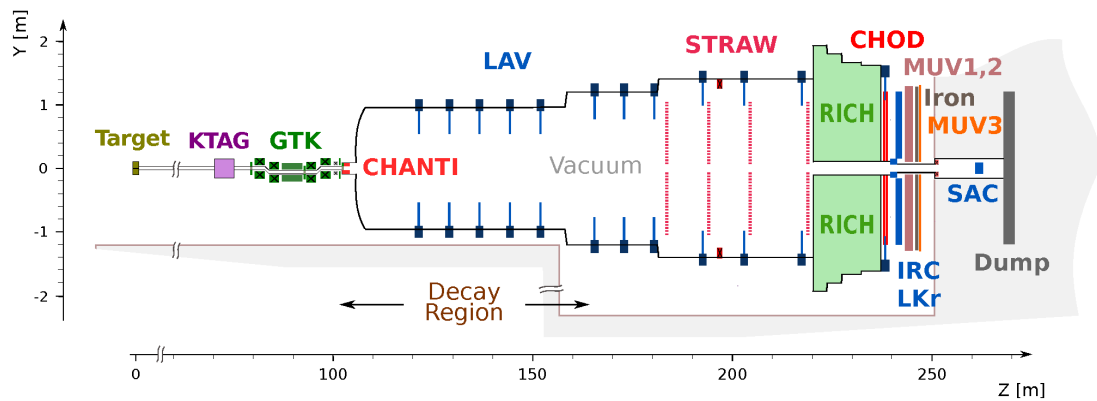
Figure 4.4: Schematic view of the NA62 experiment [50].

detail in Chapter 7. Further downstream in K12, the kaons are identified via the CEDAR (also called KTAG), a Cherenkov Differential Counter with Achromatic Ring Focus (see Fig 4.5). Always in K12, kaons traverse the GigaTracKer (GTK) spectrometer, a silicon

Figure 4.5: A photograph of the CEDAR (KTAG) detector located in the K12 beam line of the NA62 experiment [65].

tracking system that is able to measure time, direction and momentum of all the detected particles.

4.4.1 The NA62 Detector

After the GTK, there is the so called CHANTI (CHarge ANTI) detector. This is a charged anti-counter detector mainly designed to veto events with inelastic interactions of the beam with GTK3. These detectors are followed by a 110 m long vacuum tank, which contains the 50 m long fiducial decay volume (FV). A STRAW gas-spectrometer at the end of the FV allows the measurement of momenta of charged decay products. This detector is composed of several straw tubes containing mainly argon and CO_2. The full experiment region is covered by a system of photon-veto detectors that detect photons produced in the decay region (mainly from decaying π^0s) and propagating at angles up to about 50 mrad with respect to the central detector axis. These detectors include: 12 ring Large-Angle photon Veto detectors (LAV), the Intermediate Ring Counter (IRC), the Liquid

Krypton electromagnetic calorimeter (LKr) and Small-Angle (SAC) calorimeters. The Ring Imaging CHerenkov detector (RICH) is located right after the STRAW. It consists of a 17 m long radiator volume filled with neon gas at one atmosphere and allows the separation of electrons, muons, pions, and kaons. The RICH detector is followed by a system of hodoscope counters CHOD constructed from scintillator panels. Four detectors are used for muon vetos (muons could fake a π^+ track) : MUV0, MUV1, MUV2 and MUV3 that are composed of scintillating tiles and iron. All the detectors of NA62 are operated and connected to a high-performance trigger and data acquisition system [50].

4.4.2 Signal Selection

The signal signature of NA62 consists of an incoming K^+ and an outgoing π^+ with no additional particles seen in the detector (neutrinos are not detected). The detected in-
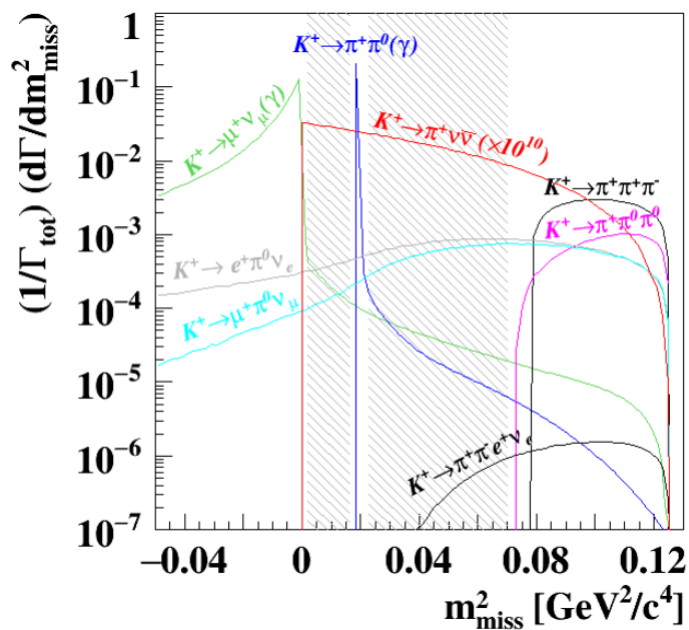
Figure 4.6: Missing squared mass (m^2_{miss}) of K^+ decays for the $K^+ \to \pi^+ \nu \bar{\nu}$. The values are obtained assuming that the particle in the final state is a π^+. The signal is multiplied by a factor 10^{10} in order to be displayed at the same scale. The dashed bands indicate the measuring range of NA62 [66].

coming track, compatible with a kaon, and the outgoing tracks associated in time with the former are used to reconstruct the decay vertex of the kaon. The vertex must be located within the FV. The identification of the downstream particle is performed by combining the RICH measurement with the output of a multivariate classifier using the LKr and the muon veto counters. The main variable used for the analysis is the missing mass

squared $m^2_{miss} = (P_K - P_\pi)^2$, which is calculated using the combination of P_K and P_π measurements. The kaon momentum P_K can be measured directly with the GTK. The pion momentum P_π can be measured either with the STRAWs and with the RICH. The analysis is performed in two separate regions of the m^2_{miss} variable (R1 as [0-0.01] GeV^2/c^4 and R2 as [0.026-0.068] GeV^2/c^4). In both regions the momentum of π^+ has to be in the range $15 - 45\ GeV/c$ to optimise the RICH π^+/μ^+ separation [66].

4.4.3 Backgrounds in the experiment

Different processes happening in the NA62 detector can mimic the signal expected for the $K^+ \to \pi^+\nu\overline{\nu}$ decay. Some of this background comes from K^+ decaying in the fiducial volume while the rest is mainly given by upstream decays. The upstream background events are positively charged pions originated by positively charged kaons that decay or interact in the region upstream of the final collimator. The expected number of signal and background events given by K^+ decays can be seen in Table 4.1. These values for

Process	Expected Events
$K^+ \to \pi^+\nu\overline{\nu}$ IB	$2.16 \pm 0.12_{stat} \pm 0.26_{syst}$
$K^+ \to \pi^+\pi^0(\gamma)$ IB	$0.29 \pm 0.03_{stat} \pm 0.03_{syst}$
$K^+ \to \mu^+\nu_\mu(\gamma)(\mu^+ \to e^+$ decay$)$	$0.11 \pm 0.02_{stat} \pm 0.03_{syst}$
$K^+ \to \mu^+\nu_\mu$	$0.04 \pm 0.02_{syst}$
$K^+ \to \pi^+\pi^-e^+\nu_e$	$0.12 \pm 0.05_{syst} \pm 0.03_{syst}$
$K^+ \to \pi^+\pi^+\pi^-$	$0.02 \pm 0.02_{syst}$
$K^+ \to \pi^+\gamma\gamma$	$0.05 \pm 0.05_{syst}$
$K^+ \to l^+\pi^0\nu_l\ (l = e^+, \mu^+)$	negligible
Upstream Background	$0.9 \pm 0.2_{stat} \pm 0.2_{syst}$
Total Background	$1.5 \pm 0.2_{stat} \pm 0.2_{syst}$

Table 4.1: Expected signal and background events in NA62. $K^+ \to \pi^+\pi^0(\gamma)$ IB and $K^+ \to \mu^+\nu_\mu(\gamma)$ IB include also the contribution from the inner Bremsstrahlung radiation.

the decay backgrounds are estimated via direct independent measurements or via MC simulations. It can be seen from these values how the K^+ decaying to muons creates an important background for the experiment. Accurate simulation models are therefore needed in order to create a precise enough characterisation of these backgrounds.

4.4.4 Main Results of NA62

In 2018 the NA62 detector collected data during 217 days using approximately 10^{18} protons. The analysis of these data led to the reconstruction of 17 signal events coming from

a decay $K^+ \to \pi^+ \nu \overline{\nu}$, out of these. These events follow the ones discovered in 2016 and 2017 (three in total). Combining these data, NA62 proved that this kaon decay rate is $BR(K^+ \to \pi^+ \nu \overline{\nu}) = (10.6^{+4.0}_{-3.4}|_{stat} \pm 0.9_{syst}) \times 10^{-11}$ at 68% CL [2]. This experimental value is compatible with the SM predictions (7.7×10^{-11}) considering the current level of precision achieved. These results represent so far the most precise measurement of this rare decay. The precision of this measurement can be improved with a larger events sample and via a better characterisation of the background. Studies on the background for NA62 are presented in Chapter 7.

4.5 K12 Future Perspectives and Physics Beyond Colliders

New experiments are currently under consideration for the future use of the K12 beam line after the completion of NA62. Studies for these experiments are part (or are foreseen to be part) of the Physics Beyond Colliders study. Physics Beyond Colliders (PBC) is a CERN program that aims at developing a new range of activities in order to extend the scientific potential of the CERN accelerator complex. This program aims at developing experiments that are complementary to the main colliders such as the present LHC, HL-LHC and in future the HE-LHC, CLIC and FCC. These projects would focus on physics topics that are similar to those at high-energy colliders, but that require different types of beams and experiments [3]. The experiments are currently considered within PBC for the K12 beam line in the North Area are: KLEVER, NA62-BeamDump (BD), NA62-HI (higher intensity) and SHADOWS. KLEVER would search for very rare neutral kaon decays instead of charged ones. NA62-HI (also called NA62x4) would run in a similar configuration to NA62 but optimised to a higher proton intensity on target to gain more statistics and achieve a better precision. NA62-BD and SHADOWS would run in approximately the present NA62 configuration (a few minor changes are required), but would focus on a dark matter search. More details about these configurations are given in the next section.

4.6 KLEVER, NA62-BD, NA62-HI and SHADOWS

KLEVER, NA62-BD, NA62-HI and SHADOWS could all be potentially placed in ECN3 and are very different from each other. These four experiments were proposed at different times and therefore the design and preparation of some of them is in a different state of development.

4.6.1 KLEVER

KLEVER aims at Standard Model physics investigations, in particular, measuring the branching ratio of K_L decay into the rare channel: $K_L \to \pi^0 \nu \bar{\nu}$. The probability amplitude for $K^+ \to \pi^+ \nu \bar{\nu}$ (studied by NA62) has both real and imaginary parts, the one for the decay $K_L \to \pi^0 \nu \bar{\nu}$ is purely imaginary. This means that these decays have different sensitivity to new sources of CP violation. Measurements of both BRs would then be useful not only to search for evidence of new physics (beyond the SM) but also to distinguish between these different physics models. Figure 4.7 illustrates a general scheme for the expected beyond SM models accessible via rare decays of K^+ and K_L. KLEVER could
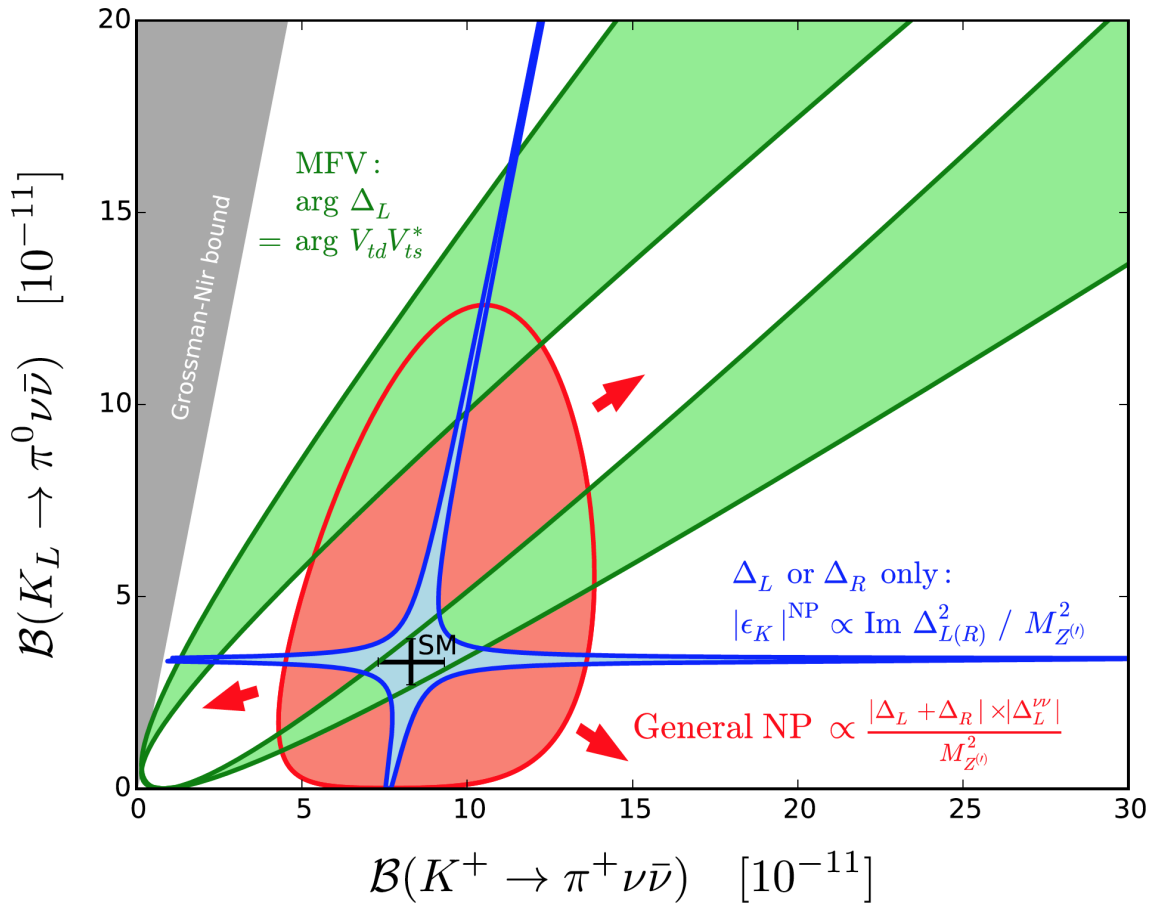
Figure 4.7: SM prediction for $BR(K \to \pi\nu\nu)$ with new potential physics scenarios. The coloured areas represent different potential SM structures. The CKM-like models with minimal flavour violation are in green, the models with flavour-violating interactions with left-handed or right-handed couplings in blue and more general models are in red [4].

start data taking in 2026. Using an intensity of 10^{19} protons on target per year, first estimations predict that the collection of 60 rare decay events are possible over five years of operation [67]. The experiment requires some changes for the P42 beam and a new K12

beam line. The related studies are presented in Chapter 8. First of all, the P42 beam line needs to be modified in order to let the protons hit the T10 target at a non-zero angle. This minimises the Λ background that impacts the number of useful K_L decays, mainly through the $\Lambda \rightarrow \pi^0 n$ channel. The following K12 beam line is arranged to accommodate a neutral beam; this means that many magnets currently used are not necessary for KLEVER (see a detailed description of the K12 beam line for KLEVER in Chapter 7).

4.6.1.1 KLEVER detector

The KLEVER experiment would inherit part of the detector currently in place for NA62, but many components need to be redesigned. For the main electromagnetic calorimeter (MEC) preliminary studies have shown that the liquid krypton calorimeter from NA62 can be reused for the reconstruction of the π^0 signal; alternativly a shashlyk-based calorimeter can be developed ad hoc. A new upstream veto (UV) is required, this UV rejects $K_L \rightarrow \pi^0\pi^0$ decays in the 40 m before the fiducial volume. The UV detector includes an active final collimator (AFC), a LYSO collar counter that provides a last stage of collimation working at the same time as a veto for photons generated by K_Ls. The current LAV of NA62 has too low efficiency to be used in KLEVER and therefore a new one is needed. The new LAV comprises 25 new calorimeters made of lead/scintillating-tile stations with wavelength-shifting fiber readout. A new small-angle calorimeter (SAC) needs to be placed on axis in the neutral beam with the function to reject photons from K_L decays that would otherwise escape downstream the beam line. Finally the last component is the pre-shower detector (PSD) that measures the directions for photons incident on the MEC. Without the PSD, the z-position of the π^0 decay vertex can only be reconstructed by assuming that two clusters on the MEC are indeed photons from the decay of a single π^0. With the PSD, a vertex can be reconstructed by projecting the photon trajectories to the beam line. The invariant mass is then an independent quantity, and $K_L \rightarrow \pi^0\pi^0$ decays with mis-paired photons can be efficiently rejected [4].

4.6.2 NA62-BD

The current configuration of NA62 can be slightly changed in order to accommodate an experiment looking for dark matter. In the current configuration, NA62 uses a massive collimator, the Target Attenuator eXperimental areas (TAX, see Figure 4.9) in order to do a particle momentum selection in the first achromat. This collimator can alternatively
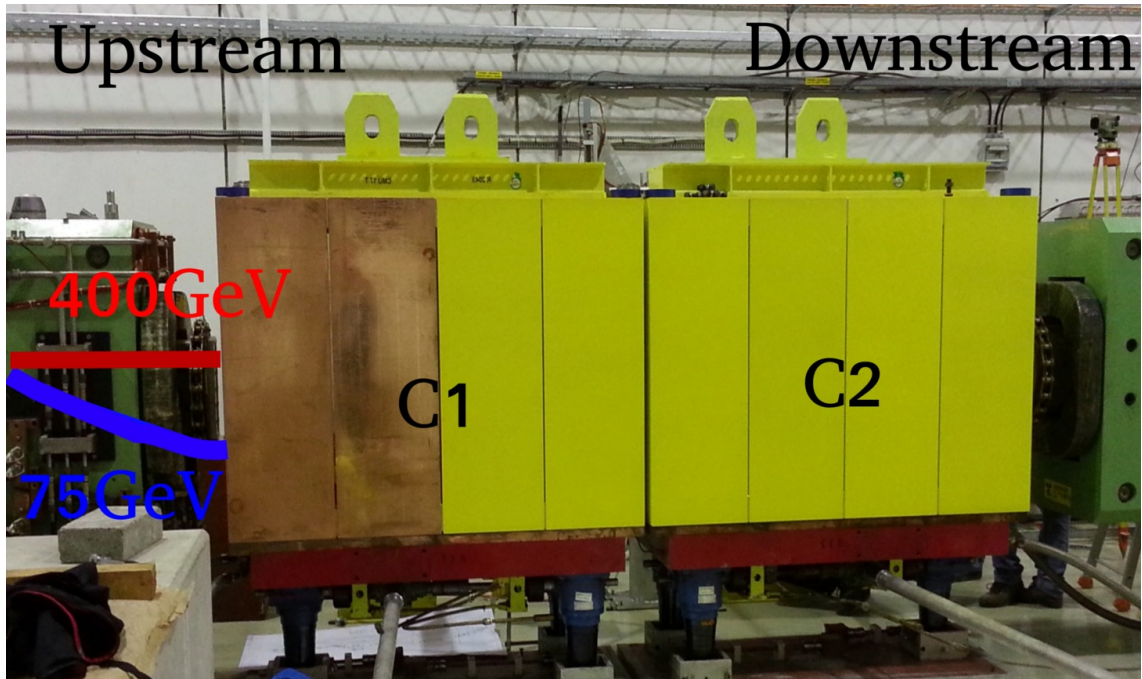
Figure 4.8: Picture of the TAX collimator. It can be seen that the TAX is divided in two blocks, C1 and C2. The first block is made of two layers of copper and two layers of iron, the second block is only made of iron [68].

be closed working effectively as a beam dump (BD). In the NA62-BD configuration the T10 target is removed in order to dump all the protons coming from the SPS (at 400 GeV/c momentum) on the closed TAX collimator. In this mode, called NA62-BD, all the protons and the secondary particles generated are absorbed by the TAX. The TAX is approximately 3.2 meters long and is made of copper and iron. A selection can be therefore made to look for particles that after going through the full collimator length, manage to escape undisturbed. These particles have to interact with forces that are not part of the Standard Model (they would be otherwise absorbed by the TAX), like dark matter candidates are expected to do. The dark matter candidates are not directly observed but the generated secondary particles (generated via decay or annihilation) can be detected in the NA62 detector. For these candidates, the signal expected is a few tracks in the NA62 detector and no other activity. In this configuration the experiment has a competitive sensitivity to dark sector candidates, such as Heavy Neutral Leptons and the dark photon. As an example, it can be considered a dark photon produced in a meson decay from the beam dump, producing visible decays such as: $A' \rightarrow e^+ e^-$ and $A' \rightarrow \mu^+ \mu^-$. Figure 4.9 shows the region explored by NA62-BD for dark scalars. In 2016 NA62 collected data at different intensities in the NA62-BD configuration and the preliminary analysis of these
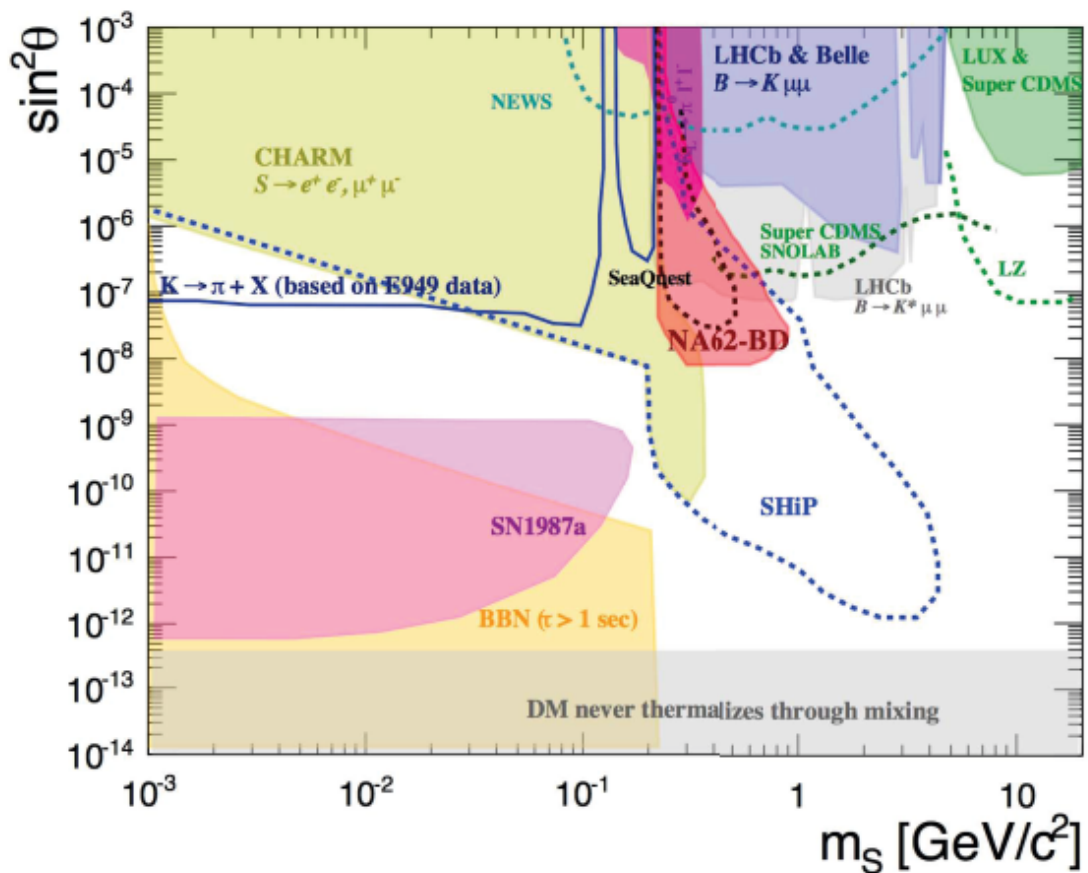
Figure 4.9: Sensitivity of NA62 for 10^{18} protons on target (the shaded region labelled as NA62-BD corresponds to a 90% confidence level exclusion limit) for a dark scalar originated by the dump. The y-axis there is the sine of the mixing angle with the Higgs sector and on the x-axis is the mass of the scalar [69].

data indicates that a zero-background condition could be achieved [69]. This hypothesis is also supported by studies on the K12 beam line optimisation that show how to reach a significant reduction for the muon background [70]. A detailed analysis on the NA62-BD background is also done in Chapter 8. The NA62 collaboration is currently considering to run the experiment in this configuration after LS2 for a duration of approximately one year.

4.6.3 NA62-HI

The system of beam lines that transports the protons from the SPS to the T10 target can be modified in order to achieve a higher flux of protons on target compared to the current one used for NA62. The precise setting and studies on of these beam lines is discussed in Chapter 8. In this new setting, the NA62 experiment is called NA62-HI (or NA62x4). This

experiment could be run for 5 years (at an intensity approximately four times higher than the current one) to collect approximately 400 rare decays ($K^+ \to \pi^+ \nu\bar{\nu}$) reaching a 5% precision measurement of this branching ratio. This experiment leaves almost unchanged
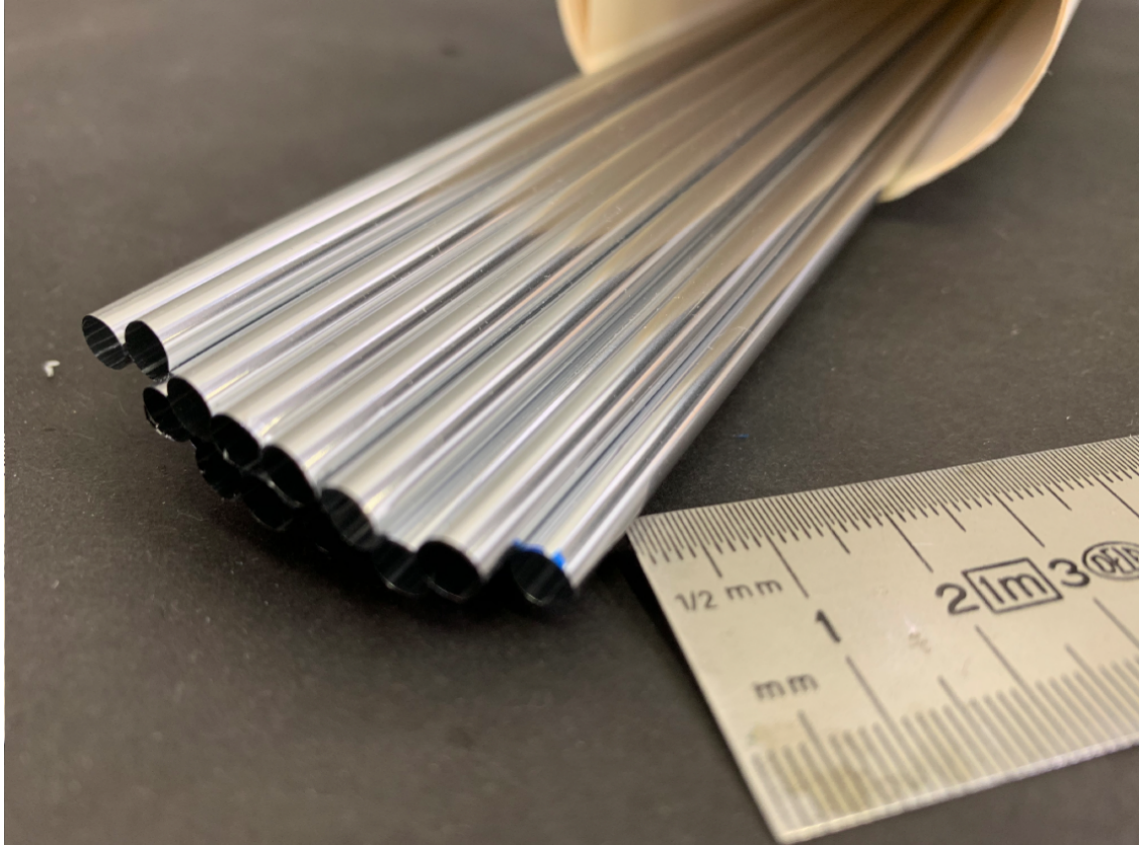
Figure 4.10: Figure of the new straw-tubes developed for NA62 [71].

the current configuration of the NA62 (K12) beam line, with changes to be considered for the target and the TAX. The adaptation of these components in the new configuration has been studied within the SY-STI section at CERN. These studies show that a new target (possibly in carbon) with pressurised air cooling and adding additional cooling in the central region of the TAX allows to reach the desired intensity [71]. The detector of NA62 also requires some changes to run in this configuration, mainly for the GTK tracker, the STRAW tracker, the CEDAR and the electromagnetic calorimeter. This is mainly due to the fact that for the new (higher) rate of events the experiment might be blinded by pile-up (this is the accumulation of two or more events that cannot be distinguished separately by the detector). Initial considerations show that the GTK tracker can be pushed to a resolution $< 50\ ps$ and an efficiency above 99%. The STRAW detector that is composed of thin tubes containing gaseous material is improved reducing the tubes

diameter (4.8 mm compared to the previous 9.8 mm, see Figure 4.10). This leads to a trailing-time resolution of approximately 6 ns (per straw), 1 ns (for track) increasing the rate-capability by a factor 6-8. Finally, from first estimates on the signal selection, it was shown that the CEDAR could use H_2 gas (see studies in Chapter 7) in order to reach a time resolution of approximately 20 ps and that the electromagnetic calorimeter can be redesigned to reach a 10 ns full width half maximum (FWHM) [71]. In addition to these modifications, studies of the radiation shielding and the experimental hall have to be performed in order to confirm the feasibility of this configuration in terms of radiation protection (RP). These studies are currently being developed by the radiation protection RP group at CERN using the model developed in Chapter 8.

4.6.4 SHADOWS

SHADOWS is a very recent project presented to the PBC commitee in 2021. This project, proposes at the installation of an off-axis detector along the K12 beam line. SHADOWS
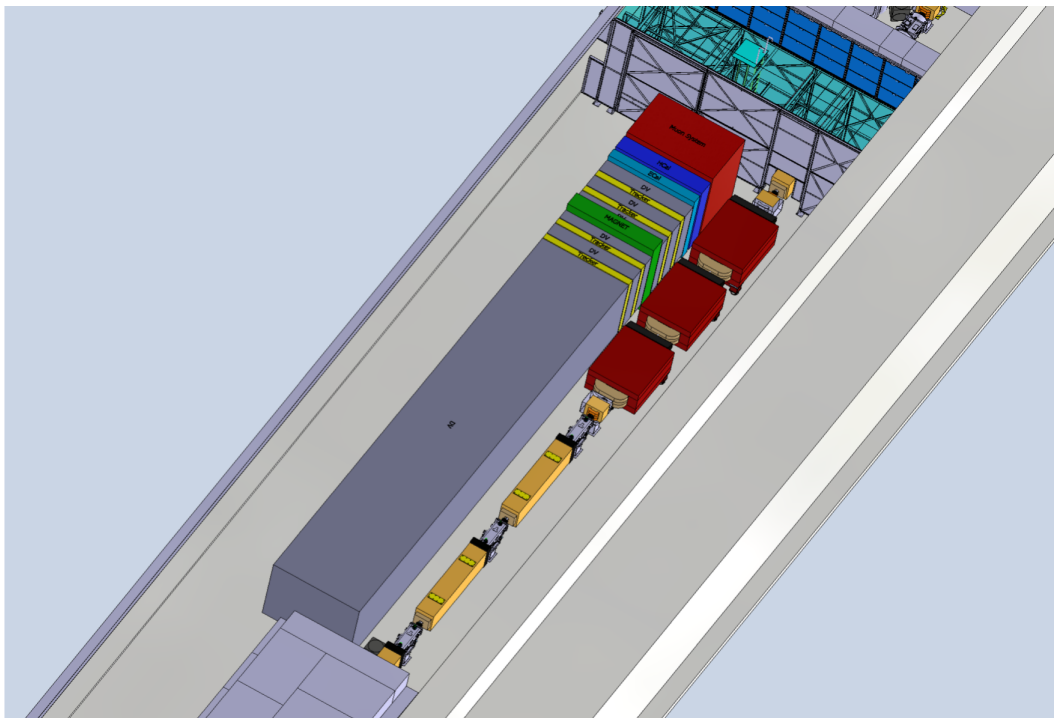
Figure 4.11: Top view of a CAD model with the SHADOWS detector off-axis the K12 beam line. The detector (spectrometer) is the big grey block followed by the yellow, green, blue and red blocks next to the magnets of the beam line [72].

is a parasitic experiment, that could take data while the NA62 experiment runs in beam dump mode. It is able to search for feebly interacting particles, created in the beam dump.

Feebly interacting particles (FIPs) is a term that indicates all the particles whose interaction with Standard Model particles is very weak ($\alpha_f \ll 1$) [72]. The experiment detector is placed about 20 m downstream of the TAX and is a standard spectrometer, composed of a magnet, trackers and calorimeters. Because of that, the dark matter particles and their decay products still have relatively high energies at the SHADOWS detector compared to NA62, which final calorimeters are about 200 m downstream the TAX. This experiment avoids the background generated by particles moving forward on-axis in the beam line but is still affected by the many muons generated in the TAX. Studies of this background have been developed and are reported in Chapter 8. The experiment is proposed to be installed in the experimental hall during LS3 [72].

Simulation Tools

This chapter is dedicated to introducing the software packages used for the simulations in this thesis work. The software is used for secondary beam line optics, background and radiation studies. The codes that were used for these studies in the past (legacy) have been recently replaced within the secondary beam line software migration program. The former are presented for reference in the next section.

5.1   Legacy Software

The four major programs that have been used for studies of secondary beam lines before the migration start in 2017 are:

- BEATCH [73] is a code that is used to generate the coordinates of beam line elements. This is an essential reference for the design, the installation and alignment of components in secondary beams.

- TRANSPORT [74] is a tool for beam optics calculations. It calculates the elements of the transfer matrix up to third order (the version that goes up to second order is used in the EA-LE section) and can be used to perform matching of optics functions.

- TURTLE [75] is a tool used for particle tracking. It includes: total absorption of particles at collimators and at magnet apertures, some particle decay processes and calculates transmission and particle distributions (X, X', Y, Y', $\frac{\Delta p}{p}$). It is a complementary code to TRANSPORT that can also produce TURTLE file inputs.

- HALO [76] is a Monte-Carlo simulation tool for muon tracking. In this code, the

magnets, the associated field maps (applied also to the yoke of magnets) and collimators can be placed using a series of different predefined models. This software can track parent particles and their decay products only.

These codes have been developed in the 70's and 80's in FORTRAN language and have only been used in recent years by the EA-LE section at CERN, becoming increasingly difficult to maintain and adapt to the evolving CERN software infrastructure. New codes such as MADX or BDSIM (see next sections) provide indeed most of their functionalities within one package. For this reason, even if some of the above tools are still maintained at CERN, they are not used in this thesis. More details about the process of software migration program can be found in Ref. [77].

5.2 MADX

Methodological Accelerator Design version 10, MADX, is a software package used in particle accelerators for beam line design and optics studies. The main functionalities of MADX are optics calculations, matching and generation of survey layout. The source code is written in C, C++ and FORTRAN programming languages [78]. MADX provides tracking functionalities similar to the ones of the TURTLE code, where beam-matter interactions are not simulated. MADX integrates a module, the Polymorphic Tracking Code (PTC) [79], that is capable of symplectic particle tracking and thick lens tracking. PTC is particularly used for small and low energy accelerators. MADX provides the possibility to plot the calculated optics functions using the internal plotting routine. Figure 5.1 shows the relevant elements of the matrix R calculated for the P42 beam line plotted with the MADX standard plotting function. The output file of MADX can have different formats and can be customised in order to contain any kind of information (usually R-parameters or Twiss parameters are of interest). These output files (mainly in TFS and TXT formats) are compatible with other software packages used for accelerator physics, such as BDSIM and AppLE.py.

5.3 AppLE.py

Although MADX provides a wide range of functionalities it does not provide an interactive graphical user interface (GUI). Secondary beam lines during operations need to be changed repeatedly in order to find the optimal configuration for the user needs. Therefore a GUI
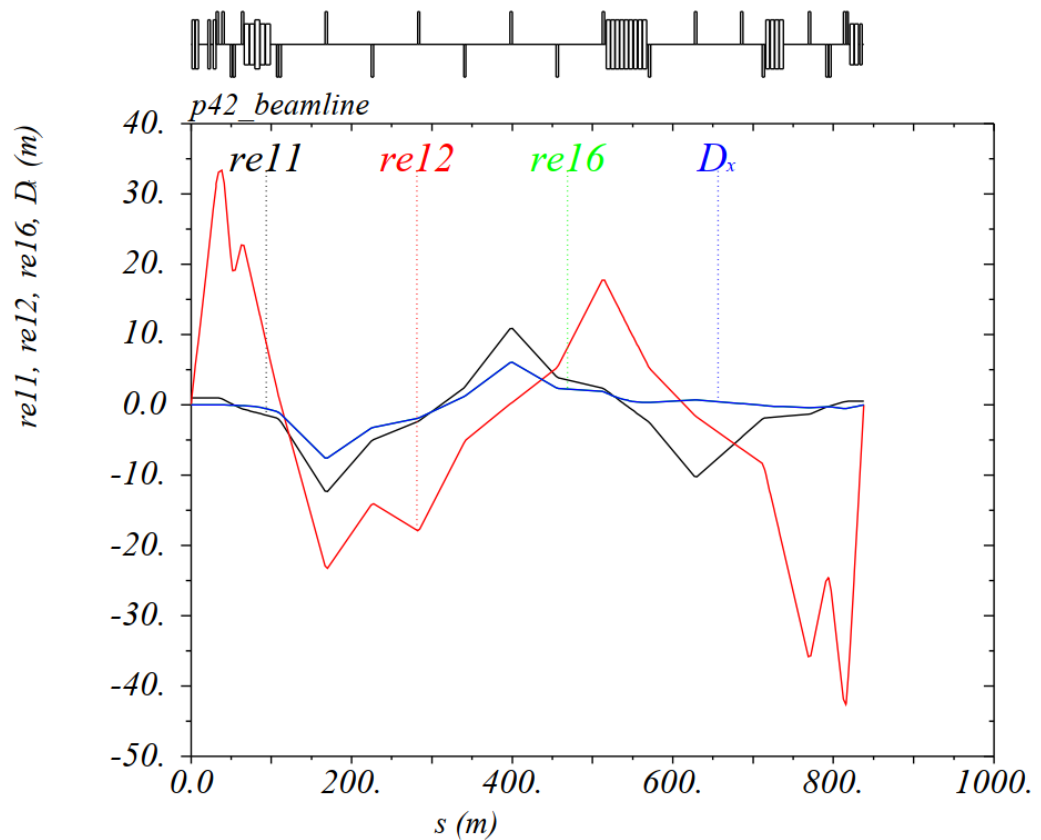
Figure 5.1: Optics functions (R-parameters and Dispersion) calculated and plotted with MADX for the P42 beam line in the North Area. On the top of the figure it can be seen a scheme of the beam line elements.

or a tool to visualise interactively the changes of the optics in function of the lattice was needed. For this reason the PYTHON code APPLE.py has been created in the CERN EA-LE section for secondary beams. AppLE.py can be defined as a GUI for MADX that gives the possibility to customise calculations or to extend the functionalities of the latter [77]. It allows to calculate the optics functions and additionally provides the possibility of matching optics functions directly from the GUI. AppLE.py provides the possibility of producing tracking and optics plots directly from the GUI. The software capabilities are currently being extended with an active contribution of the author of this thesis. Currently, APPLE.py has been extended in order to provide relativistic corrections at low energy, include synchrotron radiation effects and include a high number of classes for every component commonly used in secondary beams.

73
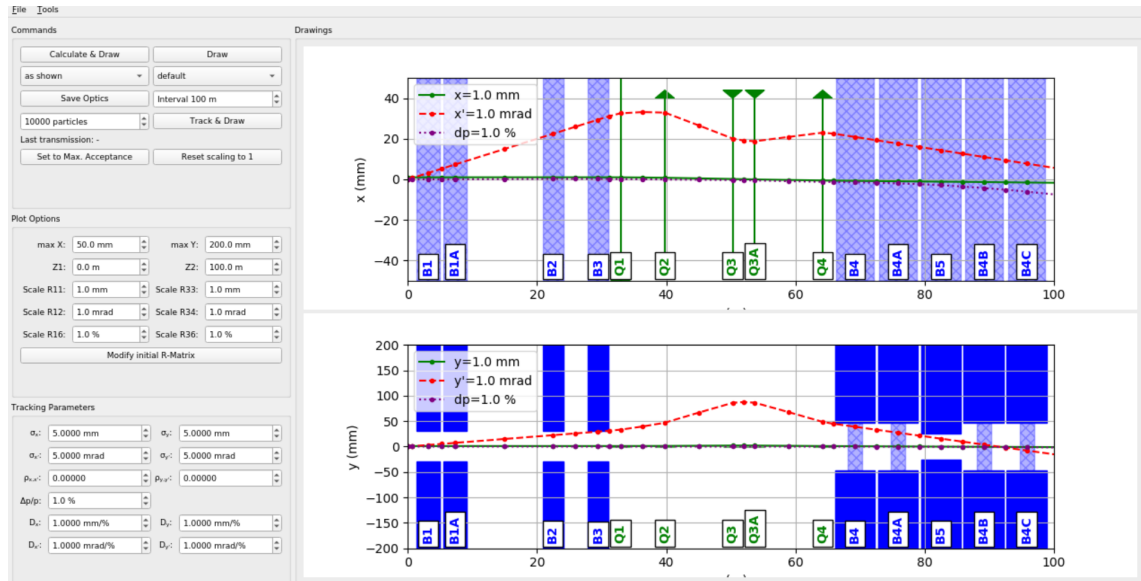
Figure 5.2: APPLE.py Graphical User Interface (GUI). On the left is displayed a panel where the optics parameters can be set, on the right the calculated optics functions are shown.

5.4 FLUKA

FLUKA (FLUktuierende KAskade) [80,81] is a Monte Carlo (MC) simulation software that simulates the interaction and transport of particles in matter. FLUKA has found applications in several fields such as particle physics, astro-particle physics, radiation protection, dosimetry and medical physics. The software is available in the form of a pre-compiled object library and it is developed using FORTRAN. A graphical user interface to run FLUKA named FLAIR [82] has been developed using PYTHON. FLAIR allows the user to design components in the GUI and interactively change their characteristics e.g. dimensions and material. In FLAIR as well as in FLUKA every object has an associated function (called card) and can be implemented via the use of this card. If for example a box needs to be placed in a certain place in space, this can be achieved via a box card, in which the positions of the vertexes of the geometry can be specified. See the definition of three bodies in FLAIR in Figure 5.3. Via these cards it is also possible to choose the kind of quantity that should be registered such as the radiation in a certain region, or the flux of muons in a certain plane. FLUKA uses a set of physics processes that cannot be completely changed; these physics processes can be partially customised via the physics cards, that allow to introduce a certain energy cut-off (can also be a particle type cut-off) or to add/remove a specific interaction. FLUKA provides also the possibility to create

Title:
Black body
SPH blkbody   x: 0.0   y: 0.0   z: 0.0
                      R: 100000.0

Void sphere
SPH void   x: 0.0   y: 0.0   z: 0.0
                      R: 10000.0

Cylindrical target
RCC target   x: 0.0   y: 0.0   z: 0.0
                      Hx: 0.0   Hy: 0.0   Hz: 10.0
                      R: 5.0

Figure 5.3: Three cards implemented in FLAIR. These cards create three objects (two spheres and one cylinder) in the FLUKA geometry.

user routines in order to achieve a specific implementation not already predefined in the software. These routines have to be written and compiled using FORTRAN. These are useful for example in implementing custom magnetic fields (see Figure 5.4) in a certain region, custom scoring of physics quantities and custom beam source. The FLUKA software
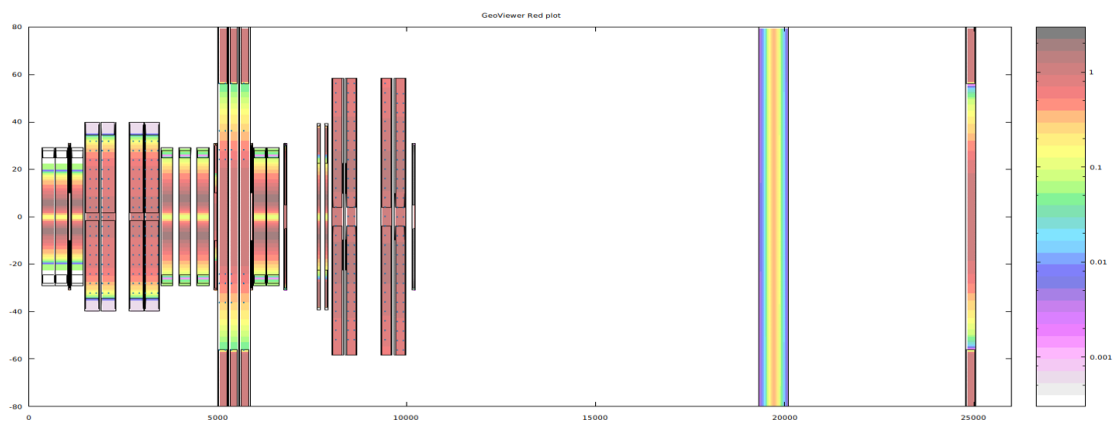
Figure 5.4: K12 beam line designed and visualised in FLAIR. It can be seen that every region has been assigned a magnetic field, via a routine written in FORTRAN. The field scale is in Tesla.

has been used at CERN and worldwide for the past decades and has been benchmarked with a large number of measurements [83]. At CERN it is currently used for all the main experiments including those at the secondary beam lines where FLUKA is used as a reference software for background and radiation studies.

5.5 GEANT4

GEometry ANd Tracking version 4 (GEANT4) is an open-source platform using MC methods for simulations of particle propagation through matter [84]. The functionalities of this software are similar to the ones of FLUKA even if the internal structure of this software is quite different. GEANT4 is written in C++ and provides a graphical GUI that is not completely interactive (the geometry and events can be visualised but not modified in the GUI). Most of the functionalities of GEANT4 are ordered into classes that provide pre-constructed modules for geometry, events, processes and so on. Predefined classes make the interaction with the software simple and flexible. Classes can indeed be created or modified ad-hoc for specific applications. Geometries in GEANT4 can be built using the standard classes or imported from other formats, such as GDML [85]. GDML is the native import and export format for geometries in GEANT4 and is capable of describing the full set of solids and other features as well as meshed solids, see Figure 5.5. Geometries written in GDML have a structure proper of the Extensible Markup Language (XML) that is a markup language that defines a set of rules for encoding documents in a file using a format that is both human and machine readable. The description of the
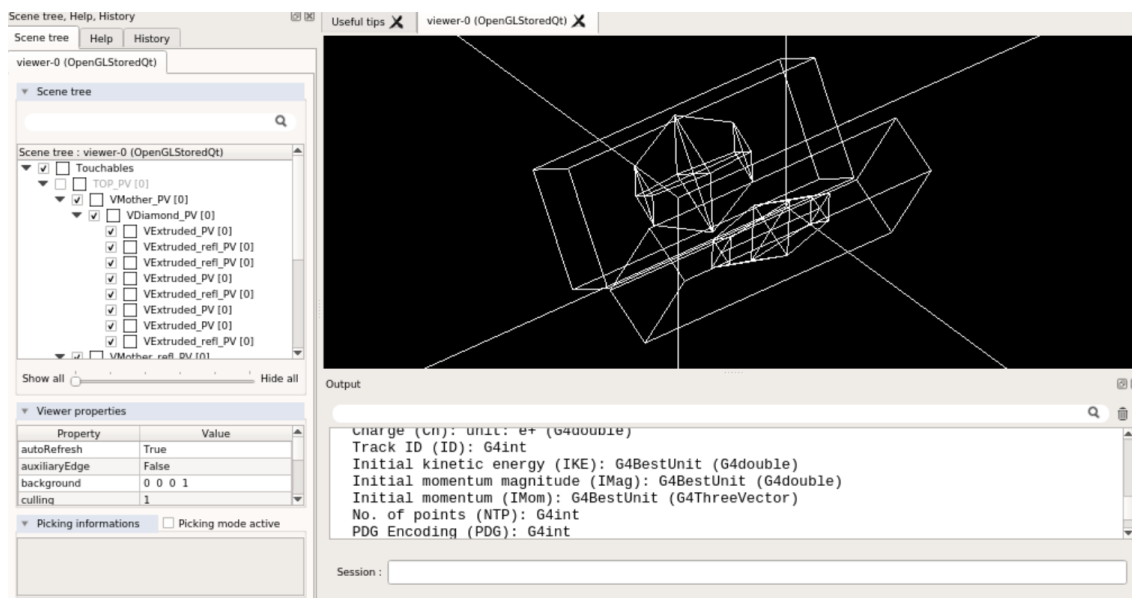
Figure 5.5: GDML geometry displayed via the GEANT4 visualizer.

physics processes in GEANT4 is fully customisable: the user can decide which processes to include (e.g. electromagnetic interactions, hadronic interactions and so on). If no process is specified, GEANT4 simply propagates particles without simulating any interactions.

The software also provides a series of physics lists, that are packages containing a list of physics processes. The choice of the physics lists depends on the experiment type and is up to the user to find which ones are better suited for the specific case. GEANT4 is a software widely used in the scientific community and at CERN. Over the years many codes that make use of a GEANT4 core have been written, these codes make the interface with GEANT easier, among those BDSIM, that is described in next section.

5.6 BDSIM

Beam Delivery SIMulation (BDSIM) [86] is a MC software that simulates the passage of particles through a beam line or material. The simulation of the physics processes is based on GEANT4 that is at the core of BDSIM. This software is written in C++ and also makes
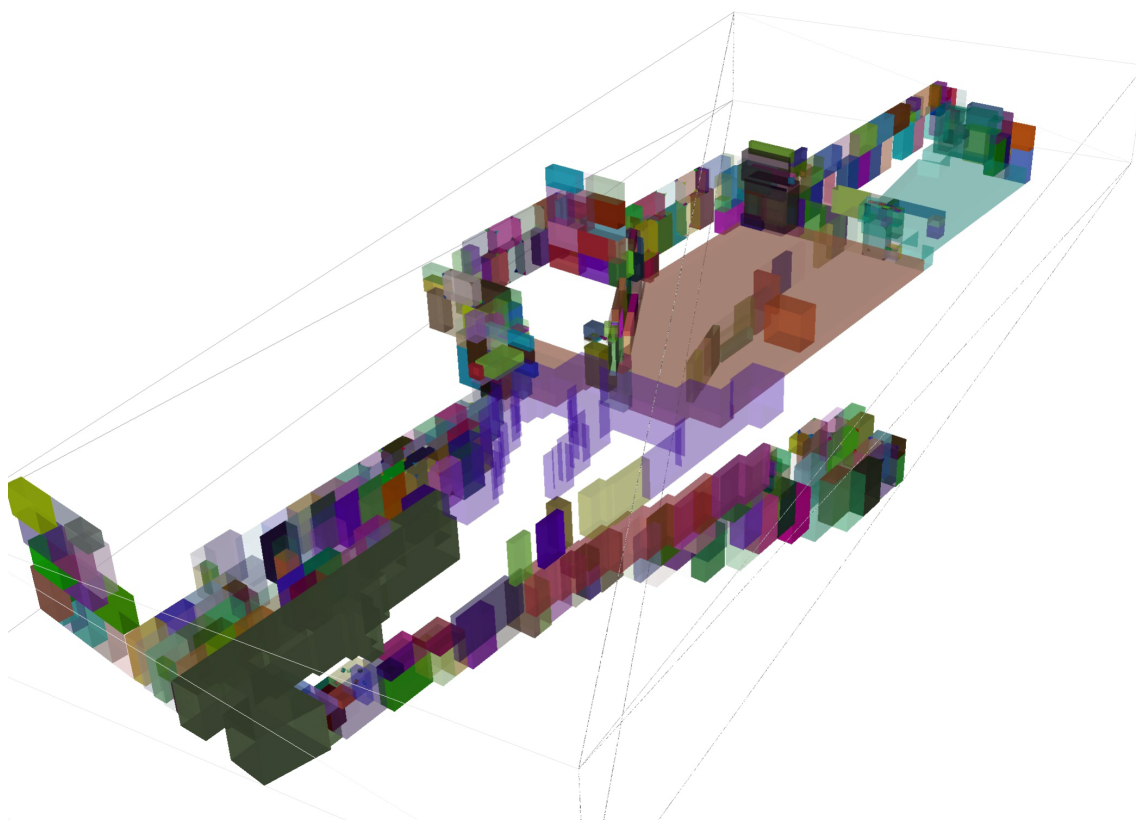
Figure 5.6: East-Area Shielding converted to GDML from CAD using PYG4OMETRY. Each part is given a randomly assigned colour to clearly indicate the structure of the shielding.

use of other packages such as CLHEP [87] and ROOT [88]. A few PYTHON tools have been written in order to extend the capabilities and functionalities of BDSIM: PYMADX,

PYBDSIM and PYG4OMETRY [89] [90]. PYMADX is a tool that is useful to load a
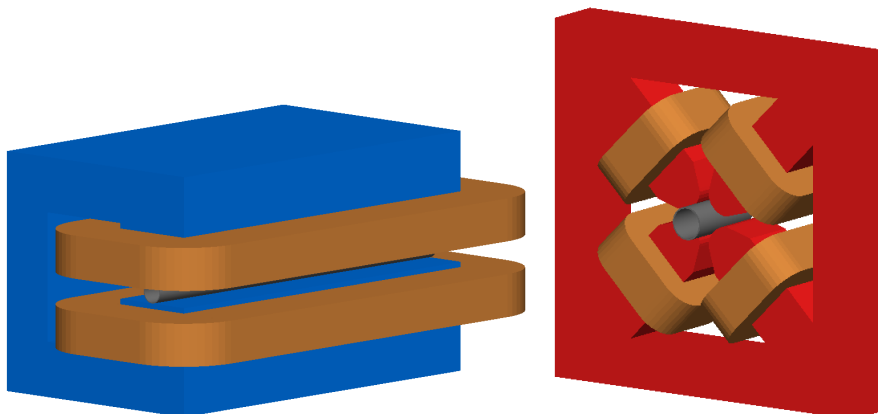
Figure 5.7: Bending and quadrupole magnets defined using the standard class of BDSIM visualized in the software GUI.

MADX output as well as to prepare MADX (or PTC) models giving the possibility to convert it to BDSIM. PYBDSIM is a PYTHON tool that make the preparation, running and validation of BDSIM models easier and faster. Finally PYG4OMETRY is a tool used to easily create and convert geometries from different types of formats. See a converted geometry from CAD to GDML visualised in BDSIM in Figure 5.6. Geometries in BDSIM can be defined using the internal classes, see Figure 5.7. Each element of the internal classes contains a series of parameters that allow to customise these components. In alternative to these standard classes BDSIM can also import geometries from a series of formats e.g. GDML (see Figure 5.8), MOKKA [91] and GGMAD. The input file format of BDSIM,
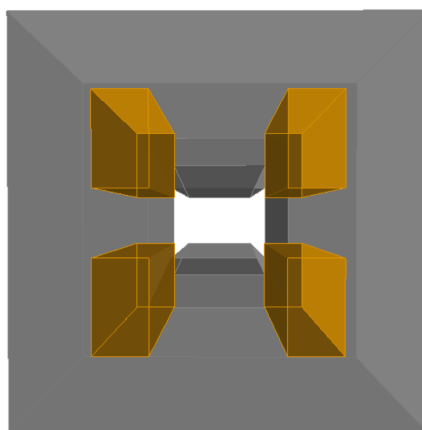
Figure 5.8: MDX magnet imported in BDSIM from a GDML file. The magnet is visualised in the BDSIM GUI.

GMAD, is very similar to the MAD-X one, but in contrast to this it is implemented in terms of a grammar and parser generator that limits eventual errors. Field maps in BDSIM

are expressed in the Frenet-Serret coordinate system, contrary to the GEANT4 coordinate system that is expressed in 3D Cartesian coordinates. Coordinate transformations between Cartesian and Frenet-Serret are used throughout BDSIM and allow to use Frenet-Serret coordinates in GEANT4. The output of BDSIM is in a ROOT file format and contains by default all the information at a plane (transverse to the beam direction) at the end of each element of the beam line. It is possible to limit or extend what information is stored at a plane through a series of functions implemented in the software. BDSIM is a new software with a growing community within the accelerator physics environment. It proved to be highly useful for secondary beam lines since it gives the possibility to do both optics and beam-matter interaction studies.

Chapter **6**

Collimation in Secondary Beams

This chapter focuses on collimator studies in the energy range of the CERN North Area secondary beam lines. It is highly important to have a well collimated beam, especially for high-precision experiments like those downstream of the K12 beam line. The studies carried out in this chapter quantify the so called "skin depth", an important factor for precise collimation, which is defined and discussed in detail in the next sections. The skin depth is studied for charged and neutral beams using different collimator materials and at different momenta.

6.1   Secondary Beam Lines Collimation

Primary protons impinging on a primary target produce secondary particles, while a fraction escapes from the target without interaction. The majority of the particles emerging from the target are not useful for the experiments and they could become a source of background. For this reason they must be stopped as soon as possible, while the rest are transported through the downstream beam lines. In NA62, for example, up to more than 10^{12} primary $400\,\mathrm{GeV/c}$ protons impinge on the primary target per extraction. On average only a few 10^8 or less are finally selected. Therefore, essentially all the energy contained in the beam is deposited on the primary TAX collimator placed directly after the target. Materials used for collimators in secondary beam lines vary according to applications. For example, tungsten has a nuclear interaction length of $10\,\mathrm{cm}$ and therefore has a high stopping power. This combined with its thermodynamical properties, like a high melting point, makes it a suitable material for the collimator jaws along the apertures. The bulk materials are usually steel or copper. Materials commonly used in secondary beams are

listed in Table 6.1 below. Some general design considerations for the collimation systems of charged and neutral beam lines are presented in the following sections, along with some examples from the CERN North Area [39].

Material	λ_I (cm)	X_0 (cm)	ρ (g/cm^3)	$\frac{dE}{dx}$ (MeV/cm)
Be	42.1	35.2	1.8	2.9
Al	39.7	8.9	2.7	5.4
Fe	18.3	1.9	7.2	11.4
Cu	15.3	1.4	8.9	12.6
Pb	17.6	0.6	11.4	12.7
W	10.7	0.4	18.0	22.1

Table 6.1: Materials commonly used for collimation in CERN secondary beam lines with their respective values of nuclear interaction length, radiation length, density and stopping power [13]. The iron and tungsten used in this chapter, however, are alloys with a small percentage of light materials and the values vary dependent on the exact material composition.

6.1.1 Charged Beam Collimation

A charged beam interacting with a collimator can generate a number of secondary particles. Most of these secondary particles escape from the collimator at low energy and can cause significant background for the experiments if not absorbed properly. Some of the interactions in the collimator produce also neutral hadrons and photons which are harder to suppress (neutral particle collimation will be discussed in the next section). In order to deal with the lower-energy charged particles, the collimators are usually followed by a number of additional cleaning collimators as well as magnets such as dipoles, quadrupoles or sweepers (see Chapter 3). These magnets, if tuned to transport the nominal beam momentum, will sweep the lower energy charged debris away from the downstream experiment. However, high energy muons may be produced and their sweeping requires a long lever arm. Therefore, in general it is important to implement strong collimation as far upstream as possible in secondary beam lines. Collimators for secondary beams at CERN are typically about 1 m long, much shorter than typical focal distances in charged beam lines at high energies. Therefore, collimator jaws are normally flat blocks. However, if a collimator has a very small aperture and if it is located in a very sharp focus, it might use tapered jaws. This is the case for example for Collimator 3 in the K12 beam line used for the NA62 experiment [1], which has a nominal aperture of ± 1.2 mm with tapered copper jaws before and after a flat section, as shown in Figure 6.1.
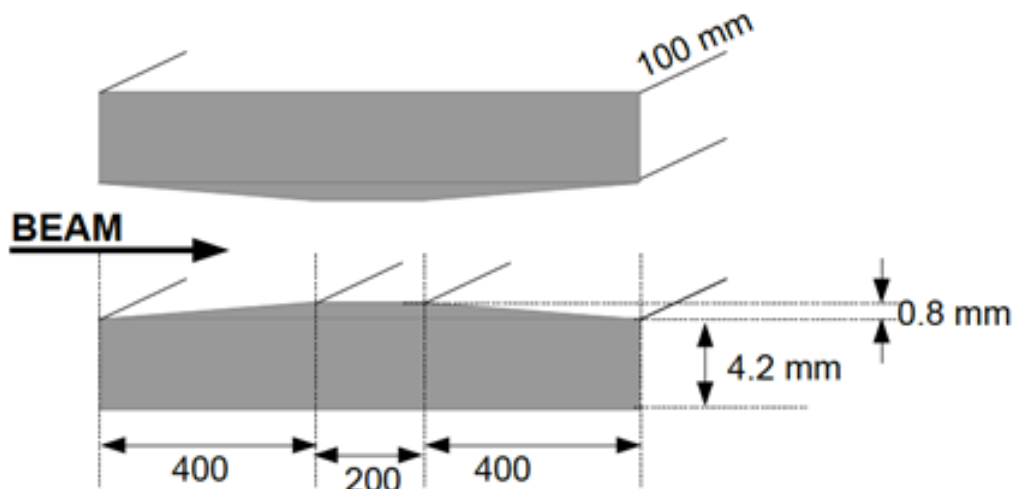
Figure 6.1: Profile of the jaws of Collimator 3 of the K12 beam line with copper shim plates

6.1.2 Neutral Beam Collimation

Similarly to charged beams, in neutral beam lines all collimators have to be followed by magnets (e.g. sweeping dipoles), since the interactions of neutral particles with the material will generate charged components. The main advantage in neutral beam is that, in general, the magnets responsible for sweeping the charged particles can be as strong as reasonably achievable (since they do not influence the neutral beam), while ensuring that they have a comfortably larger aperture than the neutral beam envelope. Once again, the sweeping should start as early as possible, especially for pions and kaons, which decaying into muons could generate background in the downstream experiment setup. However, in general neutral beam collimation is more delicate than charged beam collimation. Mitigation is only achievable by means of multiple collimation stages, each in turn affected by the skin depth of the collimators used. The skin depth will be discussed in more detail in next section, at the moment it can be understood as an additional thin layer of the aperture of the collimator that entering particles can escape from It can be shown an example of a cleaning collimator in neutral beam lines, such as the KLEVER one. In this example a charged beam collides on target producing a neutral secondary beam, see Figure 6.2. The angular acceptance cone is defined by the first collimator of inner radius R_1 and skin depth δ , located at distance L_1 from the centre of the target. The acceptance angle is thus $\pm\theta = \pm(R_1 + \delta)/L_1$. The overall beam length L is defined either by the length of the beam line or by physics constraints (e.g. the decay length of the particle of interest).

To mitigate scattering products from the first (defining) collimator causing backgrounds and beam tails in the experiment, a cleaning collimator is placed after it, at distance L_2 from the defining collimator and with inner radius R_2, with L the distance between the target and the cleaning collimator, $L = L_1 + L_2$. Such a layout is schematically shown in Figure 6.2. It can be calculated, see Ref. [39], that the best collimation is reached for a
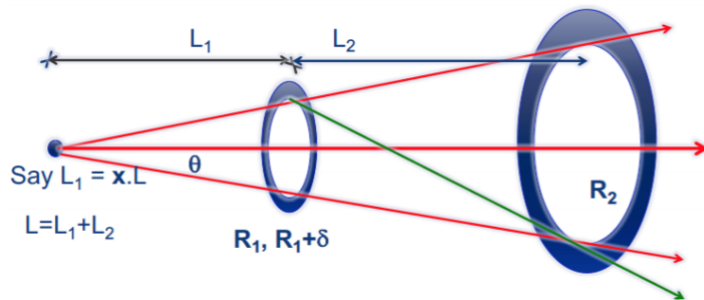
Figure 6.2: Target followed by a defining collimator of radius R_1 placed at a distance L_1 from the target and a cleaning collimator of radius R_2 and at distance L_2 from the defining collimator [39].

position of the defining collimator at $x = L_1/L = 1/3$.

6.1.3 Skin Depth

In previous sections the various methods used in order to reduce the flux of lower energy particles generated from the interaction with the collimator were discussed. In addition to this component there is a part of the beam that interacts at the collimator edge and loses only a small amount of energy without undergoing an inelastic collision. These particles can be accepted within the envelope depending on the momentum acceptance of the beam line. This effect is quantified by the impact parameter also called in this thesis "skin depth" [44]. The skin depth is the mean thickness of the layer at the collimator edge at which the beam impacts, loses a small amount of energy and then scatters back into the collimator aperture and is accepted within the main beam causing an additional source of background for the experiment. A way to quantify the skin depth is to consider the distribution of the initial impact position of such particles that manage to emerge from the collimator edge and are accepted within the beam. This distribution follows an exponential function, $\alpha e^{-\alpha x}$, where α is the decay parameter. The skin depth can be calculated from this distribution with a cut at 90% of the population as [39]:

$$\delta = \frac{\ln(10)}{\alpha} = \frac{2.3}{\alpha} \qquad (6.1)$$

It can be seen from this definition that for a given skin depth of value δ and a collimator with aperture of size R_1, the effective aperture of the collimator, considering skin depth corrections, will be $R_1 + \delta$, as was considered in the previous section, for the neutral beam collimation example. It is important to take this factor into account to mitigate scattering products from the collimators creating backgrounds and tails for the experiment (especially for high-precision experiments, such as NA62). The impact of the alignment of the collimators on the "skin depth" calculation was not taken into account for these studies which aims to give a first estimation of this parameter for the secondary beam lines at CERN. The skin depth is studied for different materials, incident momenta and acceptance, using GEANT4 and FLUKA. The details and results obtained are presented in the following sections.

6.2 Skin Depth Estimations for Charged and Neutral Beam

The FLUKA and GEANT4 collimator models are based on a simple block that represents a single collimator jaw for the geometry description. The block is $80\,\mathrm{cm}$ wide in X and Y and has a length of $1\,m$ in Z. It is located in the planes $0\,\mathrm{cm}{\leq}X{\leq}80\,\mathrm{cm}$, $-40\,\mathrm{cm}{\leq}Y{\leq}40\,\mathrm{cm}$ and $-50\,\mathrm{cm}{\leq}Z{\leq}50\,\mathrm{cm}$. The incident beam has been chosen with a spatial spread of 0–$8\,\mathrm{mm}$ in X with zero spread in Y which is sufficient to estimate the skin depth values of a few hundred microns corresponding to one plane (X). The angular spread used is $\sigma_{X_0'} = 5\,\mathrm{mrad}$ and $\sigma_{Y_0'} = 0\,\mathrm{mrad}$ to include the maximum angular acceptance of most CERN secondary beam lines. The model can be seen in Figure 6.3 in the GEANT4 visualiser for a sample run of five incident π^+ particles following the above distribution and interacting in the collimator jaw. The particles tracks are identified by colour as shown in the table in the figure. The skin depth is calculated for different incident momenta, p_0, where the chosen values are representative of the CERN North Area. The number of events simulated in both GEANT4 and FLUKA is 10^6. The GEANT4 simulations use the version GEANT4.10.06 and the $FTFP\_BERT$ physics list. The $FTFP\_BERT$ is a complete physics list in GEANT4, it is so called because it uses the Fritiof string model and the Bertini cascade model. The Fritiof (FTF) model transmits particles exchange assuming that one or two unstable objects - quark-gluon QCD-strings, are produced in elementary interactions. It propagates the interactions supposing that these strings can interact with other nucleons in hadron-nucleus and nucleus-nucleus collisions [92]. The Bertini (BERT) model is used
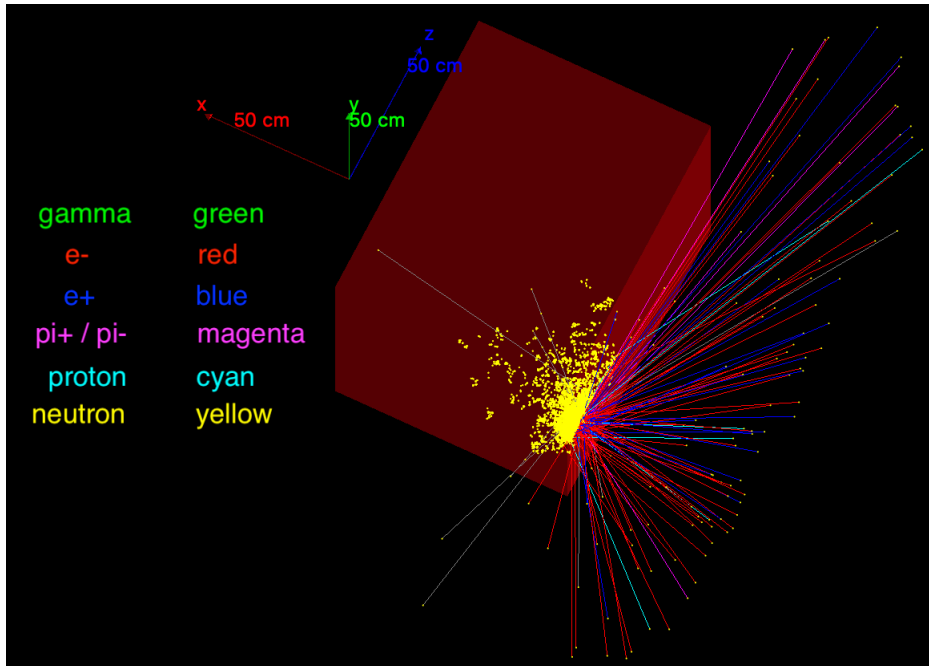
Figure 6.3: Visualization from the GEANT4 model for the collimation studies showing five incident π^+ particles interacting in the collimator jaw. The particles in the shower are identified by colour as described in the table inserted in the figure.

for parametrisation of the intranuclear cascade of hadrons and nucleons produced through a series of interactions within the nucleus [93]. The FLUKA version used is 4-0.1 with FLAIR 3.1-2 with a DEFAULTS card set to PRECISIO, without further cuts and using the standard FLUKA physics. The standard FLUKA physics list distinguishes among three main hadronic interaction types: hadron-nuclear inelastic interaction, elastic scattering and nucleus-nucleus interaction. Quasi-elastic processes are a minor share of processes and are not discussed here; for more detail on these see [94]. The hadron-nuclear interaction type uses a package that includes a very detailed Generalised Intra-Nuclear Cascade and a pre-equilibrium stage [95] at momenta below 3-5 GeV/c, while at high energies it exploits the Gribov-Glauber multiple collision mechanism [96]. For elastic scattering FLUKA uses a series of parameterized and tabulated interactions. Finally for nucleon-nucleon interaction above 5 GeV per nucleon uses DPMJET-II or DPMJET-III [97], between 0.1 and 5 GeV the modified Relativistic Quantum Molecular Dynamics [98] and below 0.1 GeV the Boltzmann Master Equation [99]. The results from the different runs in the two simulation codes are summarised below.

6.3 Charged Beams

The first studies were done for charged beam lines. A π^+ beam was simulated following the distribution shown in the previous section. These results are anyway valid for other charged particles such as protons and kaons since the difference in mass among these particles is very small compared to the energy of the beam used here (above 20 GeV/c). For the skin depth quantification only the charged particles that leave the collimator block before the end of the 1 m and reach the $X < 0$ region are scored. The distribution of these particles for a 100 GeV/c π^+ beam incident on a 1 m tungsten block in the X' vs momentum space are shown in Figure 6.4 for GEANT4 and FLUKA.
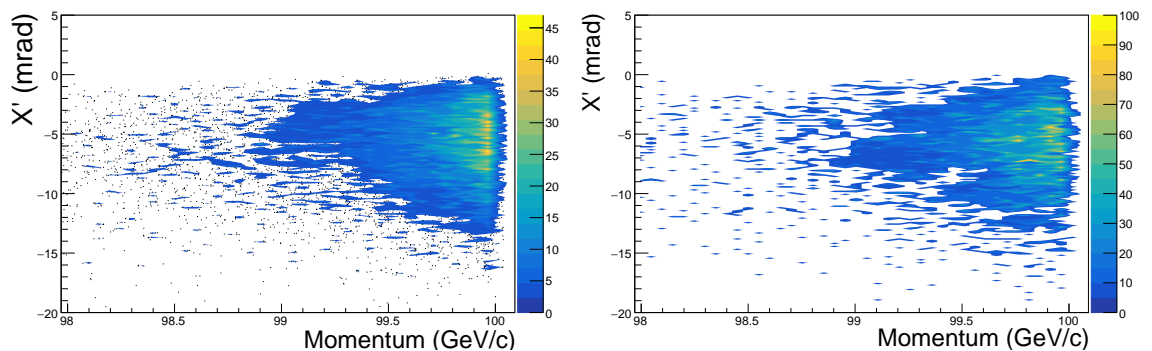
Figure 6.4: Distribution of the angle (mrad) vs momentum (GeV/c) for the charged particles that interact at the edge of the 1 m long tungsten collimator and that are accepted within the aperture limits. The simulated beam is a 100 GeV/c π^+ in GEANT4 (left) and FLUKA (right).

The outgoing beam has a low energy tail which can potentially create background for the downstream experiments. The distribution of the initial impact point of the primary π^+ beam on the collimator for the events with such outgoing particles is shown in Fig. 6.5. The distributions from the two software packages are in very good agreement. However, in the experiments, not all the particles that interact with the collimator material are afterwards accepted within the aperture and transported through the beam line. Indeed, usually, the downstream magnets (e.g. bending ones) sweep away the lower energy tails. Therefore, a reasonable cut on the momentum of $\Delta p/p < 2$ % and divergence within 2 mrad was set on the outgoing particles to estimate the skin depth of the materials for the different momenta. The skin depth was then estimated from the decay constant α of the exponential distribution as shown in Fig 6.5, after applying the acceptance cuts, as Eq. 6.1. Fig 6.6 shows the skin depth as a function of the incident momenta for a tungsten collimator. As seen the skin depth is directly correlated with the incident momenta for the
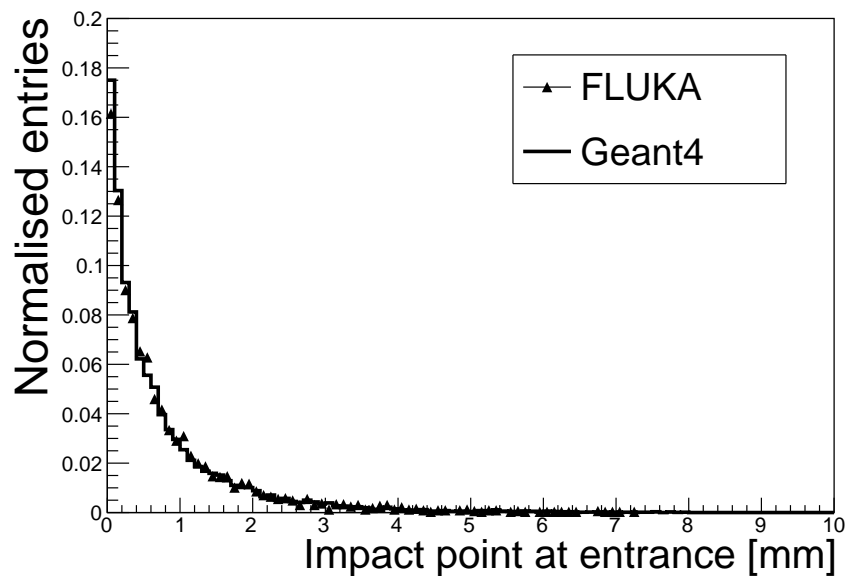
Figure 6.5: The distribution of the impact point of the 100 GeV/c π^+ particle for events where a charged particle scatters off the collimator material and is accepted within the aperture limits for a 1 m long tungsten collimator from GEANT4 and FLUKA.

lower momentum values but the effect reduces and the skin depth plateaus for momenta greater than about 100 GeV/c.
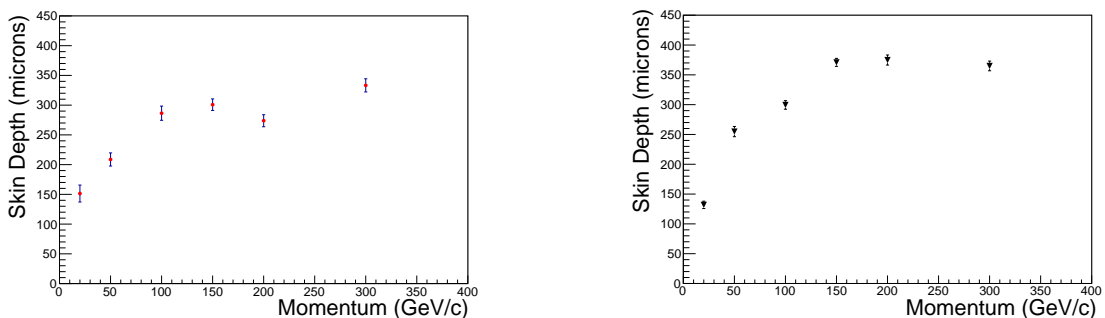
Figure 6.6: Skin depth calculated for different momenta using a cut of $\Delta p/p < 2\%$ and an angular cut of 2 mrad in X' and Y' from GEANT4 (left) and FLUKA (right).

The skin depth values are also calculated for different materials using a 100 GeV/c π^+ beam and the aforementioned cuts. These results are summarised in Table 6.2.

It can be seen that in this case the skin depth is strongly correlated with the nuclear interaction length of the material as expected, with the values being larger for larger nuclear interaction lengths. This is due to the fact that strong interactions, such as the ones involved in the skin depth effect are correlated with the nuclear interaction length.

Material	$GEANT4\ (\mu m)$	$FLUKA\ (\mu m)$
Be	1106 ± 16	1092 ± 16
Al	1005 ± 15	964 ± 17
Fe	598 ± 16	616 ± 16
Cu	575 ± 14	508 ± 14
Pb	577 ± 15	556 ± 16
W	278 ± 11	306 ± 10

Table 6.2: Skin depth for a 100 GeV/c π^+ beam interacting with collimators of different material simulated in FLUKA and GEANT4

6.4 Neutral Beams

For the neutral beam simulations, a $100\,\text{GeV/c}$ K_L beam was chosen with the same distribution and geometry as for the charged beam. The choice was mainly driven by the fact that this particle type is the one used in the KLEVER experiment and has different properties than other neutral particles; see Chapter 3 for the properties of the K_L. The charged interaction products were ignored for the studies, as they are assumed to be removed by magnetic sweeping [67]. Figure 6.7 shows the distribution of angle versus momentum of the neutral particles leaving a 1 m tungsten collimator in the $X < 0$ region, for GEANT4 and FLUKA.
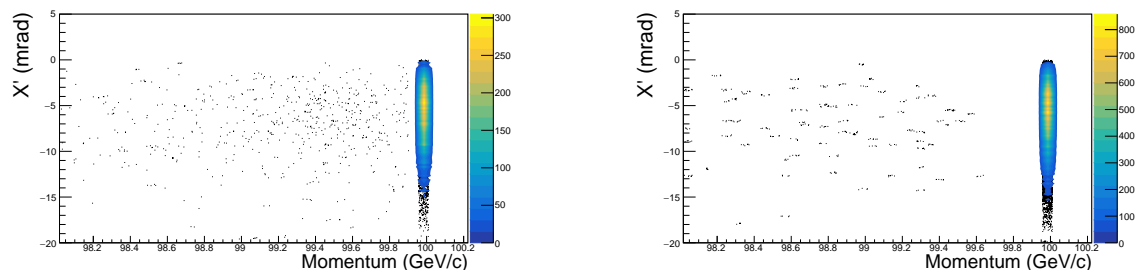
Figure 6.7: Distribution showing the angle (mrad) vs momentum (GeV/c) for the neutral particles that interact at the edge of the collimator for a 1 m long Tungsten block and are accepted within the aperture limits for a $100\,\text{GeV/c}$ incident K_L beam from GEANT4 (left) and FLUKA (right).

Since in a real beam line the neutral particles cannot be swept away by the magnets, a momentum cut is not applied in this case. Only an angular cut was used to estimate the skin depth for different materials. Figure 6.8 shows the distribution of the impact point for the events with incident beam accepted within the aperture limits of the collimators after interaction. The distribution is shown for two different momenta (50 and 150 GeV/c) and angular cuts (1 mrad and 2 mrad). Both software packages show that the dependence

of the distribution is stronger on the angular cut than on the incident momentum. The
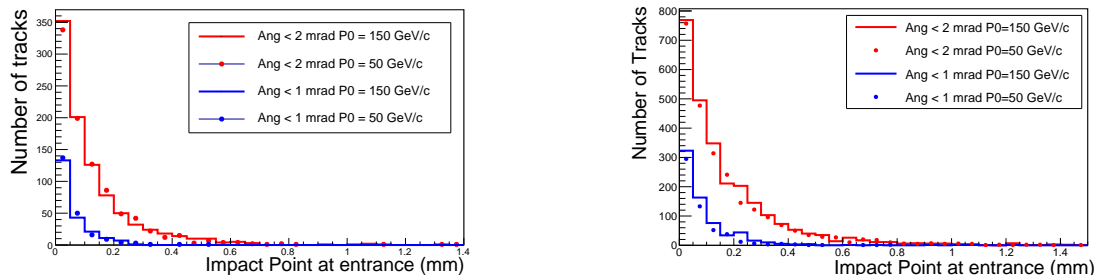
Figure 6.8: Distribution of impact point for $50\,\text{GeV/c}$ and $150\,\text{GeV/c}$ incident momenta K_L beam, for events where scattered neutral particles are accepted within the aperture limits for two angular cuts of $1\,\text{mrad}$ and $2\,\text{mrad}$ from GEANT4 (left) and FLUKA (right)

skin depth value was afterwards calculated as a function of the incident momenta for an angular cut of $1\,\text{mrad}$. The results of this analysis are shown in Figure 6.9, which also does not show strong dependence on the incident momenta for the range of values studied. These studies were repeated for different materials. Table 7.7 shows the values for some
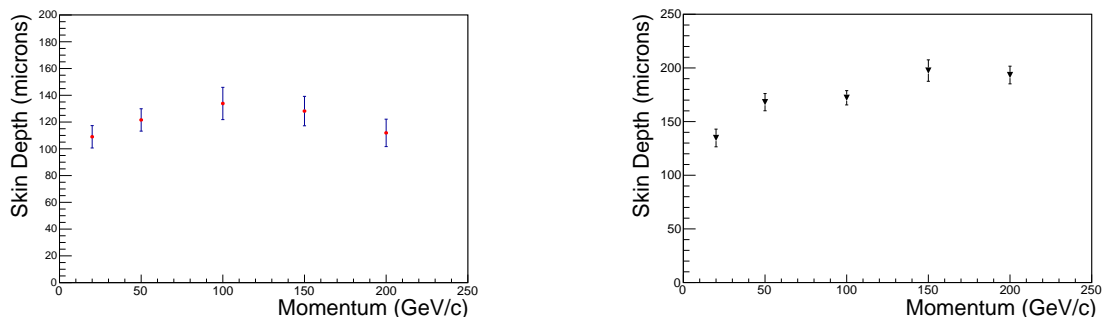
Figure 6.9: Skin Depth for K_L beam incident on a $1\,\text{m}$ long tungsten block at various momenta for an angular cut of $1\,\text{mrad}$ from GEANT4 (left) and FLUKA (right)

commonly used materials for a $100\,\text{GeV/c}$ incident K_L beam and an angular cut of $1\,\text{mrad}$ for the accepted particles.

Material	$GEANT4\ (\mu m)$	$FLUKA\ (\mu m)$
Be	565 ± 19	565 ± 18
Al	575 ± 20	550 ± 21
Fe	331 ± 22	351 ± 21
Cu	248 ± 19	287 ± 17
Pb	225 ± 18	310 ± 16
W	138 ± 12	180 ± 10

Table 6.3: Skin depth for $100\,\text{GeV/c}$ K_L beam for different materials calculated in GEANT4 and FLUKA

6.5 Applications of Skin Depth Studies

Intial studies on the properties of skin depth were carried out for the collimation system of the NA48 experiment [22], a predecessor of NA62. These studies were used for the design and development of the experiment beam line that used a K_L beam and a collimation system composed of momentum defining, acceptance and cleaning collimators. The positions of each collimation component was calculated precisely using the skin depth definition as shown in previous sections. Another future possible experiment using a K_L beam is currently being considered for the Physics Beyond Colliders (PBC) program at CERN [3], this experiment is KLEVER [67], see more details in Chapter 4 and 8. KLEVER aims to use a K_L beam, as NA31 and NA48 did in the past. For this experiment the characterisation of the skin depth to design the collimation system is once again fundamental for a successful run. In particular, to select the material that would best suit the collimation needs of the experiment knowing the value of the skin depth parameter is crucial.

6.6 Results Summary

This chapter summarises the effect of the interactions of secondary beam particles in collimators and quantifies the impact parameter "skin depth" for different incident momenta and materials. The detailed simulation studies have been performed for charged and neutral beams to estimate this parameter with the goal to provide a useful tool for secondary beams design. The skin depth is of particular importance and needs to be taken into account in the design of defining and cleaning collimators. Using this parameter helps to mitigate the background from the scattering products for the downstream experiments. It has been shown that the skin depth is directly correlated with the nuclear interaction length of the material for both neutral and charged particles. Moreover it does not depend strongly on the initial beam momentum (for the range considered, between 20 and 300 GeV/c) but varies considerably with the beam line acceptance, e.g., the momentum and angular cuts. Although some studies on this impact parameter and beam collimation have already been done in the past, e.g., for NA31 as well as in the context of colliders [100], no exhaustive studies have been developed before for secondary beam lines with a precise definition of skin depth. Simulations presented in this section show a good agreement between GEANT4 and FLUKA providing a useful input for future design of collimators in the CERN East and North Area and can be extended to other beams that use a similar

energy range. Further investigations on the effects of collimator misalignment on the skin depth values are being carried out and will be presented in future.

Studies of K12 in the NA62 configuration

A general overview of the NA62 experiment was given in Chapter 4. The present chapter discusses in detail the K12 beam line and the 3-D Monte-Carlo (MC) simulation models created for its better understanding. These models are developed in FLUKA and BDSIM and are mainly used to study the beam and the background in the NA62 experiment. Preliminary studies of the optics are presented in the beginning of the chapter where a MADX model is described and compared to BDSIM.

7.1 Proton transport to K12

The NA62 experiment makes use of 400 GeV/c protons colliding on target for studies on rare kaon decays, see Chapter 4 for more details. These protons are slowly extracted from the SPS thanks to a system of strategically positioned quadrupoles and electro-magnetic septa [102]. The recent maximum extracted proton flux to the whole North Area is about 3.5×10^{13} ppp (protons per pulse), but the aim is to reach 4×10^{13} ppp in the future. From the SPS, protons are first transported to the TT20 and TT24 beam lines before reaching the P42 beam lines and finally K12 [103]. A schematic view of the SPS beam lines in the North Area can be seen in Figure 7.1. It can be seen that between the TT24 and the P42 beam line there is the so called T4 wobbling station. This contains the T4 target that generates the beams for the H6, H8 and P42 beam line. H6 and H8 provide hadron and electron beams, that can also generate low or medium intensity muon beams and are mostly used for test beam activities. Normally the protons impinging on the T4 target are directed towards the P42 beam line and the secondaries produced in the target provide secondary or tertiary beams in H8 and H6. Also in Figure 7.1, it can be seen the T6 target
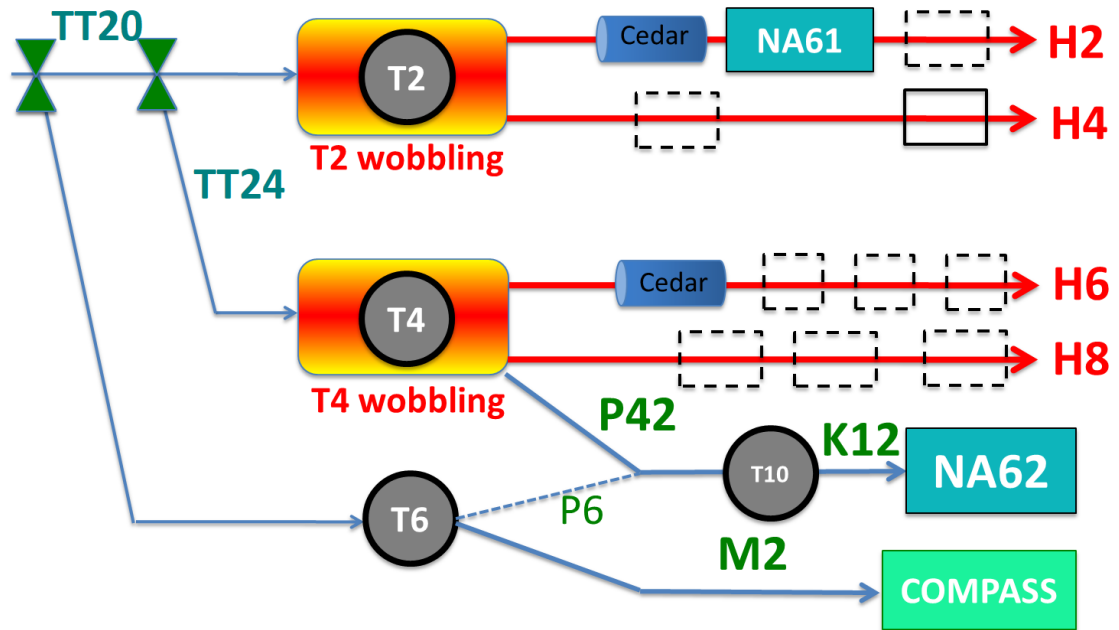
Figure 7.1: Scheme (not to scale) of the beam line structure in the North Area [101]. The T4 target is followed by the P42, H6 and H8 beam lines. The P42 beam line drives protons onto the T10 target where they interact and generate kaons which are selected in K12 before reaching the experiment detector. The other beam lines are used for test beam purposes or serve the experiments highlighted in the picture. Cedar is a gaseous detector mainly used in the North Area for particle identification.

that produces the M2 beam for the COMPASS [61] experiment in the EHN2 hall and the T2 wobbling chamber provides the beam to H2 and H4 that are, among others, used by the NA64 and NA61 experiments, respectively.

7.2 The K12 beam line

The TT20, TT24 and P42 beam lines are beam lines composed mainly of quadrupoles and dipoles. Protons entering the P42 beam line, that is approximately 900 meters long, are afterwards led to collision on the so called T10 target. The centre of the T10 beryllium target (2 mm in diameter and 40 cm long) is defined as the start of the K12 beam line. The T10 target is contained inside massive iron shielding and is followed by two fixed collimators. The beam passing through these two collimators is focused by the first series of quadrupoles through the first "achromat" that is a double-dogleg of four bending magnets. The achromat lets the beam pass through a narrow aperture in the main dump-collimator, the TAX, that permits a narrow band momentum selection of $\pm 1\%$ $\Delta p/p$. In the TAX the remaining primary proton beam is dumped. In the next part of the beam line, the beam

is collimated and re-shaped to become parallel at the CEDAR. This detector is filled with nitrogen gas over a length of approximately 6 meters and is used for positive kaon tagging. After the CEDAR detector the 75 GeV/c kaons go through a second achromat and are precisely measured via three tracking stations, the GTK 1-3, composed of Si-pixel arrays. Before GTK3 a horizontal steering magnet, called TRIM5, serves to deflect the beam by an angle of 1.2 mrad to match the downstream spectrometer design [50].

7.3 Optics Studies for K12

The first step of the studies developed for K12 is focused on the beam optics. These studies are carried out in MADX and BDSIM. In order to define a beam line in MADX only the information on the normalised field strengths and the lengths of all magnets is needed. The transverse size and the aperture of the magnets can be specified but are not taken into account for the optics calculations by the software. This is also true for collimators that can be declared as placeholders in the beam line, but do not interact with the beam. MADX performs optics calculations based on matrix multiplication, where the propagation matrices are derived from the field strength specified for the magnets. One of the standard outputs of MADX is in Twiss format, a file that contains all the information that can be derived from the Twiss parameters, see Chapter 3. A MADX Twiss file can easily be converted into a BDSIM model for optics comparison using the functionalities of the PYMADX [104] software. The BDSIM model created from the MADX model contains magnets that use the standard classes defined in BDSIM (see Chapter 5 for the BDSIM geometries). After having created these first two models the simulations can be run. In this case since the beam-matter interaction is not taken into account there is no need to specify a physics list in BDSIM.
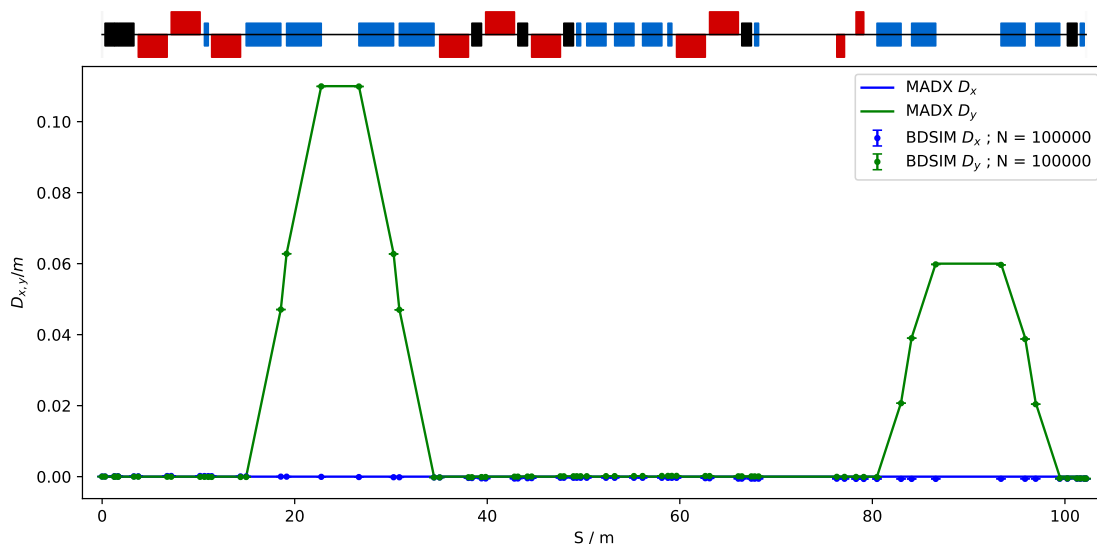
Figure 7.2: Dispersion functions in the X and Y planes as function of distance along the beam calculated for 10^6 primary particles. Continuous line for MADX, points for BDSIM.

The comparison between MADX and BDSIM is particularly interesting, since the two codes use a different approach to the optics calculations. MADX uses the aforemen-
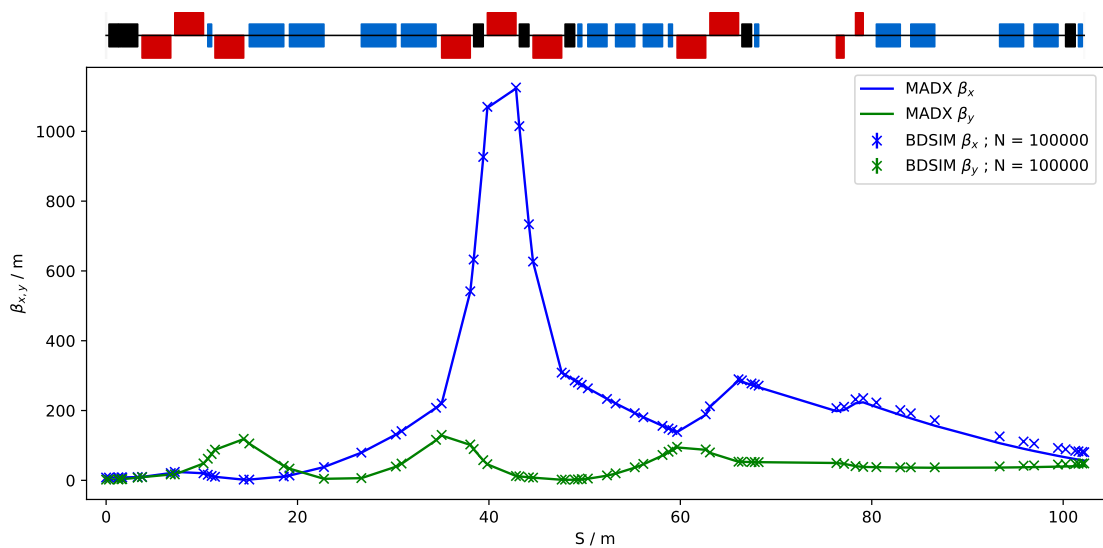
Figure 7.3: Beta function in the X and Y planes as a function of the distance along the beam calculated for 10^6 primary particles. Continuous line for MADX, points for BDSIM.

tioned matrix multiplication method, whereas BDSIM instead tracks all the particle in the lattice, extrapolating afterwards the optics parameters such as dispersion and beam size. The simulated beam for these studies is a 75 GeV/c positive kaon beam with 10^6 primary particles. The comparison plots can be created using PYBDSIM [105]. On the top of the plot of Figure 7.2 one can see a schematic of the beam line. In this survey the blue blocks represent dipoles, the red ones quadrupoles and the black ones the collimators. It is demonstrated in Figure 7.2, thanks to the dispersion curve, that most of the dipoles do not apply a bend and are used as muons sweepers for cleaning the beam from the background particles. The achromats bend in the vertical plane and produce a change in the dispersion visible at the locations around 15-35 m (for momentum selection) and 80-100 m (for spectrometry) along s. The beta-Twiss function along the beam line can also be plotted, see Figure 7.3. This function is related to the beam-size (σ) of a Gaussian beam via the relation $\sigma = \sqrt{\epsilon\beta + (\Delta p/p)^2}$, where ϵ is the emittance of the beam and p the momentum. MADX results are plotted with solid lines, whereas BDSIM's are represented with points at the end of each sampling plane (end of every beam line element). It can be noticed that there is a good agreement between MADX and BDSIM within the relative error-bars. These results are important in order to verify the compatibility of BDSIM and MADX, since MADX is the main software used for optics design at CERN. These studies are followed (see next section) by the creation of a 3-D model in BDSIM and FLUKA that replicate all the single components of the beam line. These models will be used for

background studies on NA62.

7.4 K12 3-D Monte-Carlo models

NA62 is a high precision experiment. Therefore, MC simulation models need to be precise enough to adequately describe the data, study the various sources of backgrounds for the experiment and quantify the generated radiation dose (on shielding and outside the experimental hall). Two models have been created for this purpose, one in FLUKA and one in BDSIM. The two models have different applications: FLUKA is used for radiation studies (currently being studied by the CERN Radiation Protection group), thermal effects on materials and characterisation of background events generated by beam interaction with the residual gas of the vacuum tank, see Section 7.9. BDSIM is used for the characterisation of the muon background generated at the NA62 detector. The fact that these two models cover different scopes leads to partially different structures of the two: the FLUKA model includes a more detailed experimental hall geometry to take into account every possible source of radiation as is shown in the rest of this section.

7.4.1 K12 components

The K12 beam line contains a number of magnets, collimators and detectors (also vessels and windows that are not included in the models). There are nine different magnet models, all with different apertures, yokes and coils, see Table 7.1. Magnet yokes are made out of iron and the coils out of copper. Copper density varies somewhat between the different magnet types. The reason for it is that the coils contain internal pipes that are used for water-cooling and have different shapes for each magnet type. The collimators used are eight in total (including the TAX) and have all different shapes and apertures, see Table 7.2. The detectors in K12 are only two, the CEDAR and the GTK, already discussed in Chapter 4. There are also some other detectors used for beam tuning and scanning such as the FISCS, MWPC and XION that are not included in this model [39].

7.4.2 FLUKA and BDSIM models

The design of the 3-D elements for the MC models have been executed in FLUKA (using FLAIR) and in BDSIM (using GDML geometries) following the technical drawings and 3-D models available at CERN (in CATIA format [106]). The main differences between the design in BDSIM and FLUKA is that in FLUKA the components are designed in a unique file using a global reference frame that has a fixed origin; while the GDML geometries

Magnet Type	Magnet Name	Half-Aperture 1 (cm)	Half-Aperture 2 (cm)	Yoke Length (m)
Quadrupole	QNR	3	-	3
Bending	MDX	5.2-10	8	0.4
Bending	MTR	3.6	25	3.6
Quadrupole	QNL	4	-	3
Bending	MBPL	11-20	20	2
Quadrupole	QFS	5	-	0.8
Bending	MCB	8	16	2.5
Scraper	SCR	3	14	5
Bending	MNP	120	160	1.3

Table 7.1: List of magnets used in the K12 beam line. The Half-Aperture 1 and 2 parameters for the bending magnets and scraper are relative to the aperture height and width respectively. For the quadrupoles instead, only one parameter (Half-Aperture 1) is needed to quantify the radius of the aperture.

Collimator Type	Collimator Name	Half-Aperture 1 (cm)	Half-Aperture 2 (cm)	Length (m)
Circular Aperture	CuCol	0.75	-	0.95
Circular Aperture	TCX	1.4	-	1.6
Circular Aperture	TAX	0.75-1.4	-	3.2
2-jaw collimator	XCSV	1.7	-	1
2-jaw collimator	XCSH	-	2.5	1
2-jaw collimator	XCSV	0.15	-	1
4-jaw collimator	XCSHV	1.5	2.7	1
Rectangular Aperture	TCX	2	3.8	1.2

Table 7.2: List of collimators used in the K12 beam line. The Half-Aperture 1 and 2 parameters for the 4-jaw and rectangular collimators are relative to the aperture height and width respectively. For the circular collimators instead, only one parameter (Half-Aperture 1) is needed to quantify the radius of the aperture. The 2-jaw collimators, collimate only vertically or horizontally, Half-Aperture 1 represents a vertical aperture, while Half-Aperture 2 the horizontal aperture.

have to be designed independently (single file per geometry). In a GDML file the origin of the reference frame is fixed by the first component defined in the geometry, all the other parts are positioned relative to the first.

The magnetic field of the K12 magnets are mostly defined by two-dimensional field maps, there is only one three-dimensional map that is used for the MNP (called also MNP-33) magnet. These fields were simulated using the OPERA software or extracted from the HALO software (see Chapter 5). The maps need to be reshaped in order to fit the structure adopted by FLUKA and BDSIM; this was achieved with the use of PYTHON and C++

scripts. BDSIM uses predefined classes for importing field maps and integrating over the length of the magnets. It is possible to choose from different types of interpolators and integrators in BDSIM. For these simulations a linear interpolation was used and a classic 4th order Runge Kutta integrator [107]. FLUKA does not provide a predefined function to import field maps from a file and therefore a FORTRAN routine was written in order to linearly interpolate the field in space and assign it to the right regions.

7.4.3 K12 beam line development

The first part of the beam line designed is the container of the target (called BAC) followed by the quadrupoles (QNRs) and the MDX magnet that is a trimmer magnet, see Figures 7.4, 7.5 and 7.6. These models are prepared in FLUKA and BDSIM using the approach described above and assigning the correct material to all the components.
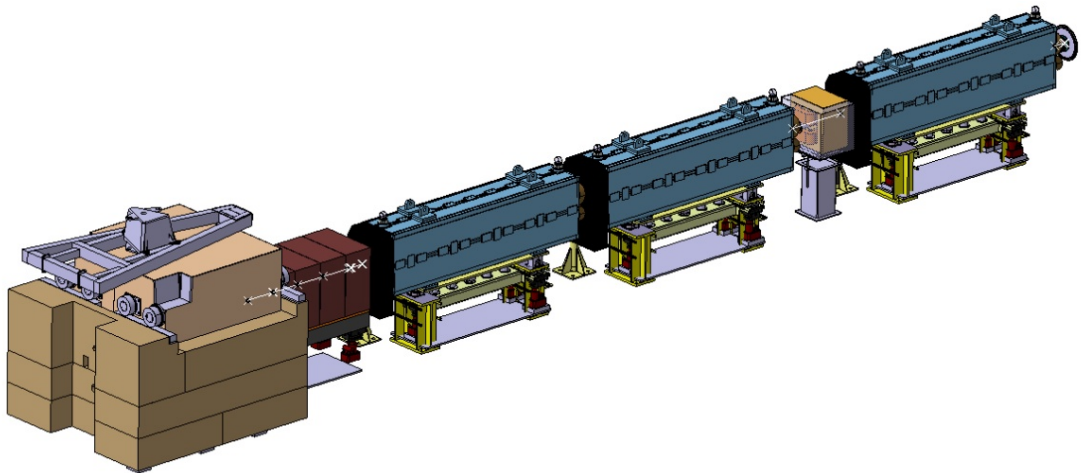
Figure 7.4: First few elements of the K12 beam line visualised in CATIA. The T10 container (called BAC) is followed by the TCX collimator and three quadrupoles (QNRs) plus a small trimmer (MDX).

The BAC and the TCX are composed of the same material, an iron alloy. The collimator contained in the BAC is made of a copper alloy (CuZrCr), while the target (T10) is made of beryllium. The T10 target has been approximated in the simulations by a straight cylinder of 2 mm diameter and 40 cm length. In reality T10 is composed of four Beryllium rods that are disposed one after the other and are held by thin (25 μm) aluminium foils (that have not been included so far in the model). After the TCX there are three quadrupoles, the QNRs, and a trimmer magnet, the MDX. Following these magnets there is the first achromat and the TAX, see Figure 7.7. The TAX can be divided in two
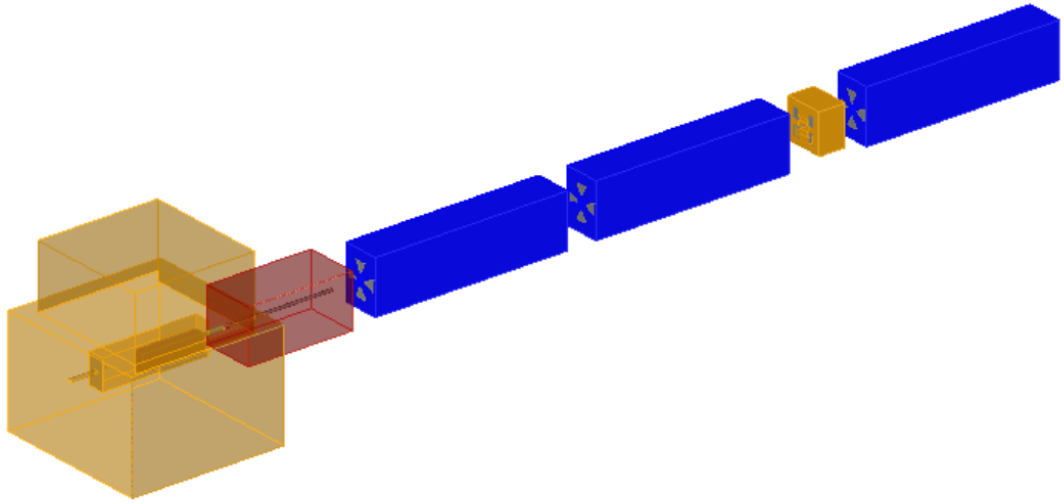
Figure 7.5: First few elements of the K12 beam line modelled in BDSIM using GDML components. The T10 container (called BAC) is followed by the TCX collimator and three quadrupoles (QNRs) plus a small trimmer (MDX). By default BDSIM plots all the components imported from GDMLs in grey and the color can be assigned afterwards without matching the material of the geometry.
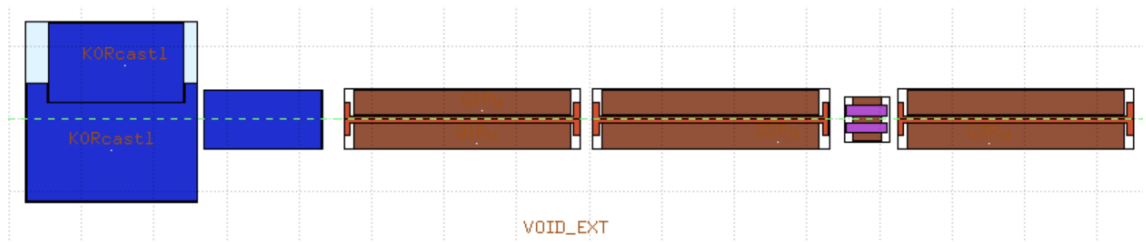
Figure 7.6: First few elements of the K12 beam line modelled in FLUKA using FLAIR. The T10 container (called BAC) is followed by the TCX collimator and three quadrupoles (QNRs) plus a small trimmer (MDX). By default FLUKA plots all the components using a color that is assigned internally to the type of material.

main modules (TAX1 and TAX2) that can be moved vertically independently. Each part is made of four blocks in which three holes are drilled. The first two blocks of the first module are made out of copper and the following two are made out of iron. The blocks of the second module are all made of iron. The holes of the TAX are either filled or shaped using tungsten inserts, this allows to move the two vertically with respect to the two modules of the TAX in order to achieve different particle selection or dumping (in case no hole is aligned). NA62 uses the configuration of the TAX where the beam passes through the central hole of both TAX modules and the other unwanted particles moving away

101
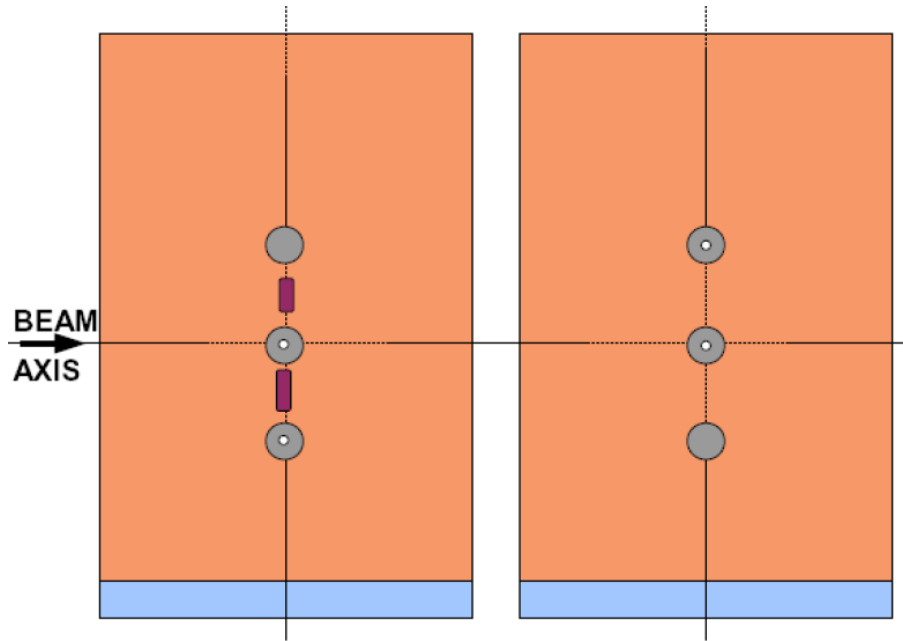
Figure 7.7: Front view of the two modules of the TAX. All the holes are filled with tungsten inserts, these are either open (with a white circle in the centre) or completely closed [50].
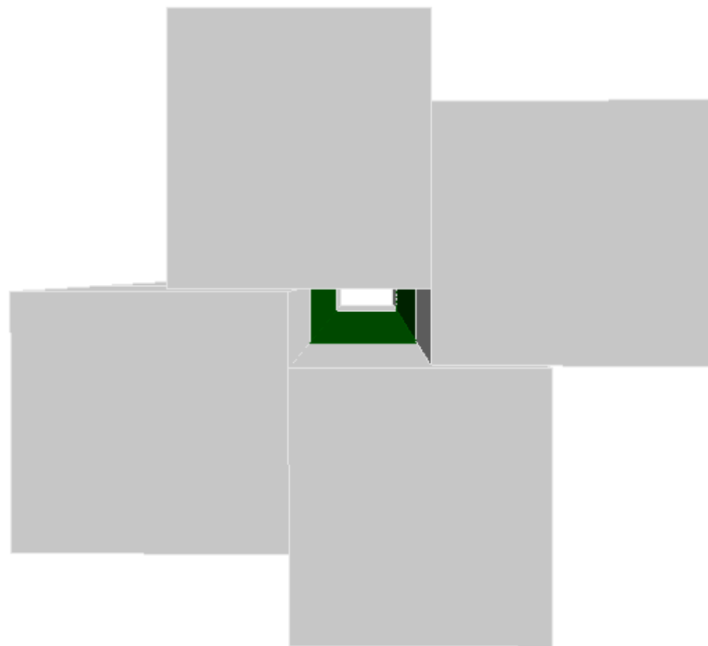
Figure 7.8: 4-jaw collimator of the K12 beam line visualised in BDSIM. The collimator has four jaws that can be adjusted in order to reach different apertures. This component contains tungsten shim plates in the internal part (in green) and is made of iron.

from the reference trajectory are dumped on the TAX. The achromat is followed by three more quadrupoles (QNLs), three more MDXs and three collimators. The collimators are
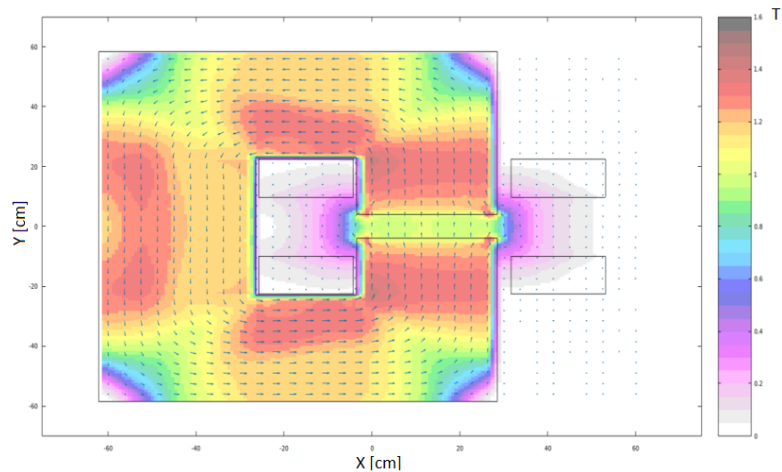
Figure 7.9: MCB magnet designed in FLAIR and relative magnetic field. It can be seen that in the centre of the magnet there is a field-free passage for the central beam.
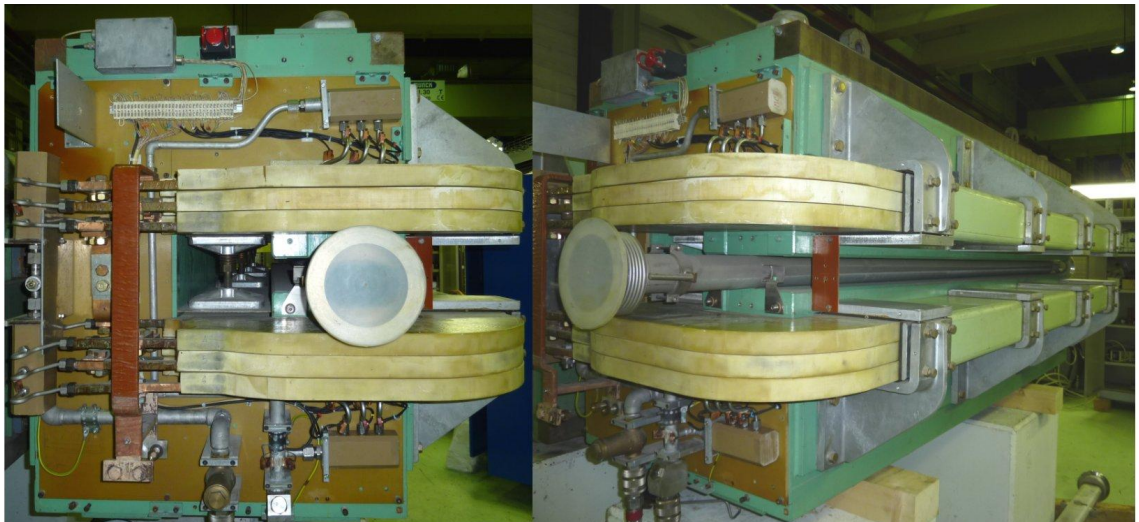
Figure 7.10: MCB magnet photograph available in the CERN NORMA database [108].

in iron and contain tungsten or aluminium plates in the central region in order to optimise the reshaping of the beam. This part of the beam line is followed by three MBPLs, that are sweeping magnets. These are bending magnets with an iron insert in the central gap with a small hole in order to create a field-free region for the central beam and to sweep the muons passing through the yoke. These sweeping magnets are followed by two more quadrupoles, two MDXs and a 4-jaw collimator (see Figure 7.8) before the CEDAR. The latter is represented in the simulation models with a volume of gas and does not contain any additional material. After the CEDAR, there are two focusing quadrupoles (QFS) that focus particles through the last achromat onto the main NA62 detectors. The last achromat is composed of four C-shape bending magnets (MCBs) and a scraper that has
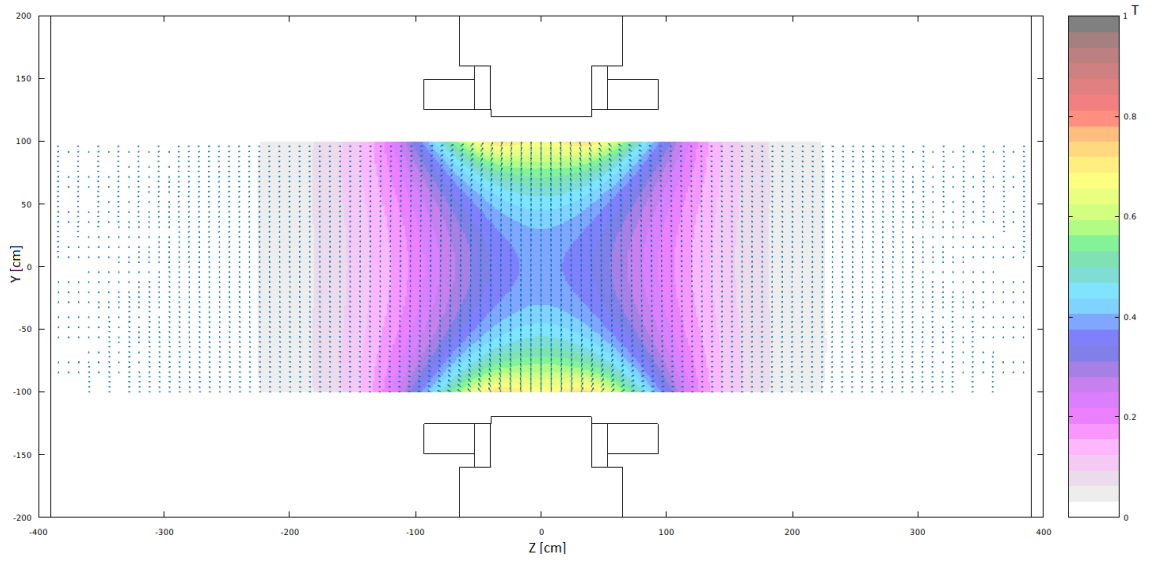
Figure 7.11: YZ view of the MNP magnet and the relative field map visualised in FLAIR.
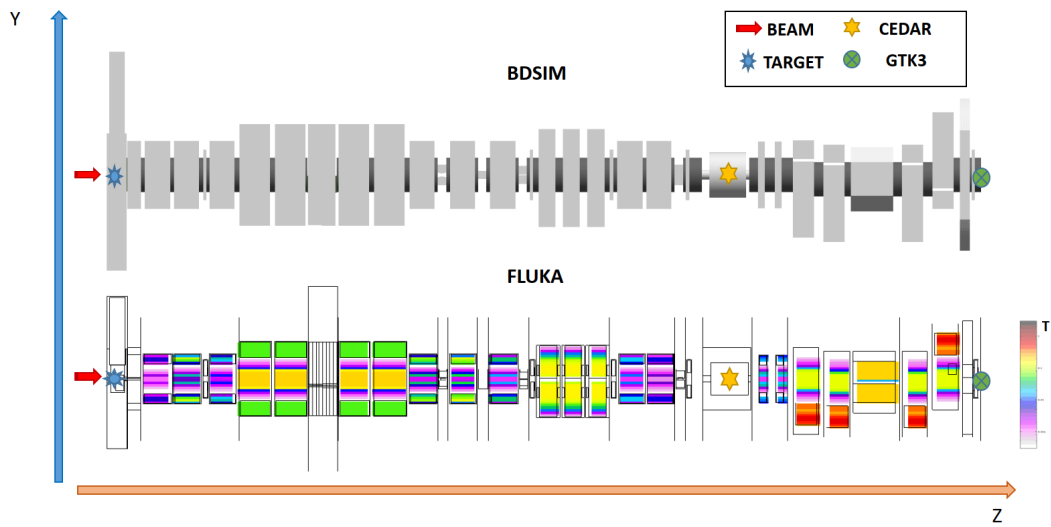
Figure 7.12: K12 model in BDSIM and FLUKA. In FLUKA the magnet's fields are shown.

the role to sweep the remaining muons in the beam line using a toroidal field in the magnet yoke. One of the MCBs is shown in Figures 7.9 and 7.10. In the last achromat there is the GTK that is represented in the simulations by very thin layers of silicon, approximately 200 μm. The GTK is divided in three stations and tracks the beam going through. After the achromat there is a final massive collimator, and the final trimmer that gives a kick

104

to the beam in order to match the detector orientation downstream. Two more magnets have been implemented in the beam line model that are not in K12 but are still part of the NA62 experiment, the large MNP magnet, that is used with the STRAW spectrometer and the final bending magnet, and a final MBPL that separates the remaining beam into a neutral (that must be vetoed by the SAC calorimeter) and charged component before it reaches the beam-dump placed at the very end of NA62, where the final beam is completely absorbed. The field of the MNP magnet is three-dimensional (see Figure 7.11) and for this purpose another routine had to be written in FLUKA in order to generate a tri-linear interpolation. The full models of the K12 beam line have been assembled following a BEATCH file as a reference for all the positions. The complete model of the finalised high-detail K12 beam line can be seen in Figure 7.12.

7.4.4 Shielding, experimental hall and detector design

After this first design step, the models have been extended to include the shielding blocks surrounding the beam lines, the experimental hall and the NA62 detector. These components do not directly impact the composition of the 75 GeV/c positive beam, but play a role in the characterisation of the halo particles that propagate outside the reference path. This is of particular relevance for particles that contribute to the experiment background, such as muons, that represent the main contribution to the NA62 background. The K12
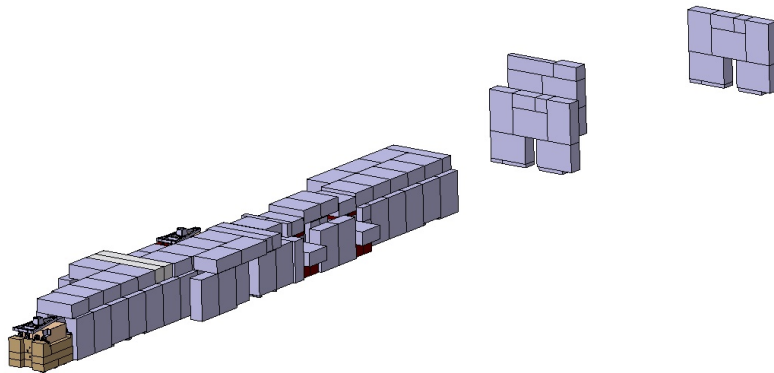
Figure 7.13: K12 shielding model visualised in CATIA.

shielding is composed of rectangular blocks closely surrounding the beam line. These are mainly made of concrete, but iron is also used in the higher radiation areas, such as the region of the first achromat. These blocks cover a length of approximately 40 m. Three consecutive concrete walls are placed downstream the blocks, and provide extra screening for particles at large angles, see Figure 7.13. The shielding was first drawn in FLAIR
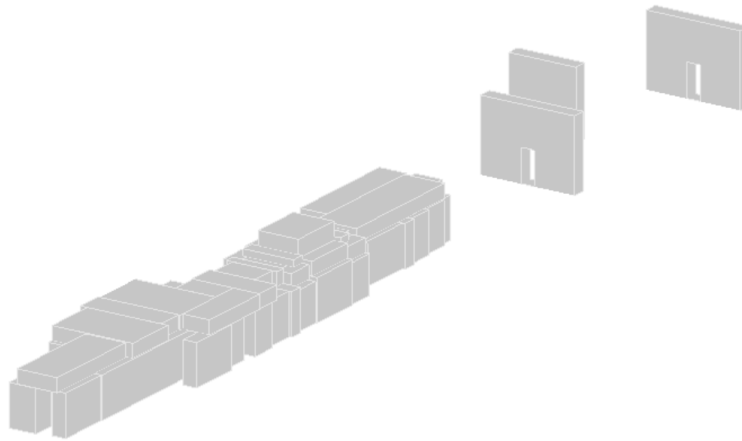
Figure 7.14: K12 shielding model and visualised in BDSIM.

and implemented in the FLUKA model and afterwards converted to GDML thanks to the functionalities software PYG4OMETRY, see Figure 7.14. This geometry is one of the first ones converted using this software and served to test the capabilities of PYG4OMETRY when it was still in development [89]. The conversion from FLUKA to GDML format is indeed not trivial and requires a complex algorithm to be developed.

The detector design was executed in BDSIM and FLUKA using all the detector elements described in Chapter 4. The information of the density of each material was retrieved from the NA62 techical design report [50]. The density for gaseous detectors was calculated using the ideal gas law. For some layered detectors, such as calorimeters, an average density was calculated and used for the full component. The cavern in BDSIM was drawn
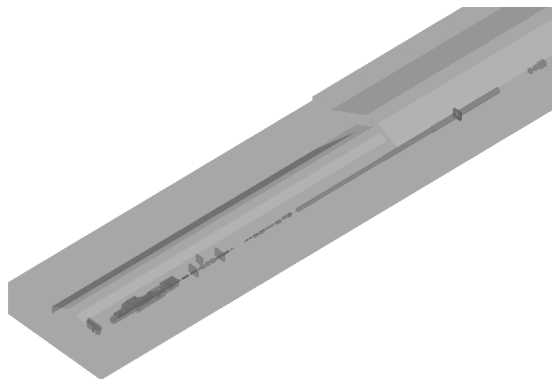
Figure 7.15: Beam line and detector placed within the ECN3 experimental hall visualised in BDSIM.

using two layers, one layer of concrete that represents the walls surrounding the beam line and one layer of soil that surrounds the concrete layer. Indeed, for the background studies

done in BDSIM the walls of the cavern are the most important element since they can contribute to the adding more background events. The soil, being the most external layer, does not influence the flux in the experiment but rather in the region outside the cavern. One of the purposes of the FLUKA model is to be used for radiation studies, therefore a high detailed model of the shielding is required (see Figure 7.16); it is indeed in the interest of the experiment to study all together with the radiation in the experimental hall also the radiation that is produced in the external environment. This model is in fact currently employed by the Radiation Protection group at CERN in order to estimate the radiation levels reached in the area outside the experiment.
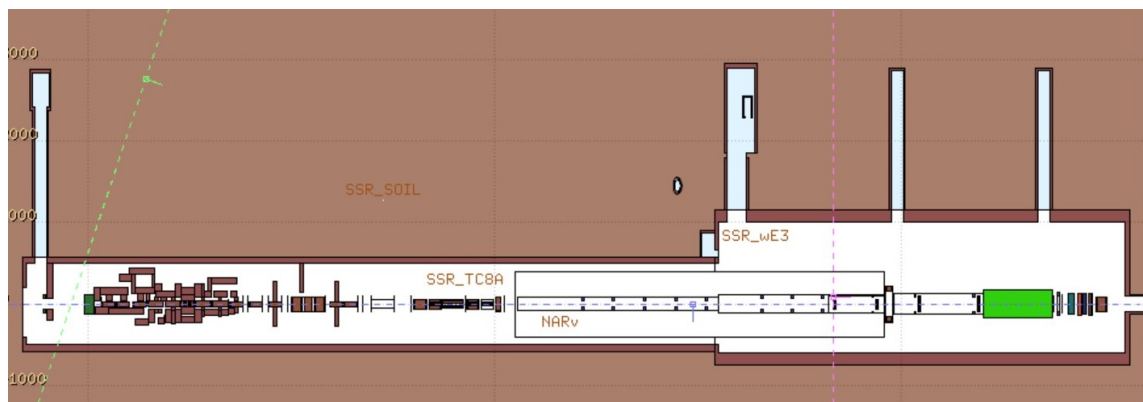
Figure 7.16: Beam line and detector placed within the ECN3 experimental hall visualised in FLUKA.

7.5 Studies of the K12 beam

The first studies carried out using these models are based on the characterisation of the 75 GeV/c positive beam. These studies aim to compare the beam obtained from the simulations to data and benchmarking the two models. The beam size and angular distribution are the observables that are used for this purpose in this section. For the first studies, in order to limit computation time, proton interactions on target have not been propagated. Instead, a K^+ beam distribution after the target has been assumed with parameters obtained from sensitivity studies.
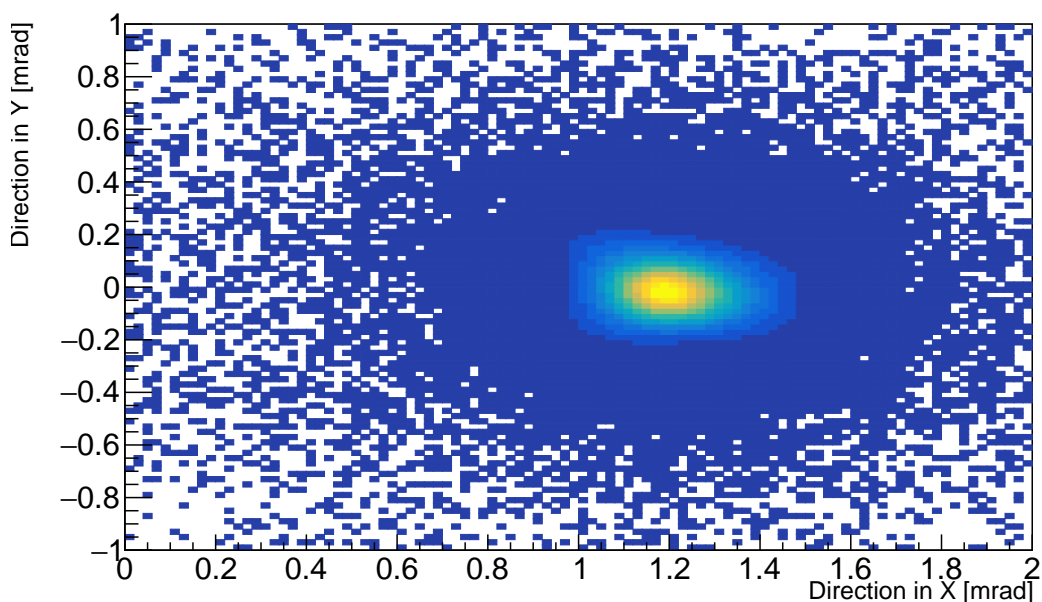
Figure 7.17: 2-D angular distribution of the positive kaon beam at the GTK3 from NA62 data of 2018.

These studies helped in the calculation of the initial maximum angle and position at which primaries would still be propagated through the beam line. For these studies, the version 2011-3.0 of FLUKA and 3.0-8a of FLAIR were used. Also, BDSIM version 1.4 with GEANT4.10.4.p03 and GEANT4 physics list FTFP-BERT. 10^7 primary particles (K^+) were run for both BDSIM and FLUKA.

One of the observables in the experiment is the angular distribution of the beam at GTK3. This observable is particularly interesting, since the beam needs to be kicked by exactly 1.2 mrad by the last trimmer magnet (TRIM5) in order to match the detector downstream. Data for beam distributions (angular and spatial) were provided by the NA62 collaboration in order to benchmark the simulations. A scatter plot of the angular distribution measured

by NA62 at the last GTK3, after the last trimmer, is depicted in Fig. 7.17. The one-dimensional projections on the X and Y axes of the data are shown together with the results from FLUKA and BDSIM, both normalised to the integral on Figure 7.18.
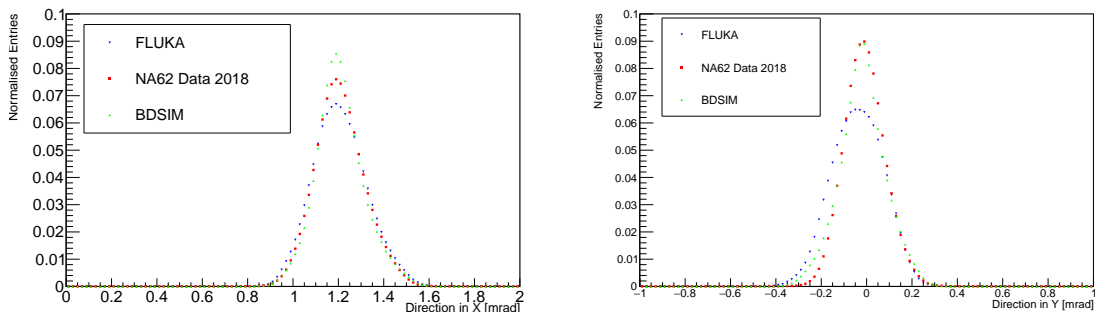
Figure 7.18: Angular distribution of the beam at the GTK3. The X and Y projections of the data and simulations (in BDSIM and FLUKA) can be seen on the left and on the right, respectively.

It can be seen that the particles following the kick of TRIM5, correctly distribute around the expected 1.2 mrad direction in the horizontal (X) plane at GTK3. While regarding the Y axes, the beam is distributed around zero, as expected. Table 7.3 lists directional and spatial beam parameters at the GTK3. Average X and Y ($\overline{X}, \overline{Y}$) and their RMS are reported for measurement data, FLUKA and BDSIM.

Table 7.3: Beam Parameters at GTK3

POINTS	$\overline{X}$	$\overline{Y}$	RMS X	RMS Y
FLUKA ANGLE [mrad]	1.21	-0.04	0.12	0.11
BDSIM ANGLE [mrad]	1.21	-0.02	0.11	0.11
DATA ANGLE [mrad]	1.21	-0.01	0.11	0.09
FLUKA BEAM [cm]	0.04	-0.02	1.01	0.66
BDSIM BEAM [cm]	0.03	-0.02	1.01	0.60
DATA BEAM [cm]	-0.01	-0.01	1.05	0.58

The curves show some differences, in particular, concerning the Y direction curve. This kind of discrepancy could be caused by the muon sweeping system of K12 that is made of MBPLs. For these a 0 field in the aperture is assumed in the simulations, but in reality a residual field (of a few milli-Tesla) is always present. Even such a low field could lead to a discrepancy of the order of what is shown in Figure 7.18. The small difference between FLUKA and BDSIM is instead probably given by the different implementations of fields in the codes. In FLUKA the field maps are attached to a box containing the full magnets geometry while in BDSIM the field is attached to the geometry of the magnet directly; this implementation could lead to the discrepancy seen in Figure 7.18. The differences

in results between the two codes are negligible if compared to the precision reached with previous software for the K12 beam line; therefore the agreement is considered satisfactory.

7.6 Studies for the CEDAR detector

After checking the compatibility of the models for the beam characteristics, more studies were done to check the beam characterisation at the CEDAR detector, see Chapter 4. In NA62, kaons cannot be separated from pions and protons at the beam level [109]. For this reason the CEDAR detector is needed to perform particle identification. In the current configuration, the CEDAR uses nitrogen at 1.73 bar, but this detector could work almost as well with hydrogen at 3.85 bar. The aim of these studies is to calculate the divergence that the two possible configurations would generate. Divergence needs to be minimised for various reasons, in particular: to avoid showers produced by particles at large angles and to reduce the emitted radiation affecting NA62 electronics.
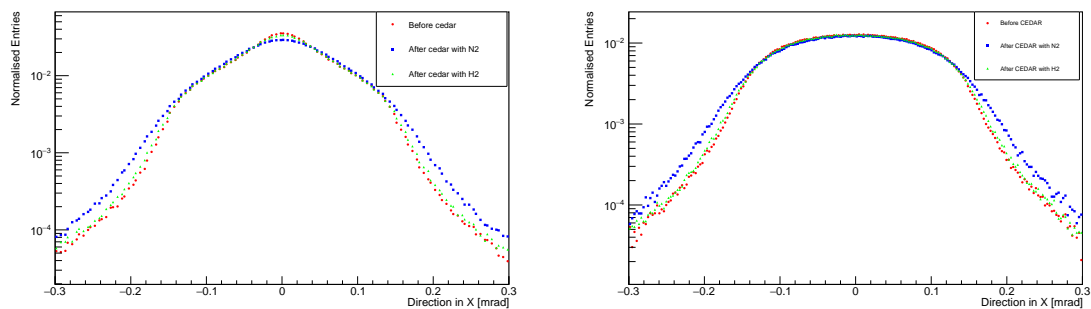
Figure 7.19: Angular spread of the beam before CEDAR and after CEDAR with N_2 and H_2. Simulations in FLUKA on the left and BDSIM on the right.

The divergence is calculated as the RMS of the angular distribution for the curves shown in Figures 7.19. The RMS parameters are reported in Table 7.4. It can be seen from the simulation curves that the angular distribution is slightly narrower according to BDSIM [110]. In both cases the nitrogen filling of CEDAR causes a wider spread, visible especially for the tails of the distributions. For these reasons the use of hydrogen for this detector was considered. These results led to the preliminary conclusions that hydrogen could reduce the background for the experiment and therefore a new CEDAR adapted to this gas was recently purchased. The tests of this detector are foreseen to take place in 2023.

Table 7.4: Divergence (RMS of Angular Distribution) Before and After CEDAR

DIVERGENCE	Before CEDAR	H2 CEDAR	N2 CEDAR
FLUKA [μrad]	82.17	83.38	88.27
BDSIM [μrad]	68.46	69.98	75.46

7.7 Muon Studies in K12

Another step in benchmarking the two models is to compare particles that do not belong to the 75 GeV/c positive beam of K12 and are produced by particle interactions with the beam line material and subsequent decays. This is the case of muons, which play a fundamental role in the NA62 background studies. The characterisation of the muon distribution is particularly useful for the main $K^+ \to \pi^+ \nu \overline{\nu}$ decay, where the decay $K^+ \to \mu^+ \nu_\mu$ represents the main background source, however not the only one. This type of background influences indeed the tests of lepton universality, done via the precise determination of the underlying form factor parameters and branching fraction of the kaon decay mode $K^+ \to \pi^+ \mu^+ \mu^-$ [111], as well as dark matter candidate searches in beam dump mode [70] (see next chapter for dark matter experiments).

The muons in K12 are mainly created by the interaction of protons on target and on the TAX collimator that generate $\pi^\pm$s decaying into muonic channels. As seen in the previous section, these are swept away mainly by the MBPLs that allow a reduction of a factor 10 in muon flux intensity. Muons that survive the sweeping and are produced by decays downstream of the scraper can still generate the main background in the experiment.
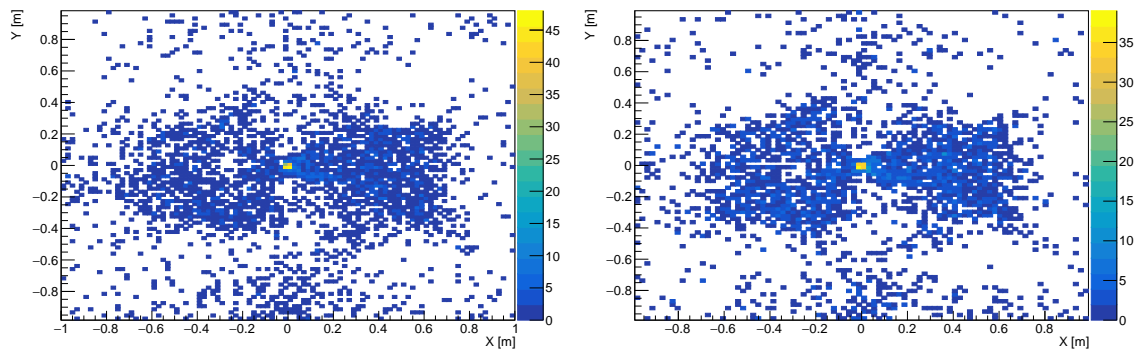
Figure 7.20: XY distribution of muons simulated in FLUKA and BDSIM scored at the plane after the third MBPL magnet (MBPL3).

Table 7.5: Muon beam distribution characteristics along the K12 beam line at various locations.

Location	Software	Number of Particles	$\overline{X}$	$\overline{Y}$	RMS X	RMS Y
MBPL3	BDSIM	5072	-1.98	-7.95	36.44	32.55
MBPL3	FLUKA	4572	-2.64	-7.17	37.28	33.54
GTK3	BDSIM	858	-8.07	3.19	52.51	39.96
GTK3	FLUKA	758	-11.19	-5.24	52.51	46.13
MUV3	BDSIM	334	-5.16	0.11	24.71	25.79
MUV3	FLUKA	265	-5.64	1.27	20.63	21.66
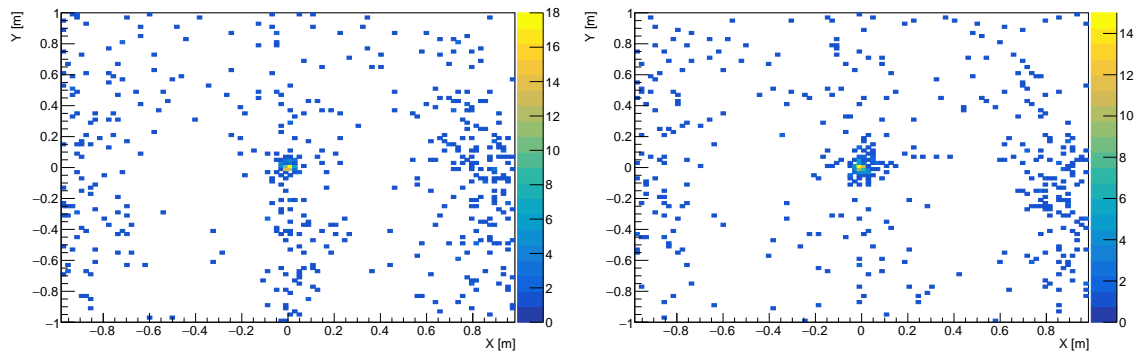
Figure 7.21: XY distribution of muons simulated in FLUKA and BDSIM scored at the plane after the third GTK station (GTK3).

The muon distribution at various locations in the beam line can be compared between the two models, built in FLUKA and BDSIM. These studies are done with 10^6 protons on target using the same physics lists and software versions mentioned in the previous section. A comparison of the muon distribution in the transverse plane XY after the third MBPL (MBPL3) and the third GTK station (GTK3) is depicted in Figure 7.21. These plots demonstrate that the muon distribution pattern is similar and comparable between the two codes. This is the first step for the two software particle production benchmarking. A detailed study of the muon distribution is currently ongoing within the NA62 Monte-Carlo simulation group that is using the BDSIM model for this purpose, see next section.

113

7.8 Beam Background Simulation Studies in BDSIM

This section covers the comparison of the BDSIM model for muon distribution studies with the data from the NA62 experiment, the so-called muon halo distribution. The simulation was run with protons colliding on the T10 target. For the high-statistics simulation of the whole K12 beam-line, the BDSIM version 1.4 compiled with GEANT4.10.6.p02 was used, employing the physics list QGSP_FTFP_BERT. The initial $p = 400$ GeV/c proton beam is placed right before the target using beam parameters taken from a previous K12 beam line simulation study [70]. After colliding with the target, the protons produce several secondary particles that are further propagated through the BDSIM-K12 beam line model until the upstream face of the NA62 CEDAR detector. After the CEDAR the information about all the particles is stored at this specific z-position using a ROOT format. This information is afterwards used as an input for the NA62 Monte-Carlo (NA62MC) software [112], also based on GEANT4.10.6.p2, that takes over this particle information and propagates them downstream through the full detector setup. The generated hits in the sensitive detectors of the NA62MC are sent to the NA62 reconstruction software. There, the detector hits from simulated (forced) kaon decays are overlaid with those hits from the simulated muon background, taking into account the probability of an event with at least one muon produced in a proton-on-target (POT) interaction. The time lapse for overlaying the hits in this manner, including also hits from other beam background sources as described before, is $\pm$ 400 ns. After this process, the reconstruction software then generates the hit events according to the real detector read-out system procedures and finally creates output similar to track information reconstructed from real data. For these studies, $4.7 \cdot 10^{10}$ POT events were simulated on the CERN HPC farm [113]. In the rest of this section, BDSIM denotes the combined BDSIM and NA62MC models. The first investigation for this model is done on the relative contribution to the total charged particle rates of particles with momentum in the range of $60 < p < 80$ GeV/c scored at the CEDAR detector. Table 7.6 shows that the values obtained with BDSIM are comparable to the Atherton parametrisation based on measurements and interpolation made at the CERN North-Area [37]. The contribution of particle rates outside this momentum range is negligible. The agreement is satisfactory within expectations, when looking at the total rates of the different particles. The proper simulation of the additional particle rates besides the kaon rate in the beam is essential for the study of the background

induced additionally by particle decays, i.e. predominantly by those of pions, as well as by particle production due to inelastic interactions with the beam line material. Material interactions can also cause particles to scatter into the sensitive detector volume, triggering extra detector activity that needs to be evaluated to isolate it from the activity from decay products.

Particle	Atherton [MHz]	BDSIM [MHz]
π^+	525 (70 %)	478 (70 %)
p	171 (22 %)	159 (23 %)
K^+	45 (6 %)	44 (7 %)
Total	750 (100 %)	681 (100 %)

Table 7.6: Particle rates (and relative contribution) in the 75 GeV/c mean momentum beam at CEDAR plane from estimates based on measurements in [37] and in the BDSIM simulation.
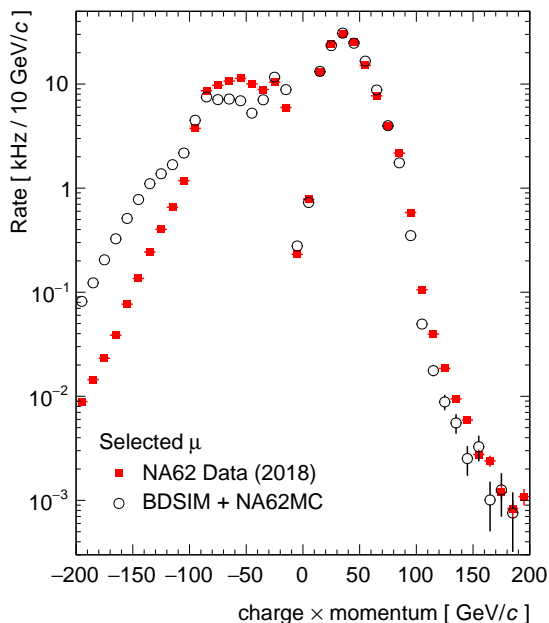
Figure 7.22: Rate of halo muons as function of charge times momentum. BDSIM results combined with NA62MC are displayed as black circles (solid), the other markers represent NA62 data from different recording periods of Run 1.

The muon rates cannot be directly measured at or close to the CEDAR plane, that is the transition point between BDSIM and NA62MC, in the period between 2016 and 2018 (Run 1). With more detectors installed in 2021, however, this will become possible and comparison studies in this plane will be done for the data acquisition period between

2021 and 2024 [114]. For the studies presented in this chapter, an analysis strategy was implemented to select the halo muons, defined as the muons out of experiment trigger time, that hit the gaseous tracking detector (STRAW) and the MUon Veto 3 (MUV3) detector. More selections were applied according to the ratio of energy over momentum E/p as well as the geometrical acceptance of the detector. Figure 7.22 shows the charge times momentum distributions of halo muons from NA62 data for the 2018 data acquisition period, together with those from BDSIM simulation. For positive muons, the comparison between BDSIM simulations and data shows a good agreement as depicted in Figure 7.22. The negative muons are well described by the simulations up to momenta of $p = 40 \text{ GeV}/c$. For higher momenta, between $40 - 100 \text{ GeV}/c$, a clear difference is visible, even if the curvature of the data is approximated by the BDSIM simulation. For momenta above $p = 100 \text{ GeV}/c$, the spectrum in BDSIM is higher than in data. This type of effect could be caused by the GEANT4 physics list and the underlying particle production and fragmentation models. Further investigations for the use of alternative physics generators to be used in BDSIM are currently ongoing. Since the observed disagreements in the momentum spectra are predominantly present at low rates, the total rate of halo muons in BDSIM agrees well with that from NA62 data and the total negative muon halo rate only differs from data by 10% (see table 7.7).

Particle	NA62 2018 data [kHz]	BDSIM [kHz]
μ^+	124.0 ± 0.1	124.5 ± 0.2
μ^-	82.4 ± 0.1	74.6 ± 0.1
Total	206.4 ± 0.1	199.1 ± 0.2

Table 7.7: Muon halo rates measured in NA62 2018 data and in BDSIM simulation.

Figure 7.23 shows the spatial distribution of the halo muons (selected as explained before) projected onto the XY plane at the end of the final NA62 collimator ($z = 101.4 \text{ m}$). This figure shows again that the BDSIM beam line simulation is reproducing well the positive muon halo distribution. The high rate locations with positive and negative X (upper row in the figure) present in data are also visible in the simulation. The ratio of data to MC in the lower row of the figure shows that the rates per quadrant are of similar order. For negative muons, however, substantial differences are observed. In particular, as depicted in Figure 7.23 an enhancement at positive X and a deficit in the region around the central bin can be noticed. Taking into account the discrepancy of the momentum distribution at high momenta, the difference in the region around the central beam axis
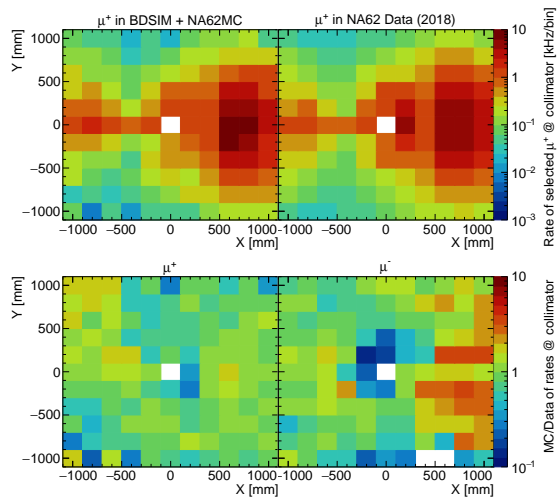
Figure 7.23: Rate of selected halo muons in the NA62 STRAW detector projected onto the XY plane at the end of the final collimator $z = 101.4$ m. The upper row shows results for μ^+ from BDSIM simulation in combination with NA62MC on the left and from NA62 data from 2018 on the right. The lower row shows the ratio of the simulation to data for μ^+ on the left and μ^- on the right respectively. The empty bin at the centre of the plots is the region where the central beam passes.

could be explained with the underestimation of the rates at $p = 40 - 100$ GeV/c. Such an effect could be attributed to the field strength of the muon sweeping magnets, the exact value of the field in these magnet is indeed not known to a high precision and can be therefore not reproduced by simulations. The excess at positive X, though, cannot be interpreted in a similar way and has to be further studied [114].

7.9   Beam-Gas Generated Background

Previous studies of the background for the NA62 experiment showed that background signals can be produced by the interaction of particles in the vacuum tank (see Chapter 4) of the NA62 detector [115]. This effect is particularly relevant when it generates a signal that can be mis-tagged as a kaon decaying into a positive pion and two neutrinos. This kind of event can be generated when a particle decays into a positive pion, detected by the STRAW-tracker, and other particles that are not detected. The non-detected particles would look like two neutrinos, which do not generate any signal. One of these events can be generated by a K_S, generated by a positive kaon hitting a gas molecule, decaying into a positive and a negative pion (see Figure 7.24) with (the positive pion) hitting the STRAW detector and the negative pion not being detected. This type of event is particularly relevant since the kaon short decays very shortly after being produced (the kaon short lifetime is of $8.954 \pm 0.004 \times 10^{-11}$ s) and could not be distinguished from a positive kaon that decays into the $\pi \nu \bar{\nu}$ channel.
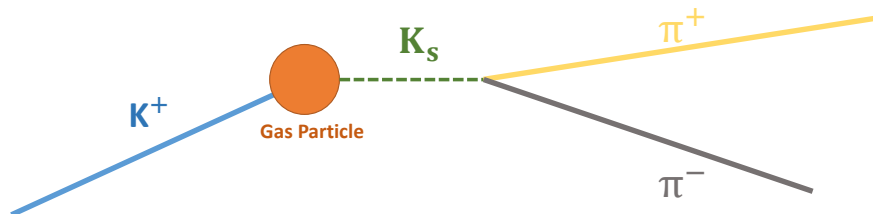
Figure 7.24: Scheme of a positive kaon interacting with a gas particle and producing a kaon short that decays into a positive and a negative pion.

These kinds of effects are simulated in FLUKA. The interaction of the positive kaons with the residual gas of the vacuum tank is a very rare process; the pressure in the tank is indeed 10^{-6} $mbar$. The simulation of these events would require a very high number of positive kaons before seeing interactions. For this reason a FORTRAN routine that

forces the beam-gas interaction was written. Thanks to this routine it is possible to run a limited number of positive kaons that all interact with the gas of the vacuum tank and scale them afterwards to the cross section of the interaction. Along with this routine, a gas distribution along the reference path of the positive kaons is needed, this gas distribution was taken according to reference article [67]. This simulation was run with FLUKA version 4-1.1 using the equivalent of 10^{18} primary protons on target that correspond to one year of NA62 operation. A FORTRAN routine in order to select only the events of the type $K^+ \rightarrow K_s \rightarrow \pi^+ \pi^-$ was written by the author. After running these events and selecting only those that can possibly generate background for the $K^+ \rightarrow \pi^+ \nu \bar{\nu}$ channel, meaning positive kaons that have a momentum between 15 GeV/c and 35 GeV/c, see Chapter 4 for more information on the NA62 event selection. The momentum distribution of the corresponding kaon shorts is depicted in Figure 7.25.
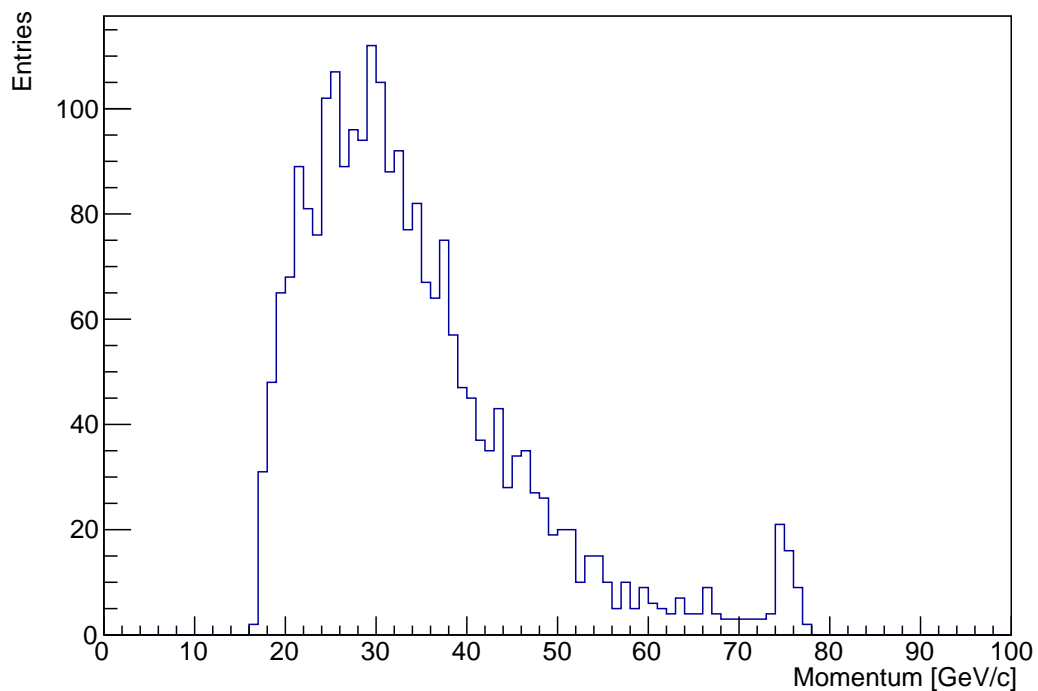
Figure 7.25: Momentum distribution of the kaon shorts that decay into a positive and negative pion produced by the positive kaon interactions with the residual gas in the vacuum tank of NA62.

In this distribution one can see a peak at 75 GeV/c due to charge-exchange events. In these events a K_s exchanges a quark with one of the gas particles becoming a K^+ with a momentum close to the one of the K_s. From these events, the missing mass squared can

be calculated, this is defined as:

$$m_{miss}^2 = (P_{K+} - P_{\pi+})^2 = m_{K+}^2 + m_{\pi+}^2 - 2E_{K+}E_{\pi+} + 2|\overrightarrow{p_{K+}}||\overrightarrow{p_{\pi+}}|\cos\theta_{\pi+K+} \quad (7.1)$$

Where $m, E, \overrightarrow{p}$, are the mass, the energy and the momentum, respectively. $\theta_{\pi+K+}$ is the angle between the direction of the positive kaon and the positive pion. NA62 selects in only two regions of missing mass squared, R1 in the [0-0.01] GeV^2/c^4 area and R2 between [0.026-0.068] GeV^2/c^4. The events falling in these two regions can therefore be selected in the FLUKA simulation data, see Figure 7.26.
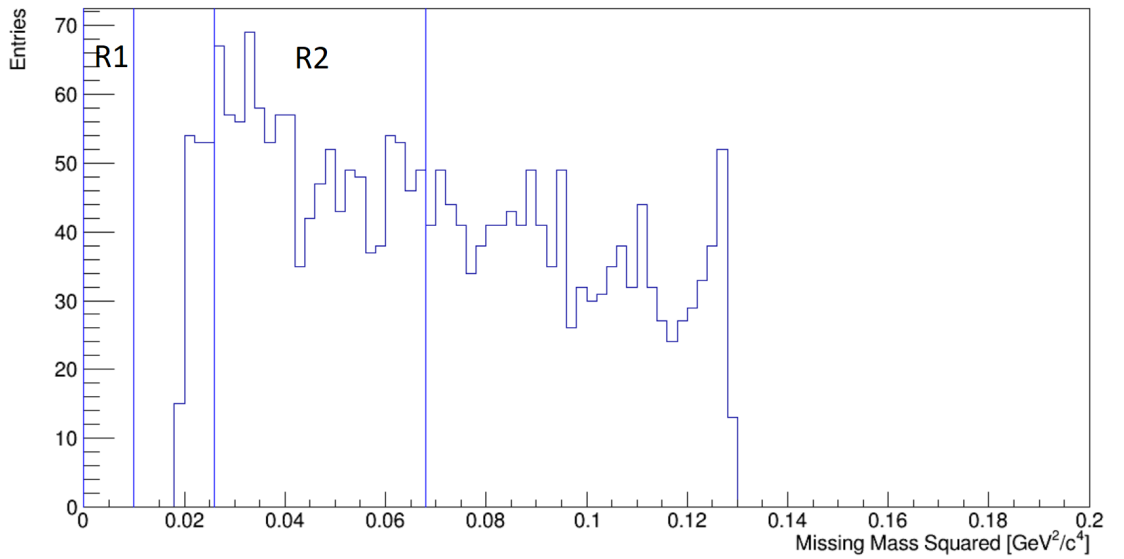
Figure 7.26: Missing mass squared distribution of the kaon shorts decaying into a positive and a negative pion produced by a positive kaon interaction with the residual gas in the vacuum tank of NA62.

Among these events, 935 fall in the selection region. The two pions produced from the decay are strongly boosted in the forward direction, with their trajectories being at a very small angle. The acceptance within the STRAW detector can be calculated from the angle and the distance of the STRAW from the decay point. The simulations show that there are two events (out of the 935) that produce a positive pion hitting the straw and a negative pion that misses it; the latter is anyway detected by the LAV detector that has a 95% efficiency for minimum ionizing particles [50]. Assuming such an efficiency for pions detection, it can be calculated that for a whole year run, 0.1 background events are generated via the $K^+ \to K_s \to \pi^+\pi^-$ channel. This represents an upper limit for the mentioned process, considering that in 2018 the number of detected events is 17, the

background corresponds to 0.6%, a quantity that can be considered negligible.

7.10 Results Summary

This chapter summarises the beam and background studies done for the K12 beam line in the NA62 configuration. Two models were build for this purpose, one in BDSIM and one FLUKA. The two models show a good compatibility with the data for what concerns the particle rates and the beam properties. The optics comparison of the BDSIM model to MADX shows en excellent agreement. The BDSIM model has been used by the NA62 collaboration as a generator for their Monte-Carlo events. In these studies, the background muon rate is well reproduced in the simulation and for the positively charged muons, also the momentum and the spatial distribution is described with good precision over the full ranges. In case of the negative muons more investigations are needed to understand better the deficits in the intermediate momentum region. The overall satisfactory description of the real beam particle background at the entry of the NA62 experimental area with BDSIM is an important contribution to the substantial reduction of the systematic uncertainties in ongoing precision and new physics analyses of the NA62 collaboration allowing for new discoveries beyond the Standard Model. The FLUKA model is currently being used by the CERN Radiation Protection group for radiation studies and for beam-gas generated background interaction. The beam-gas background studies show that the background generation for the decay channel $K^+ \to K_s \to \pi^+\pi^-$ is negligible for the NA62 operation.

Chapter 8

Future Experiments at P42 and K12

In this chapter future experiments on the P42 and K12 beam lines are discussed. These experiments could all be potentially based in these beam lines and are KLEVER, NA62-HI, NA62-BD and SHADOWS. Different aspects are covered for them, since they all have different configurations and requirements, see Chapter 4 for more information.

8.1 Studies overview

Exhaustive studies of the KLEVER experiment beam lines have been done in the past within the EA-LE section at CERN. In particular, a first K12 beam line design in FLUKA was done for this experiment [67]. It was recently found out that the estimated background for KLEVER might be more serious than expected, reaching a rate of the same order of the signal. For this reason the feasibility studies for KLEVER have been extended and are presented in the next section of this thesis. Both KLEVER and NA62-HI would benefit from having a higher intensity proton beam impinging on the T10 target. This is achievable with some modifications of the P42 beam line optics settings, thanks to a technique called T4 bypass that is also presented in this chapter. For NA62-BD and SHADOWS the main aspect to be studied is the muon background that poses the main limitation to the search for dark matter signals. For these studies an approach similar to the one presented for NA62 in the previous chapter is followed;in particular it is shown how the NA62-BD background can be characterised and how the background for SHADOWS can be mitigated.

8.2 The KLEVER beam line

The KLEVER experiment requires an intense beam of K_L mesons that are generated on the T10 target by approximately 2×10^{13} ppp. The T10 target for the KLEVER configuration would be similar to the one currently used for the NA62 experiment, but slightly larger in diameter. The proton angle of incidence for the KLEVER beam is set to 8 *mrad* following a series of studies on the spectra of all neutral particles produced [67] that showed how a non-zero angle of incidence can minimise the background from neutral particles. A key background for KLEVER is from the Λ^0 particle that decays as $\Lambda^0 \to n\pi^0$. For this type of decay the neutron might not be detected, so that the observed signal would be mimicking the $K_L \to \pi^0 \nu\bar{\nu}$ signal. This background was partially suppressed by going to an 8 *mrad* angle of incidence of the beam, mainly due to the fact that the production of Λ^0 decreases faster as a function of angle than in the case for the K_L. The Λ^0 momentum spectrum also drops faster at higher angles. Because of the long lifetime of the K_L relative to the Λ^0, this greatly reduces the number of Λ^0 that decay in the fiducial volume. Figure 8.1 shows the ratio of particles surviving over distance for an arbitrary 75 GeV/c momentum; this shows that Λ^0s decay much faster than K_Ls.
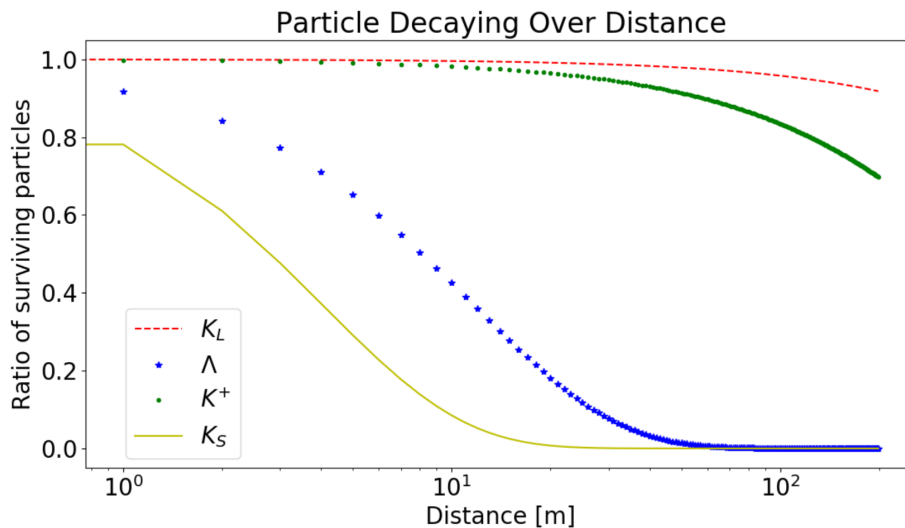
Figure 8.1: Different type of particles decaying in vacuum over distance at 75 GeV/c.

The KLEVER K12 beam line, see Figure 8.2, is composed of dipole magnets, mainly used to sweep away particles that can generate background, and collimators. A magnet is placed directly after the target that sweeps the primary protons, and dumps them on the combined dump/collimator (TAX). The neutral beam is mainly produced forward from
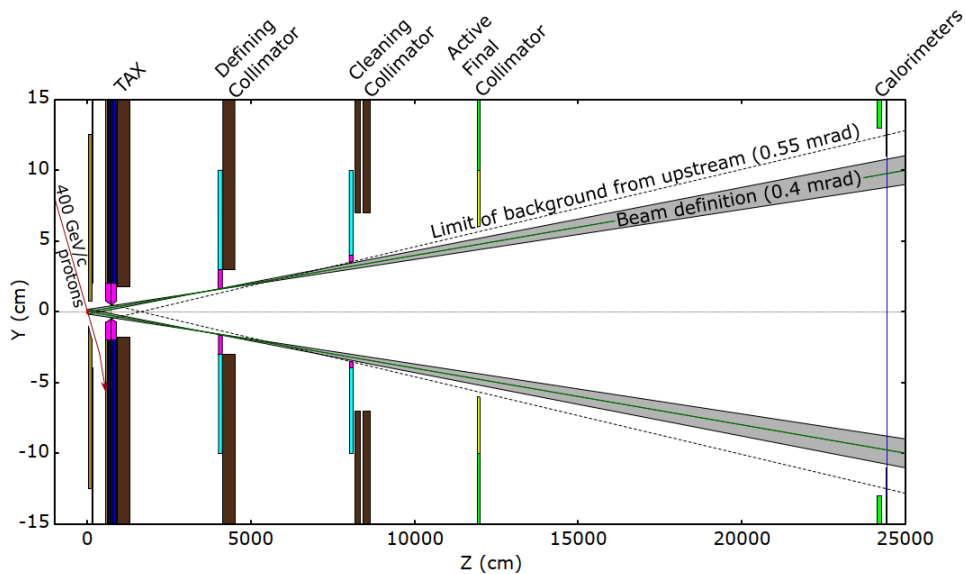
Figure 8.2: KLEVER beam line and detector designed in FLUKA [67].

the target and passes through the TAX collimator, see Chapter 2. After the TAX the beam encounters the defining and cleaning collimators, the apertures and materials of which have been defined using the skin depth values defined in Chapter 6. The defining collimator is the narrowest one and is followed by the cleaning collimator that removes particles generated by interactions on the defining collimator. These collimators define a full acceptance of 0.4 mrad opening angle relative to the target. Over the distance between the target and the detectors, significant quantities of muons are generated mostly from decays of pions and kaons. These can form substantial backgrounds in the detector, and a series of simulations has been performed in FLUKA [80, 81] to quantify those and then find strategies for their rejection. The field setting of the magnet following the target is maximised and fixed to dump the primary protons with as much downward angle as possible. The magnets following the collimator stations can be set in strength and orientation as needed. The detector of the KLEVER experiment was described in more detail in Chapter 4.

8.3 Background suppression for KLEVER

Recent studies showed that the contribution to the surviving background from the Λ^0s was initially underestimated and that some adjustments to the initial design of K12 are required. A reduction of the flux of Λ^0s could be achieved following two strategies: have

a larger incidence angle of the beam (currently set at 8 mrad) in order to have fewer Λ^0s produced on target that enter the K12 beam line; or have a longer K12 beam line that would let the Λ^0s decay before the K_Ls (since the K_Ls have a longer lifetime). The first method could be an easier solution but would imply also a lower flux of K_Ls as is shown in next section. The second method would require a full rearrangement of the beam lines and the cavern where the experiment is placed.

8.3.1 T10 target studies

Currently the 8 mrad incidence angle is achieved in KLEVER with a modification of the last three bending magnets of the P42 beam line in use for the NA62 configuration (two MBN magnets and one MCW). This can be achieved with the substitution of the MCW magnet with an MTR and changing the currents of these magnets as shown in Reference [116]. The values of currents are also displayed in Table 8.1.
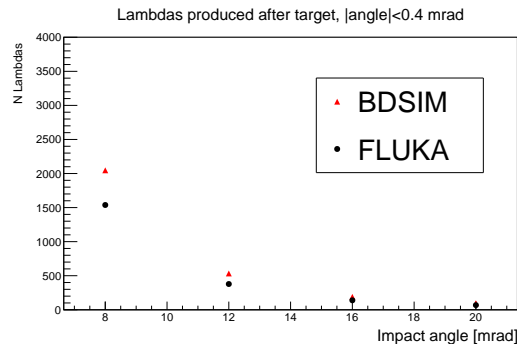
Figure 8.3: Number of Λ^0s as a function of the angle produced on the T10 target for the KLEVER configuration. Only Λ^0s within the K12 acceptance, $|angle| < 4$ mrad, are included.
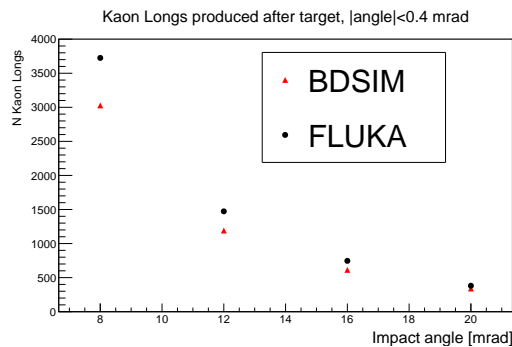
Figure 8.4: Number of K_Ls as a function of the angle produced on the T10 target for the KLEVER configuration. Only Λ^0s within the K12 acceptance, $|angle| < 4$ mrad, are included.

Table 8.1: Currents for the last three bending magnets in the present NA62 configuration and possible future KLEVER configuration.

Magnet	Bending Strength ($T \times m$)	KLEVER Current (Ampere)	NA62 Current (Ampere)
MBN	6.4	879.6	1339.6
MBN	8.9	1466.3	1117.4
MTR	7.3	815.1	-

Changing the 8 mrad angle poses some constraints on the magnets presently envisaged for KLEVER. These are indeed set to very high currents already for the 8 mrad configuration, given the bending strength limitations of these normal conducting magnets. Achieving higher values of the bending angle might be possible but would require new magnet types. Some preliminary studies have been carried out, in order to evaluate the number of particles produced on target assuming that an angle higher than 8 $mrad$ can be achieved. The target used is the T10 target presently used in NA62 (40 cm long and 2 mm in diameter). The incidence angles considered span from 8 to 20 mrad. The
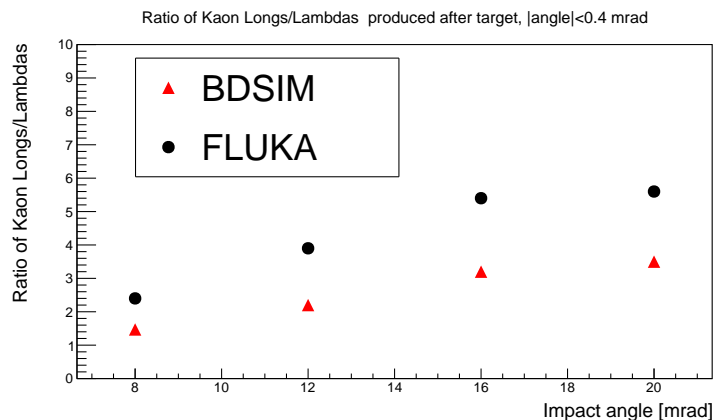
Figure 8.5: K_L/Λ^0 ratio as function of the proton impact angle on the T10 target for the KLEVER configuration.

simulations were run using FLUKA and BDSIM. The BDSIM simulations use the version GEANT4.10.06 and the $FTFP\_BERT$ physics list. The FLUKA version used is 4-0.1 with FLAIR 3.1-2 with a DEFAULTS card set to PRECISIO, without further cuts and using the standard FLUKA physics. The simulations were run using 10^8 protons on target and no low energy cuts. The number of particles within the KLEVER acceptance, hence a solid angle of 0.4 mrad, produced on target are shown in Figure 8.3 and Figure 8.4. The figures show that the change of angle is effective in reducing the ratio of Λ^0s over K_Ls (see Figure 8.5) but at the same time represents a problem in the reduction of the K_L intensity. The intensity of K_Ls is indeed decreased by a factor 2 when going from 8 to 12

mrad. Keeping a high intensity is a crucial factor for the KLEVER experiment therefore this solution is possible only if a higher intensity of protons on target can be reached for K12.

8.3.2 Relocation of the T10 target and K12 beam line

The second solution consists of extending the length of the K12 beam line in order to give more space for the Λ^0s to decay. This could be done moving the T10 target with consequent adaptation of the P42 beam line and displacement of the K12 beam line. The P42 beam line is currently passing through the TDC8 and TDC85 tunnel while the T10 target is installed in the TCC8 beam line and the NA62 detector in ECN3, see Figure 8.6. An extension of the K12 beam line could be achieved by re-positioning the T10 target in the TDC8 cavern or the TDC85, see blue indicators in Figure 8.6. After some preliminary considerations, the selected position was TDC8. This is preferred since this location contains more shielding (concrete and iron walls) that would surround the T10 target. Radiation studies on this location were done using a simple model of the target followed
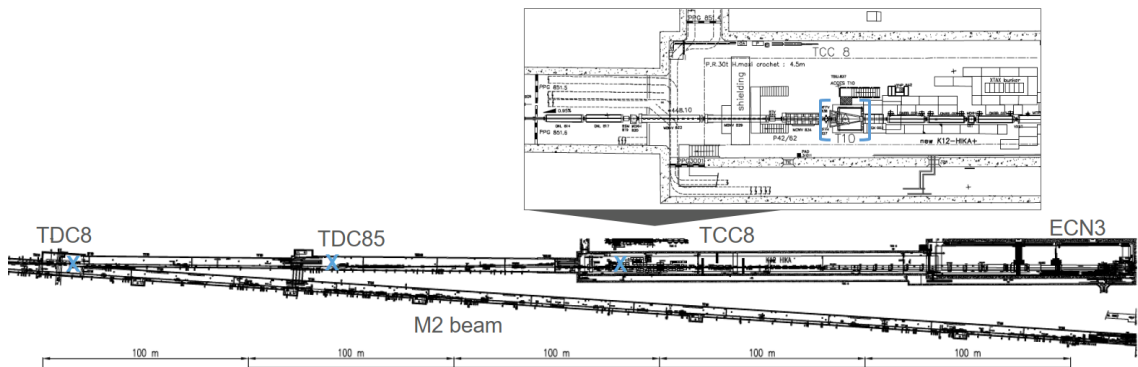
Figure 8.6: Areas where the NA62 experiment is currently located, ECN3 and the K12 beam line, TCC8. The potential positions of the KLEVER target are indicated in blue.

by the first sweeping magnets and the TAX, see Figure 8.7. The field maps were attached to the magnets using a routine written ad-hoc similar to the one used in Chapter 7. A simple concrete shielding was added around these representing the structure of the TDC8 tunnel. This can be seen in Figure 8.8. Radiation studies were conducted using this model and running them on the CERN Radiation Protection cluster [117]. The simulation was carried out using 2×10^{13} protons on target every 16.8 s. The results of such a simulation are shown in Figure 8.9; the red line around the radiation area represents the hard limit of 2.5 μSv/h that is currently set in the North Area by the Radiation Protection group.

It can be seen that this limit is exceeded especially in the region close to the target head. First estimations show that a layer of soil above the TDC8 tunnel of approximately 5 meters and a large layer of material around the target station (such as marble, iron or concrete) could reduce the radiation dose and bring it down to the required 2.5 μSv/h.
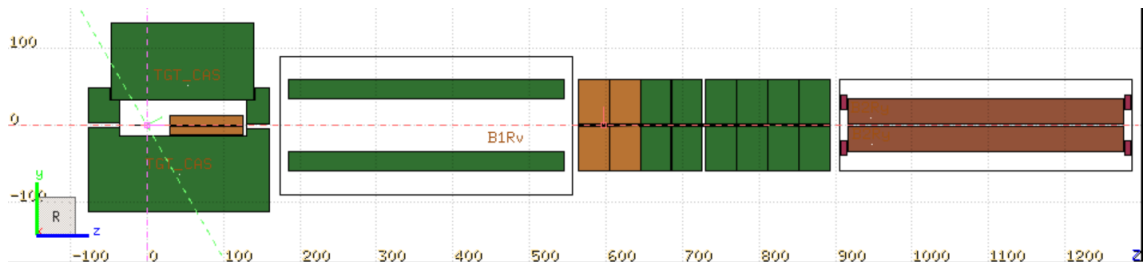
Figure 8.7: Layout drawing in FLUKA of the of the first portion of the K12 beam line for KLEVER used for the radiation protection studies.
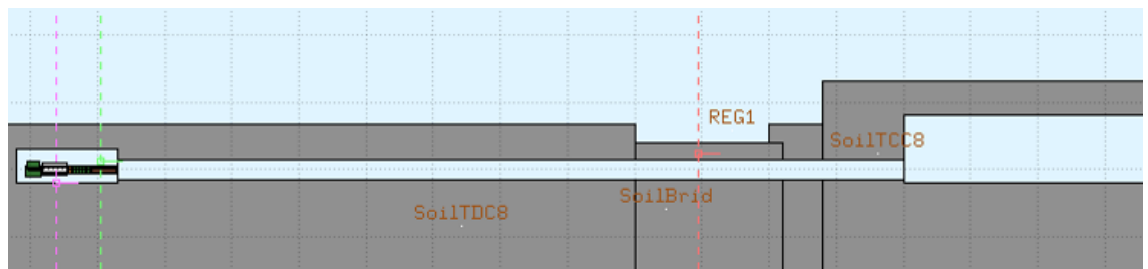
Figure 8.8: K12 beam line in the experimental hall for KLEVER used for the radiation protection studies and shielding.
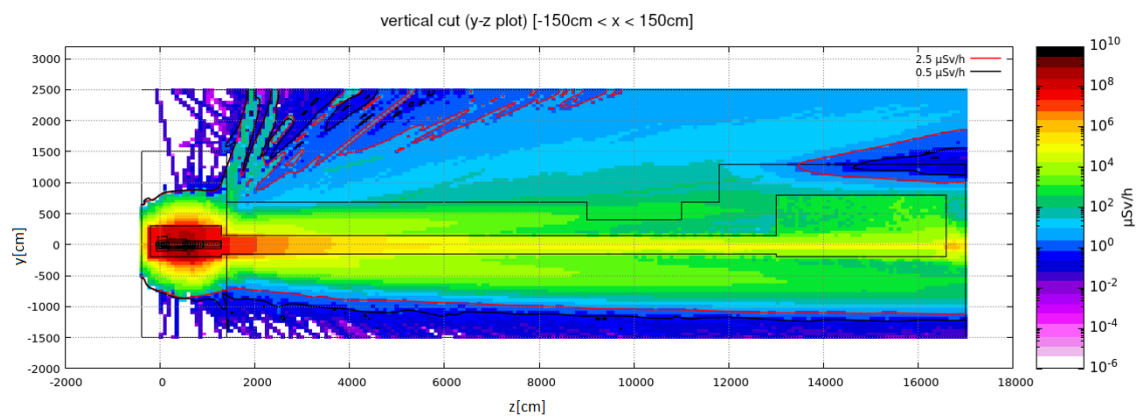
Figure 8.9: K12 beam line in the experimental hall for KLEVER used for radiation studies in FLUKA and relative generated radiation.

This modification would be quite expensive and modify the tunnel shape fundamentally. For this reason another alternative is also taken into account and currently considered the most feasible; this consists of the extension of the ECN3 cavern. This

cavern contains already a large amount of shielding material and a thick layer of soil on top of it. In this configuration the T10 target would not need to be moved and most of the K12 beam line would remain unchanged (horizontal) and translated further downstream in the ECN3 cavern.

8.4 T4 bypass studies for KLEVER and NA62-HI

The KLEVER experiment would require a high intensity of protons on target (2×10^{13} protons per 4.8 s spill), more than six times higher than NA62 operates at (3×10^{12} protons per 4.8 s spill). NA62 itself would need significant modifications to withstand a higher proton rate (comparable to the KLEVER one). In this configuration, NA62 is called NA62-High-Intensity (NA62-HI or NA62×4). With the current settings of the beam lines serving the experiments (TT24 and P42) these intensities cannot be achieved. This is mainly due to the fact that the proton beam impinging on the T4 target undergoes a significant attenuation [3]. The TT24 and P42 beam lines need some optics adjustments that cause fewer interacting particles on the T4 target avoiding the aforementioned reduction. This implementation, called target bypass, is discussed in the next sections. These studies are performed using MADX [78] and AppLE.py [77].

8.4.1 TT24 parameters

The beam lines involved in these studies are TT24 and P42 [103]. The T4 target is 2 mm thick and contains several beryllium plates adjustable for a total length that can range between 40 to 500 mm. In order to bypass T4, the vertical beam size at the end of TT24 can be increased to only partly collide with the T4 target and afterwards re-focused in order to fit within the magnet apertures of P42. The goal is to reach such a beam-size that only approximately 10% of the beam interacts with the T4 target, while the remaining beam would bypass it vertically, see Fig. 8.10, and escape unattenuated.

Figure 8.10: Schematic side view of proton beam being defocused before T4 target and partially interacting with it [118].

The beam parameters at the end of the TT24 beam line can be calculated in MADX. It is possible to calculate the current parameters (used for the standard NA62 configuration) and the ones needed for a future experiment such as KLEVER or NA62-HI. The comparison of these values can be seen in Table 8.2. These values refer to the beam size σ in X and Y, the normalised emittance ϵ in X and Y, and the β functions in X and

Y. These quantities are all related by Equation 8.1, valid for a Gaussian beam with zero dispersion.

Table 8.2: Simulated beam parameters for the standard (current) and new configuration at the T4 target (end of TT24 beam line).

Parameters	Standard Configuration	New Configuration
$\sigma_x [mm]$	0.5	0.5
$\sigma_y [mm]$	0.4	4
$\epsilon_x [mm \times mrad]$	2	2
$\epsilon_y [mm \times mrad]$	0.1	0.1
$\beta_x [m]$	58	58
$\beta_y [m]$	740	74000

The parameters obtained from the MADX studies on TT24 can be used as input for the P42 beam line.

$$\sigma = \sqrt{\epsilon \beta} \tag{8.1}$$

Assuming that the particle position and angle are uncorrelated at the location of the target the divergence of the beam can be calculated at various points using Equation 8.2.

$$\epsilon = \sigma_x \sigma_{x'} \tag{8.2}$$

8.4.2 Beam size optimisation studies in P42

The beam size in the P42 beam line has to be kept within apertures of the magnets in order to avoid damage via beam interactions or background generation for the experiment. The propagation of the beam through P42 has been studied for the current beam optics settings of TT24 and P42, currently in use for NA62. For this purpose a complete model of P42 model was created in MADX. The information on the magnets current and size is specified in the CERN database. The analysis of P42 can be developed to study the beam size in X and Y. The plots showing these results are shown in Fig. 8.11. This plot shows that in the current beam lines configuration the beam size is approximately a few millimetres. The smallest aperture in P42 is the QNL quadrupole that has a diameter of 8 cm. In this case the beam is small enough to pass within this aperture without interaction. For the T4 bypass a much higher beam size is expected, therefore the magnetic configuration of P42 needs to be changed. In particular, it was chosen to adjust the focusing strength of the first five quadrupoles to keep the beam size within the aperture limits all along the P42 beam line and small enough to collide with the T10 target (2 mm in diameter). The new
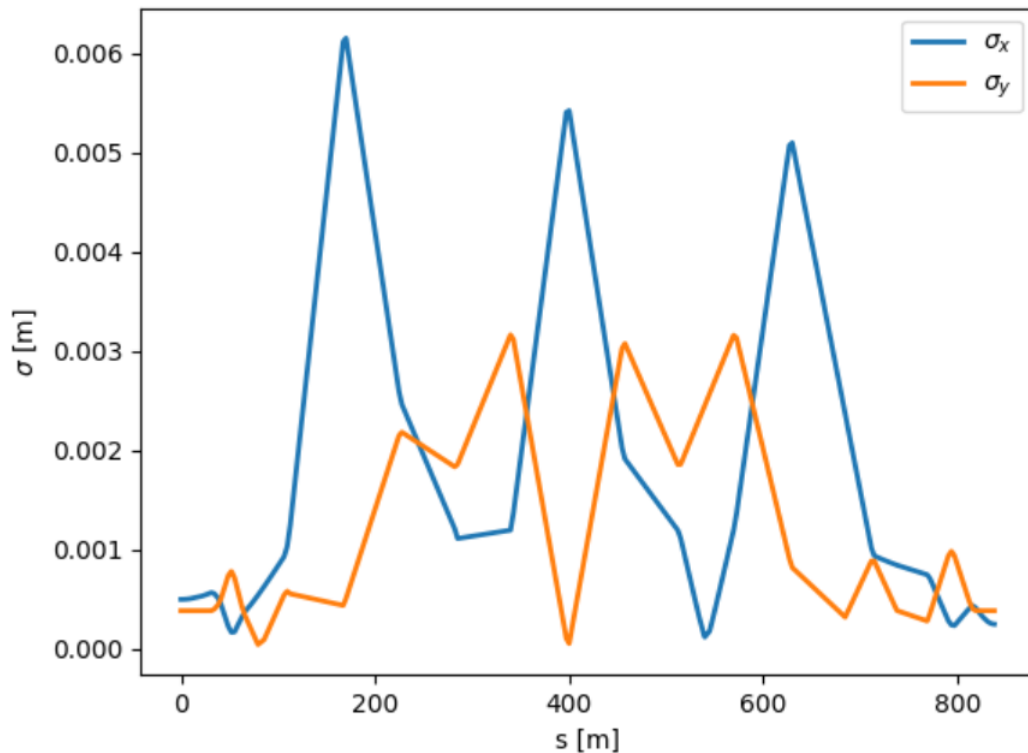
Figure 8.11: Beam size (one standard deviation) as a function of s (reference particle position along the beam) along P42 in the current configuration of the TT24 beam line.

focusing strength values for the five quadrupoles are obtained in MADX using as a limit the maximum achievable gradient of the quadrupoles (taken from the CERN database) and requiring a beam size in the same range of the standard configuration. In practice this is achieved using the fitting routine available in the MADX software. The values for the two different configurations for the focusing strength of the first five quadrupoles resulting from the fitting routine can be seen in Table 8.3.

Table 8.3: Field strength of the quadrupoles in P42 before and after fitting procedure in MADX. The quadrupoles are numbered according to their appearance in the P42 beam line and $k1$ is the focusing strength in m^{-2}.

Parameters	Standard Configuration	New Configuration
$Q1 - k1\ [m^{-2}]$	0.009482	-0.005511
$Q2 - k1\ [m^{-2}]$	0.014060	0.0117363
$Q3 - k1\ [m^{-2}]$	-0.015110	-0.009590
$Q3A - k1\ [m^{-2}]$	-0.015110	-0.009590
$Q4 - k1\ [m^{-2}]$	0.014060	0.011736

The values of the beam size for the new configuration can be seen in Fig. 8.12. The values obtained following this procedure are acceptable and prove that a beam size in the
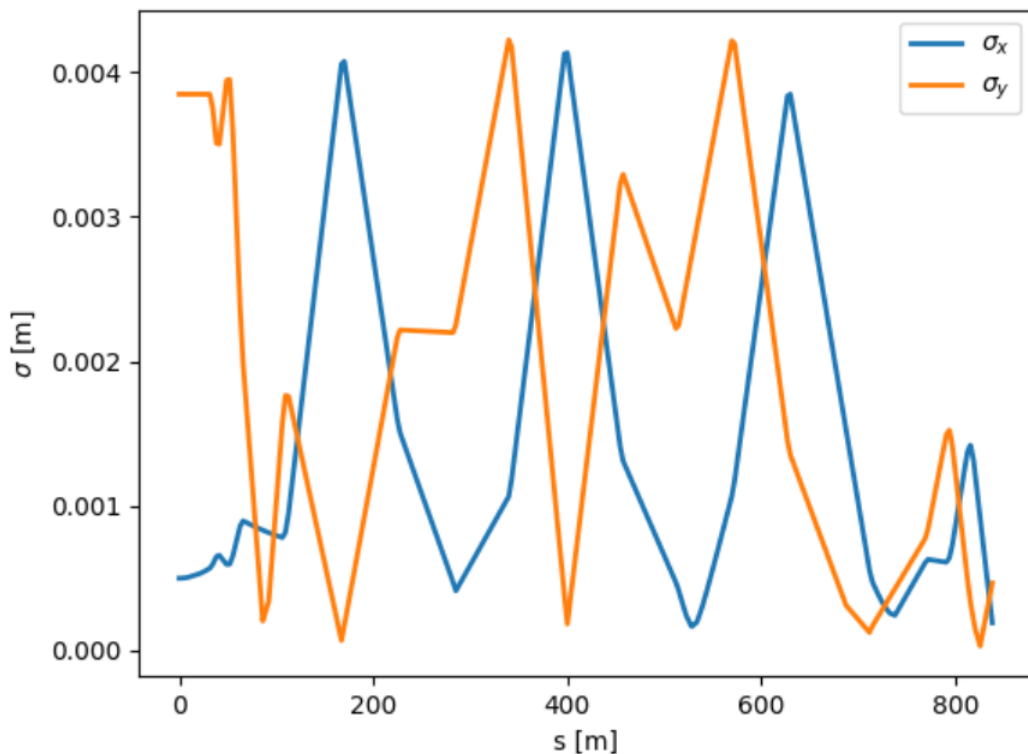
Figure 8.12: Beam size (one standard deviation) as a function of s (reference particle position along the beam) along the P42 beam line in a possible new configuration with the TT24 beam line adapted to KLEVER and NA62-HI.

millimeter range can be achieved with the polarity inversion of the first quadrupole of P42 and some minor modification for the focusing strength of the other magnets. These first results prove the feasibility of the T4 bypass in terms of beam size tolerance.

8.4.3 Beam tracking in P42

The configuration proposed for P42 in the KLEVER and NA62-HI mode is further examined with tracking studies. These studies have been developed using the AppLE.py code, see Chapter 5. It is reminded here that this code uses MADX-PTC internally for tracking purposes but gives the possibility of using an interactive graphical user interface (GUI) in order to modify the desired initial beam parameters. Using the new configuration parameters from Table 8.2 and assuming $\frac{dp}{p} = 0.001$ (estimated for the proton primary beam in TT24) the tracking can be done in AppLE.py. In particular it is noticed in Figure 8.13 that particles all fit in the magnet apertures, that are highlighted in light-blue as opposed to the magnet yoke that is in dark-blue. This is an additional proof that in the configuration found for the T4 bypass, the particles would not hit the magnets aperture allowing

therefore to run in this mode.
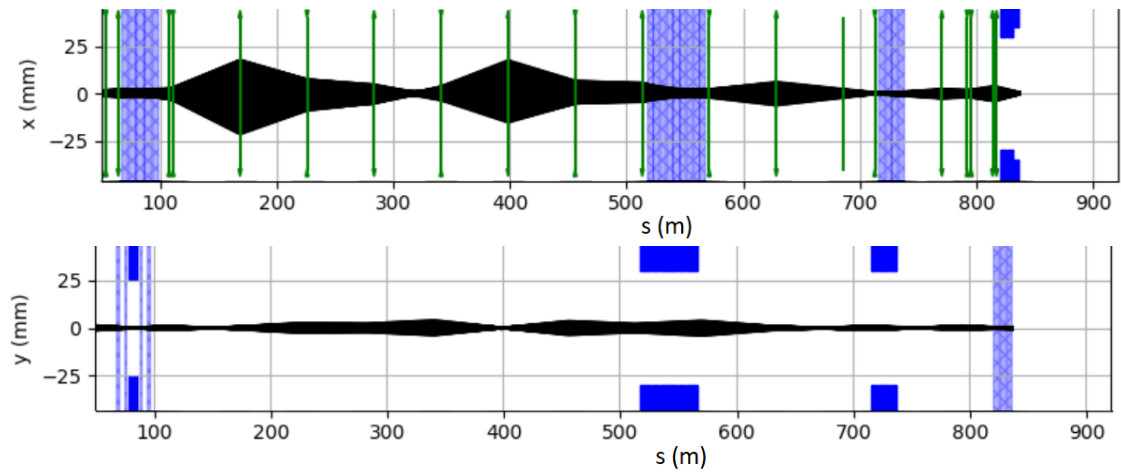
Figure 8.13: Tracking of particles in AppLE.py along the P42 beam line. Particle tracks are represented with black lines. Dipoles are represented in dark blue and their apertures are in light blue. Quadrupoles are represented as green arrows that extend through their apertures.

8.5 Muon background studies for NA62-BD

The aim of the studies for NA62-BD in this section is to understand the muon background generated in the experiment. The approach followed for this purpose is very similar to the one followed for the standard NA62 configuration. In order to do so, a BDSIM model of NA62 in dump configuration is created. The NA62-BD configuration is very similar to the configuration of NA62 with some minor changes. In NA62-BD mode the T10 target is removed from the beam axis, therefore the protons do not interact with it directly and are all transported via the K12 onto the TAX instead. The TAX is in this case used in dump mode; this means that the two collimator layers are shifted such as to completely absorb the incoming beam (see Figure 8.14, more details on the TAX can be found in Chapter 4). These modifications are implemented in the present BDSIM configuration of the beam line described in Chapter 7.
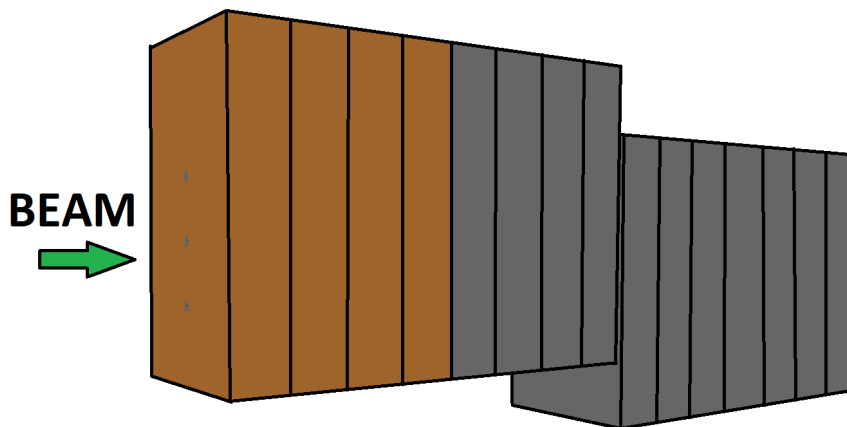
Figure 8.14: TAX geometry visualised in BDSIM for the Beam-Dump Configuration

For these simulations BDSIM is used as an event generator and the events are afterwards propagated through the NA62MC model built by the NA62 Monte Carlo group. The NA62 collaboration performed a data acquisition run in BD mode in 2018, in Run 2, and collected data for a period of approximately one month. These data are provided by the NA62 collaboration in order to compare with the BDSIM+NA62MC simulation (called BDSIM in the rest of this section). In the simulation the muon distribution is reconstructed at approximately 180 m from the target, at the location of the CHOD detector, see Chapter 4. In order to reach adequate statistics a biasing technique is developed

to reach a more abundant muon sample; this is described in detail in Reference [119]. The plots for the distributions at 180 m from the target are shown in Figures 8.15, 8.16, 8.17 and 8.18. These are created using the $FTFP\_BERT$ physics list. Both data and MC are downscaled by a factor five (data is like this by trigger construction, and the MC statistics is divided by 5 to account for this). The MC sample contains only muons originating from primary protons interacting in the TAX. The component coming from proton interactions upstream of the TAX is missing. This is the reason why the plot for the positive muons is showing a discrepancy with respect to data in shape around p=75 GeV/c.
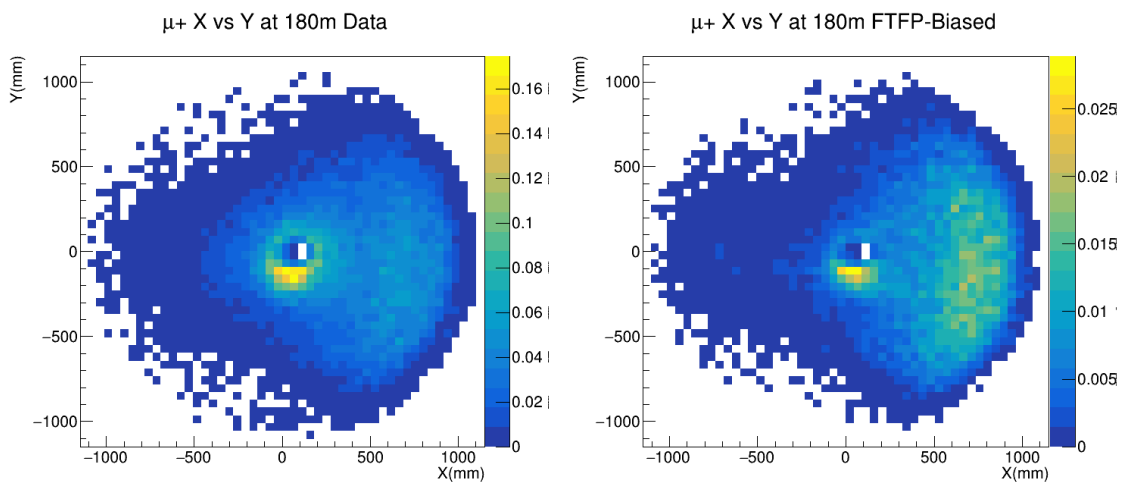
Figure 8.15: X-Y distribution of positive muons at a plane located 180 m from the target of K12. The data from 2018 data taking of NA62-BD are shown on the left, on the right the simulation in BDSIM is displayed.
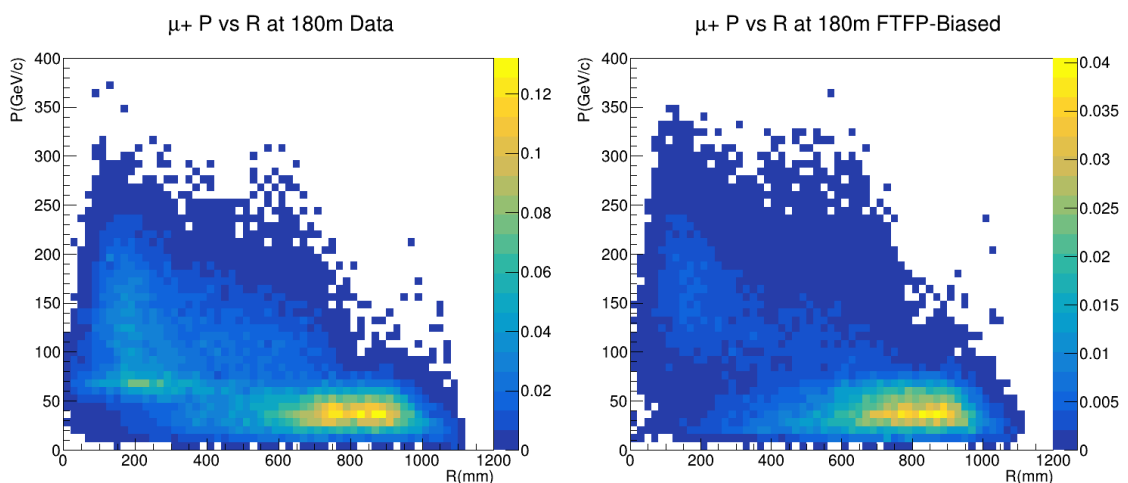
Figure 8.16: Distribution of positive muons in momentum versus radius at a plane located 180 m from the target of K12. The data from 2018 data taking of NA62-BD are shown on the left, on the right the simulation in BDSIM is displayed.
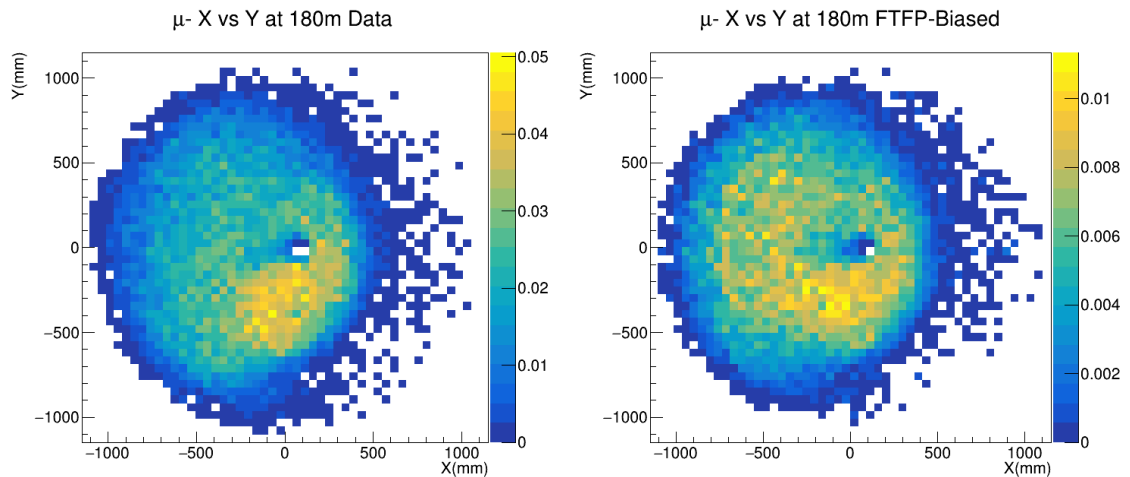
Figure 8.17: X-Y distribution of negative muons at a plane located at 180 m from the target of K12. The data from 2018 data taking of NA62-BD are shown on the left, on the right the simulation in BDSIM is displayed.
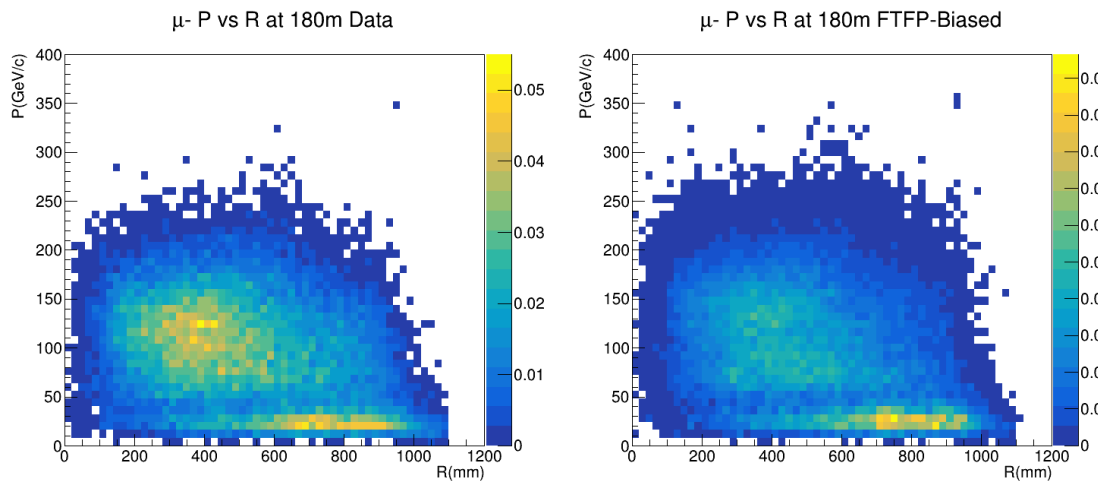
Figure 8.18: Distribution of negative muons in momentum versus radius at a plane located at 180 m from the target of K12. The data from 2018 data taking of NA62-BD are shown on the left, on the right the simulation in BDSIM is displayed.

The plots demonstrate that the overall muon distributions are well reproduced by the BDSIM software. Some differences can be observed in the rates and the plane illuminated regions. More studies are ongoing in collaboration with the NA62-BD group in order to improve the agreement between MC and data. A particular use of these studies is the use of different physics lists as well as the use of a new optimised field map for the muon sweeping system (mainly the MBPL magnets) in the BDSIM model.

This is the first attempt to characterise the background for NA62-BD in BDSIM. The agreement reached between data and simulations is the most precise achieved so far with

Monte Carlo simulations. More studies have been carried out following this first benchmark aiming to find the best configuration for minimising the background generated in the NA62-BD experiment and are presented in Reference [120].

8.6 SHADOWS

The studies for the SHADOWS experiment are also focused on the muon background. SHADOWS is a parasitic experiment therefore no changes in the K12 beam line are required for the BDSIM model. The SHADOWS detector is located at about 40 m from the T10 target right after the first achromat in K12. Previous studies showed that in the parasitic run the muon rates at SHADOWS could be too high (20 MHz) to allow sensitive dark matter measurements. For this reason a main priority for the experiment is to lower these rates. This cannot be achieved by simply changing the magnetic configuration of the beam line as was shown in Reference [120]; a new solution for this purpose is therefore required. The method followed in this section is to introduce a muon sweeping system that is dedicated to optimise the background for SHADOWS. In the simplest form this muon sweeping system could consist of an additional off-axis bending magnet upstream of the SHADOWS detector, located after the first achromat magnets in order to minimise the fraction of muons that are swept into the SHADOWS acceptance. The sweeping magnet used in these simulations is a different version of the so-called "scraper" magnet (depicted in Figure 8.19), similar to a magnetised iron block, currently used in the COMPASS experiment. Following previous studies of the NA62-BD background minimisation, the same magnetic configuration (see Reference [120]) is used for the simulations of SHADOWS done in this section. In this configuration almost all the magnetic elements of K12 are switched off leaving two bending magnets of the first achromat active and set to a field of 1.8 T.
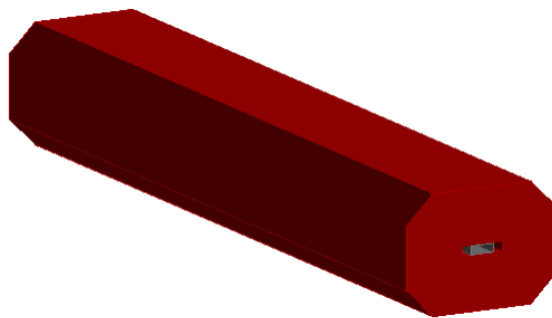
Figure 8.19: Scraper magnet used as a sweeper in the SHADOWS model.

The discussion in the rest of this section is built upon the transverse X-Y muon flux at the foreseen location of the SHADOWS experiment. All together with the detector, the sweeping magnet is also inserted at a location near the last bending magnet of the last

achromat. For this purpose it is necessary to adjust the shielding that surrounds this area. A picture of the current shielding can be seen in Figure 8.20. The magnet itself (made of iron) has a certain stopping power and reduces the muon flux, working effectively as a shielding block. The simulations of the muon background generated in the SHADOWS

Figure 8.20: Shielding in the region after the first achromat in the current NA62 configuration.

detector for the configuration without sweeping magnet can be seen in Figure 8.21. The BDSIM version used is GEANT4.10.06 and the $FTFP\_BERT$ physics list. The figure shows that in the X-direction the muon distributions are approximately symmetric in respect to the centre of the beam line. In the Y-direction the magnetic field of the bending magnets in the first achromat separates the positively charged from the negatively charged muons. The return yokes of the MTR magnet also give the muons a momentum in X-direction pushing them into the SHADOWS acceptance. From inspecting these pictures it becomes evident that a muon sweeping system is necessary. The dimensions of the sweeping magnet were established after a few iterations that finally led to choose a magnet of 3.0×3.1 m in the transverse plane and 6 m long. Considering a magnetic field peak of 1.7 T in the center of the magnet this corresponds to a total BL =10.2 Tm. Such a large magnet in the transverse plane allows to maximise the muons that are swept away near the

141
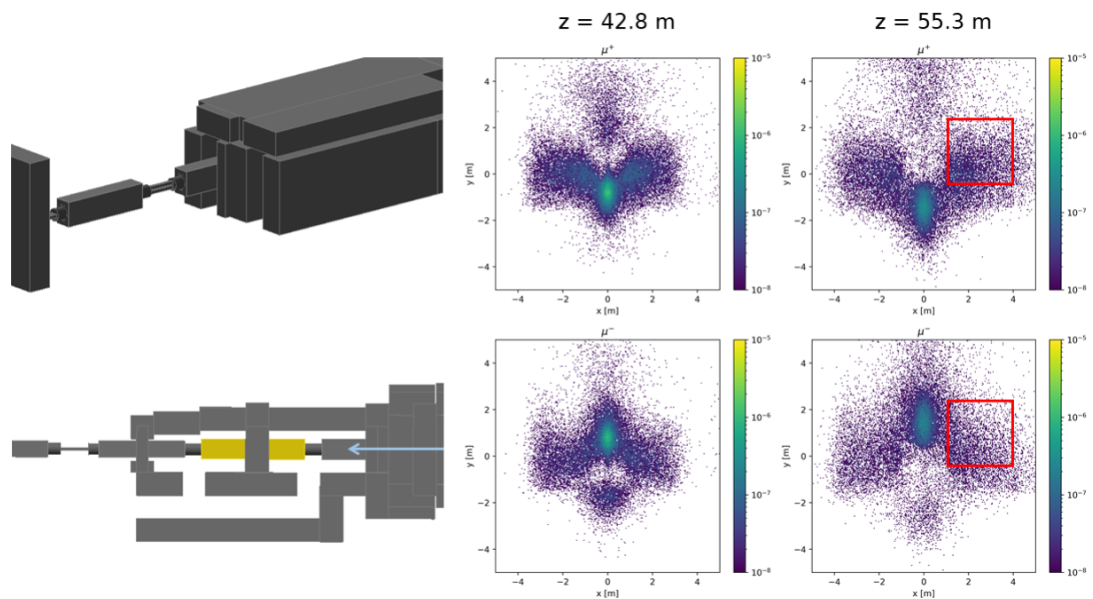
Figure 8.21: Left: BDSIM model of the current configuration for the NA62 experiment after the first achromat. Right: muon flux in this configuration at two planes (z=42.8 m and z=55.3 m) for μ^+ and μ^-, the red box indicates the region of the SHADOWS detector.

yoke. The muons are redirected in this manner in the X-direction and miss the SHADOWS detector. The results obtained for this configuration are displayed in Figure 8.22. The plots show that for this configuration the muon background could be reduced drastically. Compared to the original setup shown in Figure 8.21 the number of muons in the relevant SHADOWS detector region is reduced by a factor seven in the relevant SHADOWS region. Furthermore, by investigating the charge of the muons, as it is displayed in Figure 8.21, it is possible to see that the tested muon sweeping system is able to reduce the positive muons more than the negative muons. In fact, the background generated by positive muons would decrease by approximately a factor 20, while the negative muons background is reduced by a factor four, compared to the simulation without sweeping system. This asymmetry effect is due to the polarity of the magnet. For the alternative polarity, the opposite behaviour would have been observed. Another feature of the sweeping system is that while the positive muons are swept away from the SHADOWS detector, the negative muons are conducted into the direction of the return yoke of the magnet. The return yoke forces the negatively charged muons to the centre of the magnet. These muons are therefore being forced to move forward at small angles from the sweeper and could eventually reach the SHADOWS detector. Even if this behaviour occurs, the separation of negative and positive muons might not be an issue, but could actually simplify the muon sweeping. It
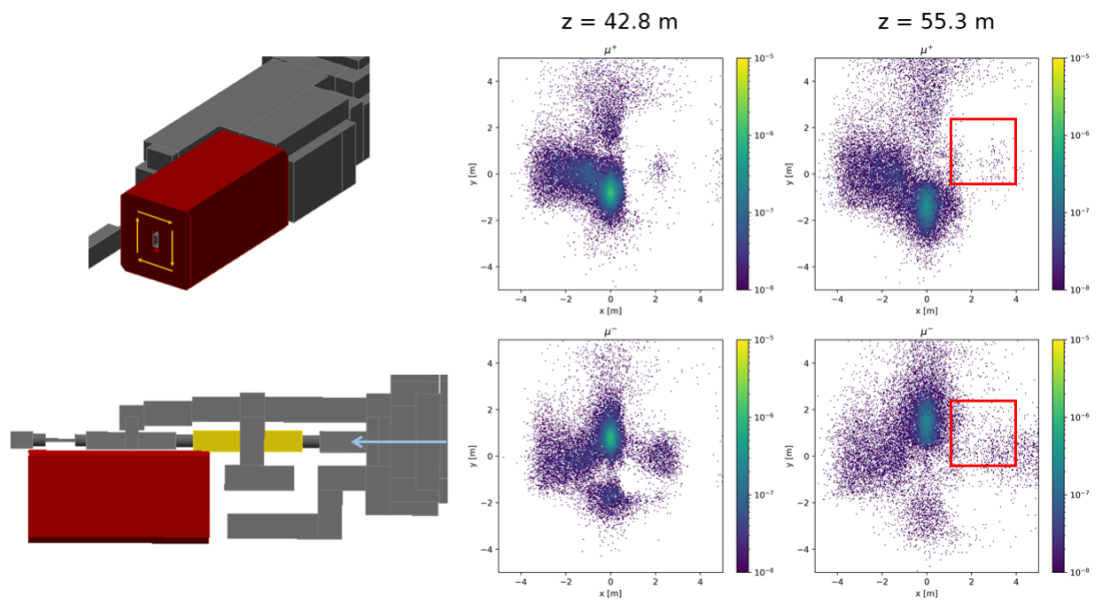
Figure 8.22: Left: BDSIM model of potential new configuration for the SHADOWS experiment after the first achromat. Right: muon flux in this configuration at two planes (z=42.8 m and z=55.3 m) for μ^+ and μ^-, the red box indicates the region of the SHADOWS detector.

is possible indeed to place two separate sweepers instead of a single one and redirect the two components separately. By doing so it might be possible to reduce the size of the single sweeping magnet and to avoid having a strong effect given by the return field in the yoke [121].

8.7 Results Summary

This chapter summarises the beam and background studies done for the P42 and K12 beam lines for possible future configurations. Simulations in BDSIM and FLUKA are carried out for the KLEVER configuration in order to study the background produced by Λ^0s. It is shown how this flux can be reduced preferably adopting new positioning for the T10 target or extending the ECN3 cavern. It is also demonstrated how, thanks to the T4 target bypass, it is possible to achieve a higher intensity for KLEVER and the NA62-HI configuration. This new solution is currently considered for future implementation and will be tested during Run 3 of the LHC. A full model of NA62-BD is created and benchmarked to data from the NA62 collaboration, showing a good compatibility of the BDSIM model with the data collected in 2018. The same model is used for studies of the background in the SHADOWS experiment that proved the possible reduction of the muon flux at the detector plane.

Chapter 9

Summary and Outlook

This final chapter of the thesis summarises the results and the methods developed in the document. The main goal of the thesis work is to address the feasibility and optimisation of experiments at the P42 and K12 beam lines. A large share of the studies is dedicated to background studies and beam line optimisation. It is shown in Chapter 6 how the "skin depth" parameter is defined, for the first time, for secondary beam lines. This is used, and will be used in future, for collimation at experiments such as KLEVER and NA62. Chapter 7 addresses potential backgrounds generated in K12 for the NA62 configuration. It is here shown that BDSIM, FLUKA and MADX are useful tools for this kind of studies. The beam-size, the divergence given by the CEDAR gas, the background coming from muon halo and particle interactions with the residual gas of NA62 are studied and characterised for K12. In particular, the studies of the CEDAR (also called KTAG) show that the hydrogen gas can be used as an alternative to nitrogen, bringing a potential background reduction for the experiment. These studies are taken into account by the NA62 collaboration that will use in 2023 a version of the CEDAR detector with hydrogen. The BDSIM model of K12 is currently adopted by the NA62 collaboration as generator for Monte Carlo simulations and is used to describe the muon backgrounds in the experiment. The FLUKA model developed for this thesis work is currently used by the Radiation Protection group at CERN. The same model served to prove that the beam gas generated background for NA62 is negligible for the considered $K^+N \to K_s \to \pi^+\pi^-$ channel.

The studies for future experiments are presented in Chapter 8. It is shown how the background for KLEVER can be reduced preferably adopting new positioning for the T10 target or extending the ECN3 cavern. It is also demonstrated how, thanks to the T4

target bypass, it is possible to achieve a higher intensity for KLEVER and the NA62-HI configuration of NA62. This new solution is currently being considered for future implementation and will be tested during Run 3 of the LHC. Finally, a full model of NA62-BD is created and benchmarked to data from the NA62 collaboration, showing a good compatibility of the BDSIM model with data. The same model is used for studies of the background in the SHADOWS experiment that proved the possible reduction of the muon flux at the detector plane.

These studies play an important role with the BE-EA-LE section and the experiments mentioned in this thesis. The results and models developed so far are currently used and being extended within the section, covering new aspects and future implementation of experiments at P42 and K12.

Appendix A

Appendix

This appendix gives an overview of the studies done for two secondary beam lines (T9 and T10) in the East Area using BDSIM. The beam line configuration used in this section corresponds to what was used in the East Area before renovation (in 2018).

A.1 BDSIM studies for secondary beam lines: T9 and T10

The T9 and T10 beam lines are located in the CERN East Area and were used to provide (in the 2018 configuration) secondary beams of charged particles in a momentum range from 1 GeV/c up to 10 GeV/c (for the T9 beam line) and up to 6 GeV/c (T10 beam line), produced due to the interaction of a primary 24 GeV/c proton beam with a target head. T9 was used for several experiments while T10 was mainly dedicated to ALICE [122].
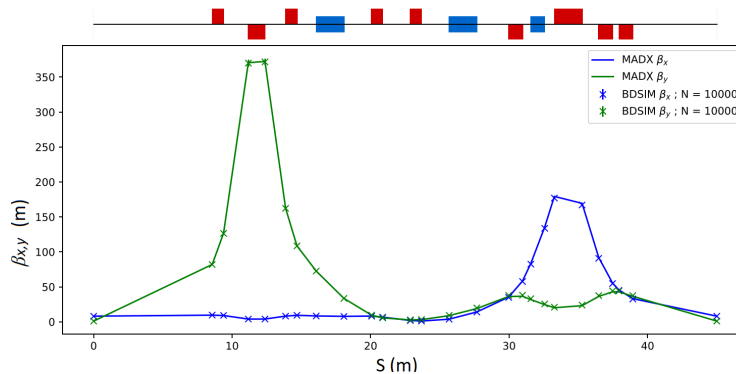
Figure A.1: CERN T10 beamline optics comparions between BDSIM and MADX

In this section the optics studies for T10 and the particle production spectra for T9 are presented. The simulations are run using BDSIM version 1.4 with GEANT4.10.4.p03. Figure A.1 shows the T10 optics (beta functions in X and Y) obtained from simulations

run for 10000 particles. It can be noticed in the figure a good agreement between BDSIM and MADX within the relative error bars. For T9, studies of particle production have been run placing a target head upstream the beam line. The target used is 200 mm long and is
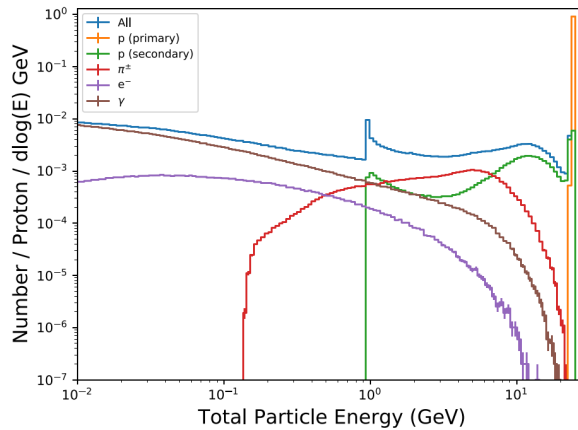
Figure A.2: Particle production spectra after the target of the T9 beamline.

made of beryllium. For the purpose of studying the beam composition, 10 million particles were simulated using a complete package of physics processes, $FTFP\_BERT$, available in BDSIM [123]. Figure A.2 shows the particles spectra after target simulated in BDSIM. The spectra have the expected rates for the considered energy and are comparable to those shown in Reference [37]. These are the first studies developed for CERN secondary beam lines with BDSIM and they show how the software can be reliably used for these type of energy ranges and beam line configuration.

Bibliography

[1] G. Lamanna. The NA62 experiment at CERN. *Journal of Physics: Conference Series*, Vol. 32, pages 1–3, 2011.

[2] N. Lurkin. Latest results from the NA62 experiment at CERN. *Proceedings, An Alpine LHC Physics Summit (ALPS 2019)*, pages 3–4, 2019.

[3] J. Beacham et al. Physics Beyond Colliders at CERN: Beyond the Standard Model Working Group Report. *CERN Document Server, CERN-PBC-REPORT-2018-007*, pages 4–12, 2018.

[4] F. Ambrosino et al. An experiment to measure $\mathrm{BR}(K_L \to \pi^0 \nu \bar{\nu})$ at the CERN SPS. *arXiv:1901.03099*, pages 1–4, 2019.

[5] L. Gatignon et al. Report from the Conventional Beams Working Group to the Physics beyond Colliider Study and to the European Strategy for Particle Physics. *CERN Document Server, CERN-PBC-REPORT-2018-002*, pages 1–81, 2018.

[6] M. Schwartz. *Quantum Field Theory and the Standard Model*. Cambridge University Press, 2014.

[7] A. De Angelis and M. Pimenta. *Introduction to Particle and Astroparticle Physics*. Springer, 2015.

[8] M. Robinson. *Symmetry and the Standard Model*. Cambridge University Press, 2011.

[9] A. Bettini. *Introduction to Elementary Particle Physics*. Cambridge University Press, 2008.

[10] J. Schwinger. The Theory of Quantized Fields. *Physical Review*, Vol. 82 (914), pages 914–927, 1951.

[11] N. Cabibbo. Unitary Symmetry and Leptonic Decays. *Physics Review Letters*, Vol. 10, pages 531–532,1963.

[12] M. Kobayashi and T. Maskawa. CP Violation in the Renormalizable Theory of Weak Interaction. *Progress of Theoretical Physics*, Vol. 49, pages 652–657, 1973.

[13] P.A. Zyla et al. Particle Data Group. *Progress of Theoretical and Experimental Physics*, Vol. 2020 (8), pages 1–2093, 2020.

[14] L. Leprince-Ringuet and M. L'Heritier. *Compt. Rend.*, Vol. 219 (618), 1944.

[15] T. Nakano and K. Nishijima. Charge Independence for V-particles. *Progress of Theoretical Physics*, Vol. 10 (5), pages 581–582, 1953.

[16] M. Gell-Mann. Isotopic Spin and New Unstable Particles. *Physical Review*, Vol. 833 (92), pages 833–834, 1953.

[17] G.D. Rochester and C.C. Butler. Evidence for the Existence of New Unstable Elementary Particles. *Nature*, Vol. 160, pages 855–857, 1947.

[18] M. Gell-Mann and A. Pais. Behavior of Neutral Particles under Charge Conjugation. *Physical Review*, Vol. 97, pages 1387–1389, 1955.

[19] S.Gjesdal et al. A measurement of the $K_L - K_S$ mass difference from the charge asymmetry in semi-leptonic kaon decays. *Physics Letters B*, Vol. 52 (1), pages 113–117, 1974.

[20] O. Piccioni and A. Pais. Note on the Decay and Absorption of the θ^0. *Physical Review*, Vol. 100, pages 1387–1389, 1955.

[21] J. Cronin and et al. Evidence for the 2π Decay of the K_2^0 Meson. *Physics Review Letters*, Vol. 13 (138), pages 138–140, 1964.

[22] V. Fanti et al. A new measurement of direct CP violation in two pion decays of the neutral kaon. *Physics Letters B*, Vol. 72 (465), pages 335–348, 1999.

[23] C. Hawthorn, K. Weber, and R. Scholten. Littrow Configuration Tunable External Cavity Diode Laser with Fixed Direction Output Beam. *Review of Scientific Instruments*, Vol. 72 (12), pages 4477–4479, 2001.

[24] L.G. Landsberg. Rare Kaon Decays $K^+ \rightarrow \pi^+ \nu \overline{\nu}$-2005: Standard Model and New Physics. *Physics of Atomic Nuclei*, Vol. 69, pages 757–759, 2005.

[25] E. Stamou. Rare Kaon Decays. *arXiv:1101.3245*, pages 1–7, pages 1–7, 2011.

[26] F. Zwicky. On the Masses of Nebulae and of Clusters of Nebulae. *The Astrophysical Journal*, Vol. 86, pages 217–220, 1937.

[27] V. Trimble. Existence and Nature of Dark Matter in the Universe. *Annual Review of Astronomy and Astrophysics*, Vol. 25, pages 425–472, 1987.

[28] S. Lowette. Accelerator searches for new physics in the context of dark matter. *Journal of Physics: Conference Series*, pages 1–2, Vol. 718 (2), pages 1–2, 2016.

[29] M. Fabbrichesi, E. Gabrielli, and G. Lanfranchi. The Dark Photon. *arXiv:2005.01515v3*, pages 1–2, 2020.

[30] J. Beacham et al. Physics Beyond Colliders at CERN: Beyond the Standard Model Working Group Report. *Journal of Physics G*, Vol. 47, pages 68–69, 2020.

[31] A. Abada and A.M. Teixeira. Heavy Neutral Leptons and High-Intensity Observables. *Frontiers in Physics*, pages 8–10, 2018.

[32] M. Ackermann et al. Dark matter constraints from observations of 25 Milky Way satellite galaxies with the Fermi Large Area Telescope. *Physical Review D*, Vol. 89 (4), pages 1–47, 2014.

[33] J. Grube et al. VERITAS limits on dark matter annihilation from dwarf galaxies. *AIP Conference Proceedings*, Vol. 1505 (689), pages 1–5, 2012.

[34] R. Land and W. Seidel. Search for dark matter with CRESST. *New Journal of Physics*, Vol. 11, pages 1–21, 2009.

[35] E. Behnke et al. First dark matter search results from a 4-kg CF3I bubble chamber operated in a deep underground site. *Physical Review D*, Vol. 86 (5), pages 1–8, 2012.

[36] M. Kamionkowski, K. Griest., G. Jungman, and B. Sadoulet. Model-Independent Comparison of Direct versus Indirect Detection of Supersymmetric Dark Matter. *Physics Review Letters*, Vol. 74, pages 1–9, 1995.

[37] H. Atherton et al. Precise measurements of particle production by 400 GeV/c protons on beryllium targets. *CERN Document Server, CERN-80-07*, pages 1–25, 1980.

[38] A. Malensek. Empirical formula for thick target particle production. *Fermilab Publications, Fermilab-FN341*, pages 1–10, 1981.

[39] L. Gatignon. Design and Tuning of Secondary Beamlines in the CERN North and East Areas. *CERN Document Server, CERN-ACC-NOTE-2020-0043*, pages 1–113, 2008.

[40] A. Wolski. Maxwell's equations for magnets. *CERN document server, CERN-2010-004*, pages 1–12, 2019.

[41] E. Wilson. *An Introduction to Particle Accelerators*. Oxford University Press, 2001.

[42] H. Wiedemann. *Particle Accelerator Physics*. Springer, 2015.

[43] A. Bogomyagkov et al. Effect of the sextupole finite length on dynamic aperture in the collider final focus. *arXiv:0909.4872*, pages 1–15, 2009.

[44] G. D'Alessandro et al. First "Skin Depth" estimations using GEANT4 and FLUKA based simulations for CERN secondary beamlines. *Nuclear Instrumentation and Methods B*, Vol. 512, pages 76–82, 2021.

[45] S. Prestemon et al. Structural design and analysis of a compact sweeper magnet for nuclear physics. *IEEE Transactions on Applied Superconductivity*, Vol. 11, 1721–1724, pages 2001.

[46] A. Aloev et al. CLIC Muon Sweeper Design. *Proceedings, International Workshop on Future Linear Colliders (LCWS15)*, pages 1–7, 2016.

[47] Y. N. Kharzheev. Scintillation counters in modern high-energy physics experiments (Review). *Physics of Particles and Nuclei*, Vol. 46, pages 678–728, 2015.

[48] G.Charpak et al. The Use of Multiwire Proportional Counters to Select and Localize Charged Particles. *Nuclear Instrumentation and Methods*, Vol. 62 (3), pages 262–268, 1968.

[49] C. Bovet et al. The CEDAR counters for particle identification in the SPS secondary beams : a description and an operation manual. *CERN Yellow Report, CERN-82-13*, pages 1–3, 1990.

[50] The NA62 Collaboration. NA62: Technical Design Document. *CERN Document Server, NA62-10-07*, pages 21–400, 2010.

[51] F. Frenet. Sur les courbes à double courbure. *Journal de Mathématiques Pures et Appliquées*, Vol. 17, pages 437–447, 1852.

[52] J.A. Serret. Sur quelques formules relatives à la théorie des courbes à double courbure. *Journal de Mathématiques Pures et Appliquées*, Vol. 16, pages 193–207, 1851.

[53] R.J. Webster and B.A. Jones. Design and Kinematic Modeling of Constant Curvature Continuum Robots: A Review. *The International Journal of Robotics Research*, pages 15–16, 2020.

[54] Y. Giboudot and A. Wolski. Use of transfer maps for modelling beam dynamics in a nonscaling fixed-field alternating-gradient accelerator. *Physical Review Special Topics - Accelerators and Beams*, Vol. 15, pages 6–7, 2012.

[55] M. Martini. An Introduction to Transverse Beam Dynamics in Accelerators. *CERN Document Server, CERN-PS-96-011-PA*, pages 1–13, 1996.

[56] E. Bravin. Transverse emittance. *Proceedings, 2018 CERN–Accelerator–School*, pages 2–3, 2018.

[57] E. Mobs. The CERN accelerator complex - 2019. Complexe des accélérateurs du CERN - 2019. 2019. General Photo.

[58] P. Collier. Status and Plans for the CERN Accelerator Complex. *Proceedings, XXIX International Symposium on Lepton Photon Interactions at High Energies (LP2019)*, pages 1–10, 2019.

[59] E. Montbarbon et al. The CERN East Area Renovation. *Nuclear Instruments and Methods in Physics Research Section B*, Vol. 461, pages 98–101, 2019.

[60] N. Abgrall et al. NA61/SHINE facility at the CERN SPS: beams and detector system. *Journal of Instrumentation*, Vol. 9 (2-3), pages 1–3, 2014.

[61] P. Abbon et al. The COMPASS experiment at CERN. *Nuclear Instruments and Methods in Physics Research Section A*, Vol. 577, pages 1–6, 2007.

[62] G. Brumfield. Cloud formation may be linked to cosmic rays. *Nature, pages 1–7*, Vol. 504, pages 1–7, 2011.

[63] J. Bernhard, the NA64 collaboration, and the Physics Beyond Collider Conventional Beams working group. Status and Plans for the NA64 Experiment. *Journal of Physics: Conference Series*, Vol. 1468, pages 12023–12027, 2020.

[64] The North Area at CERN. `https://gis.cern.ch`.

[65] C. Graham and D. Protopopescu. NA62 cavern and sub-detectors. 2017. General Photo.

[66] G. Ruggiero. New Result on $K^+ \to \pi^+ \nu \nu$ from the NA62 Experiment. *Journal of Physics: Conference Series*, Vol. 1526, pages 3–5, 2019.

[67] M. van Dijk G. D'Alessandro et al. The K12 beamline for the KLEVER experiment. *Proceedings, International Particle Accelerator Conference (IPAC2019)*, pages 3726–3729, 2019.

[68] B. Doebrich for the NA62 Collaboration. Searches for very weakly-coupled particles beyond the Standard Model with NA62. *arXiv:1711.08967*, pages 3–4, 2017.

[69] M. Pepe for the NA62 Collaboration. Search for exotics at NA62. *Journal of Physics: Conference Series*, Vol. 1137, pages 4–5, 2019.

[70] M. Rosenthal et al. Muon Background Studies for Beam Dump Operation of the K12 Beam Line at CERN. *Proceedings, International Computational Accelerator Physics (ICAP2018)*, pages 93–98, 2018.

[71] C. Lazzeroni. NA62/KLEVER prospects for future high-intensity K^+ and K_0 running, including beam dump. *Physics Beyond Colliders Annual Workshop*, 2021.

[72] G. Lanfranchi. SHADOWS. *Physics Beyond Colliders Annual Workshop*, 2021.

[73] G. Burton. BEATCH - a FORTRAN Programme for the Particle Optics of Beam Transfer Channels. *CERN Document Server, CERN-ISR-BT-TH-69-27*, pages 2–10, 1969.

[74] K. L. Brown, D. C. Carey, F. C. Iselin, and F. Rothacker. TRANSPORT : A Computer Program for Designing Charged-Particle Beam Transport Systems. *CERN Document Server, CERN-73-16*, pages 1–125, 1973.

[75] D. C. Carey. TURTLE with MAD Input - A Computer Program for Simulating Charged Particle Beam Transport Systems. *Fermilab Publications, FermilabPub-99/232*, 1999.

[76] C. Iselin. HALO - A Computer Program to Calculate Muon Halo. *CERN Document Server, CERN-74-17*, pages 2–10, 1974.

[77] A. Gerbershagen et al. CERN Secondary Beamlines Software Migration Project. *Proceedings, International Conference on. Accelerator and Large Experimental Physics Control Systems (ICALEPCS2019)*, pages 312–317, 2019.

[78] H. Grothe et al. The MAD-X Program (Methodical Accelerator Design) Version 5.02.08, User's Reference Manual. *CERN Document Server*, pages 2–240, 2016.

[79] E. Forest et al. Introduction to the polymorphic tracking code : Fibre bundles, polymorphic Taylor types and "Exact tracking". *CERN Document Server, CERN-SL-2002-044-AP*, pages 1–149, 2002.

[80] G. Battistoni et al. Overview of the FLUKA code. *Annals of Nuclear Energy*, Vol. 82, pages 10–18, 2015.

[81] T.T. Boehlen et al. The FLUKA Code: Developments and Challenges for High Energy and Medical Applications. *Nuclear Data Sheets*, Vol. 120, pages 211–214, 2014.

[82] V. Vlaouchidis. Flair: A powerful but user friendly graphical interface for fluka. *Proceedings, International Conference on Mathematics: Computational Methods and Reactor Physics*, pages 1–4, 2009.

[83] G. Battistoni et al. The FLUKA code: Description and benchmarking. *Proceedings, American Institute of Physics (AIP)*, pages 31–49, 2007.

[84] S.Agostinelli et al. Geant4-a simulation toolkit. *Nuclear Instruments and Methods in Physics Research Section A*, Vol. 506 (3), pages 250–303, 2003.

[85] Radovan Chytracek et al. Geometry Description Markup Language for Physics Simulation and Analysis Applications. *IEEE Transactions on Nuclear Science*, Vol. 53 (5), pages 2892–2896, 2006.

[86] L. Nevay et al. BDSIM: An accelerator tracking code with particle–matter interactions. *Computer Physics Communications*, Vol. 252, pages 1–16, 2020.

[87] L. Lonnblad. CLHEP: A project for designing a C++ class library for high-energy physics. *Computer Physics Communications*, Vol. 84, pages 307–316, 1994.

[88] R. Brun and F. Rademakers. ROOT - An Object Oriented Data Analysis Framework. *Nuclear Instruments and Methods in Physics Research Section A*, Vol. 389, pages 81–86, 1997.

[89] S. Boogert, G. D'Alessandro, et al. PYG4OMETRY : A tool to create geometries for GEANT4, BDSIM, G4BEAMLINE AND FLUKA for particle loss and energy deposit studies. *Proceedings, International Particle Accelerator Conference (IPAC 2019)*, pages 3244–3247, 2019.

[90] S. Boogert et al. PYG4OMETRY: a Python library for the creation of Monte Carlo radiation transport physical geometries. *arXiv:2010.01109*, pages 1–40, 2020.

[91] P. M. de Freitas. Mokka, main guidelines and future. *Proceedings, International Conference on Linear Collider*, pages 441–444, 2006.

[92] V. Uzhinsky on behalf of the Geant4 Hadronics Working Group. Development of the fritiof model in geant4. *Proceedings, Joint International Conference on Supercomputing in Nuclear Applications and Monte Carlo*, pages 1–4, 2010.

[93] D.H. Wright and M.H. Kelsey for the GEANT4 Hadronics Working Group. The Geant4 Bertini Cascade. *Nuclear Instruments and Methods in Physics Research Section A*, Vol. 804, pages 175–178, 2015.

[94] A. Lechner. Particle interactions with matter. *CAS - CERN Accelerator School: Beam Injection, Extraction and Transfer, Italy, 2017*, pages 47–66.

[95] A. Fasso' et al. New developments in FLUKA modelling hadronic and EM interactions. *Proceedings, The third workshop on simulating accelerator radiation environments*, pages 1–6, 1997.

[96] A. Ferrari and P. Sala. Nuclear reactions in monte carlo code. *Radiation Protection Dosimetry*, Vol. 99 (1), pages 29–38, 2002.

[97] S. Roesler et al. The monte carlo event generator dpmjet-iii. *Proceedings, International Conference on Advanced Monte Carlo for Radiation Physics*, pages 1–6, 2000.

[98] H. Sorge et al. Poincaré invariant hamiltonian dynamics: Modelling multi-hadronic interactions in a phase space approach. *Annals of Physics*, Vol. 192 (2), pages 266–306, 1989.

[99] A. Fasso' et al. The physics models of FLUKA: status and recent developments. *Proceedings, Computing in High Energy and Nuclear Physics (CHEP03)*, pages 1–9, 2003.

[100] A.W. Chao and M. Tigner. Handbook of Accelerator Physics and Engineering. *World Scientific Publishing*, pages 244–249, 2009.

[101] D. Banerjee, J. Bernhard, M. Brugger, N. Charitonidis, N. Doble, L. Gatignon, and A. Gerbershagen. The North Experimental Area at the Cern Super Proton Synchrotron. *CERN Document Server, CERN-ACC-NOTE-2021-0015*, 2021.

[102] B. Balhan et al. Improvements to the SPS Slow Extraction for High Intensity Operation. *CERN Document Server, CERN-ACC-NOTE-2019-0010*, pages 1–87, 2019.

[103] P.A. Arrutia Sota, Y. Dutheil, M Fraser, and F. Velotti. TT20 Transport and Splitting of Beams Extracted Using Crystal Shadowing in LSS2 of the SPS. *CERN Document Server, CERN-ACC-NOTE-2020-0040*, pages 1–17, 2020.

[104] pymadx. `http://www.pp.rhul.ac.uk/bdsim/pymadx/`.

[105] pybdsim. `http://www.pp.rhul.ac.uk/bdsim/pybdsim/`.

[106] The CATIA software. `http://catiadoc.free.fr/online/CATIAfr_C2/basugCATIAfrs.htm`.

[107] J. A. Dit Sandretto. Runge–Kutta Theory and Constraint Programming. *Reliable Computing Journal, hal-01762191*, pages 1–22, 2017.

[108] MCB magnet picture. `https://norma-db.web.cern.ch/magnet/idcard/5698/`.

[109] R. Appleby et al. Considerations for a RF separated K^+ beam for NA62. *CERN Document Server, CERN-PBC-Notes-2021-001*, pages 1–38, 2021.

[110] G. D'Alessandro et al. Studies for the K12 High-Intensity Kaon Beam at CERN. *Proceeding, International Particle Accelerator Conference (IPAC 21)*, pages 3049–3052, 2021.

[111] L. Bician. New measurement of the $K^+ \rightarrow \pi^+\mu^+\mu^-$ decay at NA62. *Proceedings, International Conference of High Energy Physics (ICHEP2020)*, pages 1–364, 2021.

[112] NA62MC. `https://github.com/nlurkin/NA62Analysis`.

[113] P. Llopis, C. Lindqvist, N. Høimyr, D. Ster, and P. Ganz. Integrating HPC into an agile and cloud-focused environment at CERN. *Proceedings, EPJ Web of Conferences*, Vol.214, pages 1–8, 2019.

[114] G. D'Alessandro et al. Muon Background Studies For the K12 High Intensity Kaon Bean at CERN. *To be published*, 2021.

[115] K. Massri. Studio di alcuni processi di background nell'esperimento NA62. Master's thesis, Università di Pisa, 2010.

[116] Samantha Lynn Pagan. Simulating Modifications to the P42 Beamline for the KLEVER Experiment. *CERN Document Server, CERN-STUDENTS-Note-2018-062*, pages 3–5, 2018.

[117] Radiation Protection Cluster. `https://coflucluster.cern.ch/coflu5/`.

[118] G.L. D'Alessandro et al. Target Bypass Beam Optics for Future High Intensity Fixed Target Experiments in the CERN North Area. *Proceedings, International Particle Accelerator Conference (IPAC 21)*, pages 3046–3048.

[119] S. Ghinescu, B. Döbrich, E. Minucci, and T. Spadaro. A biased MC for muon production for beam-dump experiments. *European Physics Journal C*, Vol. 81 (8), pages 766–774, 2021.

[120] F. Stummer. Studies and Optimization for future beam dump experiments in the K12 and P42 beams at CERN. Master's thesis, TU Wien, 2021.

[121] G. Lanfranchi G. D'Alessandro et al. SHADOWS (Search for Hidden And Dark Objects With the SPS). *arXiv:2110.08025*, pages 1–21, 2021.

[122] The Alice collaboration. Performance of the ALICE experiment at the CERN LHC. *International Journal of Modern Physics A*, Vol. 24, pages 1430–1444, 2014.

[123] G. D'Alessandro et al. Implementation of CERN Secondary Beam Lines T9 and T10 in BDSIM. *Proceedings, International Particle Accelerator Conference (IPAC 2019)*, pages 3746–3748, 2019.